REDUCTION OF CHROMIUM USING POLYANILINE BASED COMPOSITE MEMBRANE IN A PHOTOCATALYTIC MEMBRANE REACTOR

Thesis

Submitted in partial fulfilment of the requirements for the degree of

DOCTOR OF PHILOSOPHY

By

THARA RATHNA I V

(Register No: 177106CH008)

DEPARTMENT OF CHEMICAL ENGINEERING
NATIONAL INSTITUTE OF TECHNOLOGY KARNATAKA
SURATHKAL, MANGALORE -575025

JUNE 2023

D E C L A R A T I O N

I hereby declare that the Research Thesis entitled **"REDUCTION OF CHROMIUM USING POLYANILINE BASED COMPOSITE MEMBRANE IN A PHOTOCATALYTIC MEMBRANE REACTOR"** is being submitted to the National Institute of Technology Karnataka, Surathkal in partial fulfilment of the requirements for the award of the Degree of **Doctor of Philosophy** in the Department of Chemical Engineering *is a bonafide report of the research work carried out by me*. The material contained in this Research Thesis has not been submitted to any University or Institution for the award of any degree.

Place: Surathkal

Date: 20/06/2023

Thara Rathna I V

Register Number: 177106CH008

Department of Chemical Engineering

National Institute of Technology,
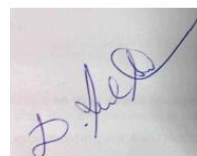
Surathkal, Karnataka

C E R T I F I C A T E

This is to certify that the Research Thesis entitled **"REDUCTION OF CHROMIUM USING POLYANILINE BASED COMPOSITE MEMBRANE IN A PHOTOCATALYTIC MEMBRANE REACTOR"** submitted by **THARA RATHNA I.V** (Register Number: **177106CH008**) as the record of the research work carried out by her, is accepted as the Research Thesis submission in partial fulfilment of the requirements for the award of the degree of **Doctor of Philosophy**.

Research Guide

Dr. P.E JagadeeshBabu

Associate Professor

Department of Chemical

Engineering

NITK, Surathkal

Research Guide

Dr. Ruben Sudhakar D

Assistant Professor

Department of Energy and

 Environment

NITT, Thiruchirapalli

Chairman -DRPC

Dr. P.E JagadeeshBabu

Head of the Department

Department of Chemical

Engineering

NITK, Surathkal

ACKNOLOWDEGMENT

ABSTRACT

The presence of heavy metals in the aquatic environment has become a severe threat to the ecosystem. This work focuses on the remediation of heavy metal Chromium present in the aqueous solution using a visible-light-driven photocatalytic membrane reactor via simultaneous photoreduction and separation. The hydrothermal method was used to synthesize TiO_2-based photocatalysts such as TiO_2-WO_3 and TiO_2-SnO_2. The photocatalytic membranes were prepared either by blending the photocatalyst nanoparticle before casting the composite membranes or by coating the photocatalytic nanoparticles on the membrane by physical method to obtain hierarchical membranes. Polyaniline was selected as the membrane material due to its interesting properties such as permselectivity, better electrical tunability, higher conductivity, economic viability, environmental stability, excellent tunable properties, and redox behaviour. Polyaniline (PANI) is also a very good adsorbent of Cr(VI) in acidic pH, and we could observe that the adsorption of Cr(VI) on the PANI membrane follows Freundlich and Jovanovic's multilayer adsorption isotherm, which indicates that the adsorption occurs by both physisorption and chemisorption. PANI/TiO_2 nanocomposite offered better adsorption and reduction of Cr(VI) to Cr(III) in acidic pH under visible light. The addition of nanoparticles in the membrane can impart synergistic effects such as improved hydrophilicity and permeability. The maximum performance of 98.50 % was observed in the nanofiltration membrane separation process operated for 60 min using 5 wt% TiO_2-WO_3 nanoparticle loading in the PANI membrane. The hierarchical membrane allows the immobilization of nanoparticles to facilitate catalyst recovery. TiO_2-based nanosheets, nanotubes, and nano-thorns have shown higher surface adhering capacity to allow a stable film formation. In this work, we could successfully synthesize TiO_2-WO_3 nanocubes-coated hierarchical PANI membranes. The membrane 'M1' (50 mg loaded) showed better photocatalytic efficiency (removal/separation) of around 79.30 % in a custom-made photocatalytic membrane reactor. The hierarchical assembly also offered self-cleaning ability, and the coating on the membrane prevented the PANI emeraldine salt membrane from over-oxidation.

Keywords: TiO_2, WO_3, SnO_2, Polyaniline, Hierarchical membrane, Chromium, Photocatalysis, Composite membrane, Visible light

CONTENTS

LIST OF FIGURES

xiii

LIST OF TABLES

NOMENCLATURE

PANI – Polyaniline

Cr(VI) – Hexavalent Chromium

Cr(III) – Trivalent Chromium

Jw – Flux of pure water (L/m^2h)

A - Area of cross-section of the membrane (m^2)

Wt% - Weight percentage

SEM – Scanning Electron Microscopy

TEM - Transmission Electron Microscopy

XRD – X-ray Diffraction Analysis

ATR-FTIR – Attenuated Total Reflectance Fourier Transform Infrared Spectroscopy

XPS – X-ray Photoelectron Spectroscopy

KSPCB – Karnataka State Pollution Control Board

USEPA- United States Environmental Protection Agency

MCL – Maximum Allowable Limit

UF - Ultrafiltration

NF - Nanofiltration

RO – Reverse Osmosis

WO_3 – Tungsten oxide

SnO_2 - Tin oxide

NIPS – Non-solvent Induced Phase Separation

MWCO – Molecular Weight Cut Off

CPs – Conducting Polymers

PT – Polythiophene

PS - Polystyrene

PSf - Polysulfone

PPy – Polypyrrole

S/cm – Siemen per centimetre

NMP- N-methyl-2- pyrrolidone

BSA – Bovine serum albumin

CHAPTER 1

INTRODUCTION

Water pollution has become an issue of increasing concern in this current scenario. The release of inadequately treated wastewater into natural water bodies can lead to the deterioration of aquatic ecosystems. Industrial effluent and sewage water mainly contain toxic products such as heavy metals, dyes, and other inorganic and organic chemicals. Among the heavy metals, Chromium enters the environment from anthropogenic sources such as electroplating factories, textile manufacturing facilities, and leather tanneries.

The tannery is one of the major industries in India that involves several chemicals such as Calcium chloride, Chromium sulfate, etc in their treatment process. The untreated effluent that are generated in such industries is generally discharged either into the land or water bodies, which degrades the soil and affects aquatic organisms and plants. The major pollutant in the tannery wastewater is Chromium and it can easily penetrate into the other water sources like groundwater and surface water. Chromium exists in its two oxidation states such as trivalent and hexavalent Chromium. Trivalent Chromium is essential for human health, but hexavalent Chromium is highly toxic and carcinogenic in nature. In humans, trivalent Chromium is stored in the skin, muscle, and fat, and Cr (III) plays a major role in normal insulin function. In India, particularly in north Karnataka, the increase of Chromium concentration in the groundwater is a major problem. Bangalore district has 29 mg/L of Chromium in their groundwater, which is more than the allowable limit. The major sources of Chromium in groundwater are electroplating industries of that area.

Chromium is a shiny metal, which can react with air and form a thin layer of Cr(III) oxide. Chromium occurs in $2^+,3^+,6^+$ oxidation forms. Chromium is available in different forms, like Chromium (II) oxide, Chromium (III) oxide, Chromium (III) sulfate, Chromium (III) chloride, Chromium (IV) oxide, Chromium (VI) oxide, chromyl chloride, and chrome alum. The two main types of Chromium ions are Chromium (III) and Chromium (VI).

In plants, only trivalent Chromium is absorbed, which is essential for plant growth and crop yield. Hexavalent Chromium forms chromate (CrO_4^{2-}) which is more soluble in water than trivalent Chromium. High concentrations of Chromium, due to the disposal of metal

products in surface water, can damage aquatic life like fish that swim near the point of disposal. High doses of Chromium can cause digestive tract cancer in humans, and there is an increased risk of lung cancer in workers who are exposed to high levels of Chromium. Chromate poisoning causes severe skin disorders such as allergic dermatitis, and liver and kidney damage. The removal of chromate from the polluted environment is essential to protect the environment.

In the past centuries, a significant breakthrough was achieved in establishing new processes for removing metal from various liquors and effluents. The conventional heavy metal removal methods include chemical precipitation, ion exchange, electrochemical treatment, membrane technology, adsorption on activated carbon, biosorption, and phytoremediation. But, the major setbacks of these methods include long process times, high sedimentation, high cost, and partial removal of ions. Bioremediations like phytoremediation take a long duration in plant generation. Several new and innovative solutions for efficient heavy metal removal have been investigated, and it is strongly believed that they will help in solving the problems of water pollution and soil pollution.

1.1 ENVIRONMENTAL CONCERN ABOUT HEAVY METALS

Heavy metal contamination in the environment is lithogenic and anthropogenic in origin. The various anthropogenic activities that introduce heavy metals into the environment are mining, smelting of ores, municipal waste, burning of fossil fuels, battery manufacturing, industrial effluents, and agricultural activities. Heavy metals possess a threat to life due to their toxicity, faster mobility in water, non-biodegradability, and accumulation in soft tissues which cause both short- and long-term damage. Heavy metals are elements with atomic weights between 63.5 - 200.6 and a specific gravity greater than 5 (Zare et al. 2018), (Kang et al. 2004). The list of heavy metals which cause major health issues to humans as well as other flora and fauna include Copper (Cu), Chromium (Cr), Zinc (Zn), Nickel (Ni), Cadmium (Cd), Mercury (Hg) and Lead (Pb) (Zare et al. 2018). These pollutants affect aquatic life and cause our divine rivers to dry up and lead to the scarcity of fresh water on the earth. Among all the heavy metals listed above, Chromium is often found in the primary water resources, and Chromium also causes diarrhoea, nephritis, necrosis, vomiting, headaches, cancer, and even death. The primary anthropogenic sources which generate excess Cr(VI) concentration in the environment are mining, smelting of ores,

2

electroplating, tannery effluents, wood preservation, paints and pigments etc (Dozzi et al. 2016a).

Chromium majorly exists in its more toxic hexavalent form, and less toxic trivalent oxidation states. The former one is 500 times more toxic, carcinogenic and teratogenic than the immobile trivalent Chromium. In India, many cities are affected by Cr(VI) poisoning, and have already been in the limelight in the recent past. The cities which face Chromium problems include Ranipet (Tamil Nadu), Peenya (Karnataka), Vadodara (Gujarat), Talchar (Odissa), and Kanpur (Uttar Pradesh). Karnataka has the highest number of polluted river stretches in South India. According to Karnataka State Pollution Control Board (KSPCB), 3,777 million litres of sewage effluent are generated and diverted into the state rivers every day. Of this, only 1,304 million litres are treated and the remaining 2,473 million litres are left in rivers without any treatment. Annually, 9,03,645 million litres of sewage water and industrial effluent join the lifelines across the state and only 4.75 lakh million litres are treated. According to India Today news, daily 50% of industrial heavy metal waste are directly dumped into Vrushabhavathi river from Peenya industrial area (Shankar 2009a). The Hindu daily reported in June-2016 that the borewells tested in India's largest industrial area, Peenya, show concentrations of Chromium up to 35 mg/L, whereas the allowable national limit for Chromium is 0.05 mg/L. A survey conducted by Karnataka State Pollution Control Board (KSPCB) in 72 borewells reports that more than 25 % of the wells are heavily polluted (600 to 700 times concentration than national limit) with Chromium. The untreated effluents from electroplating units inside the Peenya area are said to be the major cause of pollution. These terrifying facts reflect the absence of rigid environmental protection norms in India. The United States Environmental Protection Agency (USEPA) has suggested a standard maximum allowable level (MCL) of Chromium (VI) of 0.1 mg/L (Khulbe and Matsuura 2018) and the Indian standard allows 0.5 mg/L of Cr(VI) in the drinking water. Chromium is one of the most widely used metals in the industry and it exists in its different oxidation states in the environment. The Cr(III) is vital for human and plant metabolic activities, but the excess amount is lethal to all living tissues. The abatement of Chromium (VI) ions from drinking water is essential to protect humans from Chromium (VI) pollution.

The conventional techniques used for heavy metal reduction include adsorption, precipitation, ion exchange, membrane filtration, coagulation, flocculation, floatation,

electrodialysis (Fu and Wang 2011) and advanced oxidation technique such as photocatalysis.

1.2 HEAVY METAL REMOVAL TECHNIQUES

The commonly followed practices for removing heavy metals from effluent water are chemical precipitation, ultra-filtration, ion exchange, reverse osmosis, electrowinning, carbon adsorption, and phytoremediation.

Joshi et al., in 2017 have mentioned in their work the conventional and current methods used for heavy metal removal. In the chemical precipitation method, metal ions precipitate with the help of alum, lime, and coagulants like organic polymers. The main disadvantage of chemical precipitation is the formation of an enormous amount of sludge during the process. In the ion exchange process, the metal ions from dilute solutions can be removed using exchange resins. The main disadvantages of ion exchange are its high cost and partial removal of ions. Reverse osmosis is another method that is extensively used for the removal of metal ions from water. The separation is carried out by using a semipermeable membrane at a pressure greater than the osmotic pressure, which is caused by the dissolved solids, and this method is an expensive one. Electrowinning is another method used for metal ion removal. In this method, metal ion removal occurs by the reduction process in an electrode. The reaction chamber contains a suitable electrolyte and electrodes. The main drawback is that there must be a higher concentration of metal cations in the effluent water, and this restricts its efficiency. The carbon adsorption method removes metal contaminants from single-phase liquid streams using granular activated carbon. The high surface area to volume ratio of activated carbon helps in metal ion adsorption. The main disadvantages of this method are its cost and the requirement for pre-treatment. Process efficiency can also be affected by fouling (Joshi 2017).

Biosorption and phytoremediation are the two main remediation techniques used for heavy metal removal. In phytoremediation, selected plant species are utilized to clean up the wastewater. Species like gymnosperms, aquatic macrophytes, bryophytes, and tree crops have shown significant removal of metal ions from wastewater. The major disadvantages of this process include its long duration and the regeneration of plants. The biosorption technique utilizes the metal sorption potential of certain natural adsorbents, which include algae, fungi, bacteria, and waste materials. It was reported that the white inner skin of orange peel can be used for the removal of Chromium in acidic conditions (Ingole and Dharpal 2012).

In the recent past, membrane separation has gained attention as an emerging technique for wastewater treatment due to its convenient operation. The membrane filtration method includes microfiltration (MF), ultrafiltration (UF), nanofiltration (NF), and reverse osmosis (RO). Photocatalysis is an innovative technique used for effluent water treatment under UV-Visible light (Barakat 2011). Alexa and Mamba et al. (2016) in their work, discussed the scope of combining physical separation via membrane filtration and pollutant degradation achieved by photocatalysis in a single and smart unit called a photocatalytic membrane reactor (Kuvarega and Mamba 2016).

1.3 PHOTOCATALYSIS

In the recent past, photocatalysis has gained more attention among researchers because of its capacity to handle a wide variety of pollutants and sustainable energy production (Putri et al. 2015). Photocatalysis utilizes the energy of photons to propel chemical reactions. In 1972, Fujishima and Honda reported that the TiO_2 semiconductor can split water into hydrogen and oxygen in a photo-electrochemical cell, which led to the evolution of newer technology in the scientific world (Pelaez et al. 2012). Photocatalysis is a semiconductor mediated process that eliminates pollutants by converting optical energy into electrochemical energy required for photo-oxidation by the catalyst (Hai and Zhang 2019) TiO_2 is a widely used photocatalyst in water purification, but the wider bandgap and less photostability limit its performance in the visible light region. To improve the photocatalytic properties of TiO_2, many techniques have been found to produce TiO_2 composite nanoparticles of visible range capacity, including doping with metal or metal oxides, noble metal deposition, anion doping, and exfoliation etc. The photocatalytic behaviour of a semiconductor is due to their distinct electronic structure, having a filled valence band and an empty conduction band. Catalysts like TiO_2, ZnO, SnO_2, Fe_3O_4, $BiVO_4$, CdS have been used for the reduction of $Cr(VI)$ under UV light, but the efficiency was poor and not suitable under visible light (Pawar and Lee 2015). The coupled semiconductor catalysts have gained their way into the research of photoreduction of $Cr(VI)$ under UV/Visible light. WO_3 is considered a better photocatalytic material because of its higher stability, photocorrosion resistance, and lower bandgap (2.8 eV), which utilizes the visible light spectrum. Recent research has also shown that mixed metal oxide semiconductors can be used to decompose toxic organic compounds in photovoltaics, used to prevent fogging on the glass, split water into hydrogen, and convert CO_2 into methanol.

For photoreduction of Cr(VI), a semiconductor should possess more positive conduction band minima than the actual reduction potential of Cr(VI) (i.e. $E_0 = 1.36$ V) (Cheng et al. 2015).

In photocatalysis, the photo-induced reactions take place on the surface of a TiO_2 catalyst. The initial photo-excitation occurs on the catalytic substrate, and then electron transfer occurs from valence band to conduction band, which is called as sensitized photoreaction. If the initial excitation occurs in the adsorbate molecules and then the reaction takes place, then it is called a catalysed photoreaction (Gautam et al. 2014). Recombination of holes and electrons is the major drawback in most semiconductor photocatalysts, which hinders their photocatalytic efficiency. The availability of active surface area is an important factor in photon absorption. The surface area of the catalysts can be modified by both chemical and physical methods. Coupling of semiconductors can offer drastic changes in the electronic properties of a newly formed complex. The charge recombination in a catalytic reaction can be reduced by lowering the energy bandgap of the catalyst. Titanium dioxide (TiO_2) is a versatile material which is majorly used in photocatalytic reactions. Aeroxide P25 (TiO_2) is the most famous commercial photocatalyst, which is a non-toxic, environmentally friendly, and inexpensive photocatalyst. P25 has been proven to have the most photocatalytic activity under visible light. The most promising solution to modify TiO_2 is to prepare TiO_2-composites by using π- conjugated polymers such as Polyaniline. Polyaniline is a non-toxic, thermally stable polymer with a high absorption coefficient in the visible light region (Novaković et al. 2016).

1.4 PHOTOREDUCTION OF CHROMIUM (VI)

Chromium (VI) under acidic pH (pH <6.5) is a relatively strong oxidant and its oxidative nature is the reason for its toxicity (Ansari 2006). The higher toxicity and mobility of Chromium (VI) in the environment causes significant damage to the food chain. Removal of Cr(VI) or converting it to less toxic form like Cr(III) is a demanding concern these days. The metal oxide catalysts like TiO_2, ZnO, WO_3 and CeO_2, have been employed for the photoreduction of Chromium (VI). The photo-reduction of Cr(VI) to Cr(III) majorly depends on the parameters such as pH of the pollutant, initial concentration of pollutant, catalyst loading, extent of exposure to light, and availability of active surface area of the catalyst. The photoreduction occurs in three steps, adsorption of Cr(VI) species on the surface of the catalyst, reduction of the Chromium and precipitation of the product. The

solution pH plays a significant role in the whole Cr(VI) photocatalytic reduction process, which will affect both the surface adsorption and the Cr(VI) reduction potential.

The amount of Cr(VI) absorbed by a semiconductor varies with solution pH. Optimum pH for Cr(VI) adsorption by TiO_2 lies in the range of pH 3-6. At pH 2.0, Cr(VI) exists as chromic acid (H_2CrO_4) and at acidic pH (pH 3-6), dichromate, and hydrogen chromate ($HCrO_4^-$) ions dominate in the solution whereas, at pH >6, Cr(VI) exists as chromate (CrO_4^{2-}) ions (Dognani et al. 2019). For the solution pH greater than 6.0, the negative charge on the TiO_2 surface increases and the negatively charged Cr(VI) radical repels due to lack of electrostatic affinity and thus reduces the extent of adsorption on the catalyst surface (Ku and Jung 2001). It was believed that the rate-determining step in the photocatalytic reduction of Cr(VI) was the surface reaction step after the Cr(VI) was adsorbed on the catalytic surface. Light intensity greater than 17.14 W/m^2 has a minimum effect on the reduction rate. In this study, the light intensity used was 20.54 W/m^2, and the light intensity is excessive in comparison with the amount of catalyst particles present in the solution to generate a more significant number of photoelectrons (Lee et al. 2015). The Cr(VI) reduction reaction equations (Sane et al. 2018; Liu et al. 2014; Yin et al. 2018) are given below.

$$HCrO_4^- + 7H^+ + 3e^- \rightarrow Cr^{3+} + 4H_2O \hspace{4cm} \rightarrow (1.0)$$

For acidic solutions:
$$Cr_2O_7^{2-} + 14H^+ + 6e^- \leftrightarrow 2Cr^{3+} + 7H_2O \hspace{3cm} \rightarrow (2.0)$$

For alkaline solutions:
$$Cr_2O_7^{2-} + 14\,H_2O + 3e^- \leftrightarrow 2\,Cr(OH)_3^+ + 5OH^- \hspace{2cm} \rightarrow (3.0)$$
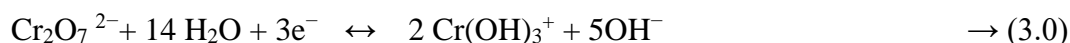
The reduced Cr(III) can be precipitated as Cr_2O_3 (acidic pH) and $Cr(OH)_3$ (at basic pH). Hexavalent Chromium is a predominant form of Chromium and is highly toxic and carcinogenic. The high water solubility of Cr(VI) makes it dissolve in the water bodies easily and becomes a life-threatening pollutant. The abatement of Cr(VI) can be possible in two ways, Cr(VI) can be removed, or it can be reduced to a less toxic form. In this study, we propose that coupled metal oxide semiconductor catalysts be synthesized, followed by their incorporation into the PANI-based membrane by blending or depositing the catalyst on the membrane. The prepared composite and hierarchical membranes will be used to

reduce the Chromium (VI) under visible light. Further, the composite membrane's Chromium (VI) reduction reaction is optimized.

1.5 MEMBRANE TECHNOLOGY

A membrane is an interphase between two adjacent phases that acts as a selective barrier between the two compartments. According to the material of construction, the membranes can be classified as polymeric, inorganic, or organic-inorganic composite membranes. The development of the first high-flux anisotropic RO membranes (via NIPS from cellulose acetate) by Loeb and Sourirajan in 1963 has become one of the most critical breakthroughs in membrane technology. The first polymeric membrane synthesized was cellulose acetate, and the first inorganic semipermeable membrane was synthesized using Rayon in 1867. Gradually, polymeric membranes became well accepted in many fields due to their reproducibility and low cost compared to ceramic membranes. In the early stages, cellulose acetate, collodion, cellophane, and Rayon were the most widely used monomers to prepare organic membranes. However, these hydrophilic polymers were unable to use in harsh environments (acidic and basic pH, temperature). Hydrophobic polymers such as polysulfone, polyvinylidene fluoride, polyether sulfone, and polyetherketone were also preferred. The properties like purity, mechanical, and high chemical resistance have made these hydrophobic polymers a unique material to use as membranes.

Pressure driven membranes can be classified as microfiltration membranes (MF), ultrafiltration membranes (UF), nanofiltration membranes (NF) and reverse osmosis membranes (RO) (shown in Figure 1.1). Microporous membranes with a pore size of about 0.1–5 µm can only be used for filtering particles with a size of 1–10 µm, which limits their applications in water purification. The nanoporous membranes exhibit high performance in water purification. They can filter most of the pollutants (1–10 nm), such as metallic ions, organic molecules, salts, and microbes from wastewater (Wang et al. 2018). The most common way of preparing an asymmetric membrane is the phase-inversion technique. An asymmetric membrane consists of a dense skin layer supported by a microporous matrix bottom layer. These membranes can be classified as integrally skinned and single/multi-layered composite asymmetric membranes. The filtration ability of any membrane is based on the molecular weight cut off (MWCO) of the membrane. MWCO is the molecular weight of the solute in the feed with 90% retention indicates the molecular weight cut off of the particular membrane. Assembly of nanomaterials on the top of polymeric membranes

is a novel technique in the degradation/filtration of pollutants under UV-visible light. These multifunctional hierarchical membranes will help in both filtration and degradation of pollutants and can provide a better technique to immobilize the nanocatalyst. The pore size of the membrane should be smaller than the size of loaded nanoparticles. TiO_2 has been proven to be a promising semiconductor catalyst in heterogenous photocatalysis and its outstanding properties such as stability, low cost, non-toxicity and photocatalytic activity make TiO_2 an unavoidable material even in water purification. Several methods have recently been developed and optimised for the fabrication of TiO_2-polymeric membranes. Embedding TiO_2 nanoparticles into the polymeric membrane matrix and electrospinning TiO_2 fibres or flat membranes by recasting are some examples. TiO_2 nanosheets and nanofibers have shown better prospects in the fabrication of TiO_2 hierarchical membranes. There are no reports on polyaniline hierarchical membranes for the photocatalytic reduction of heavy metals.
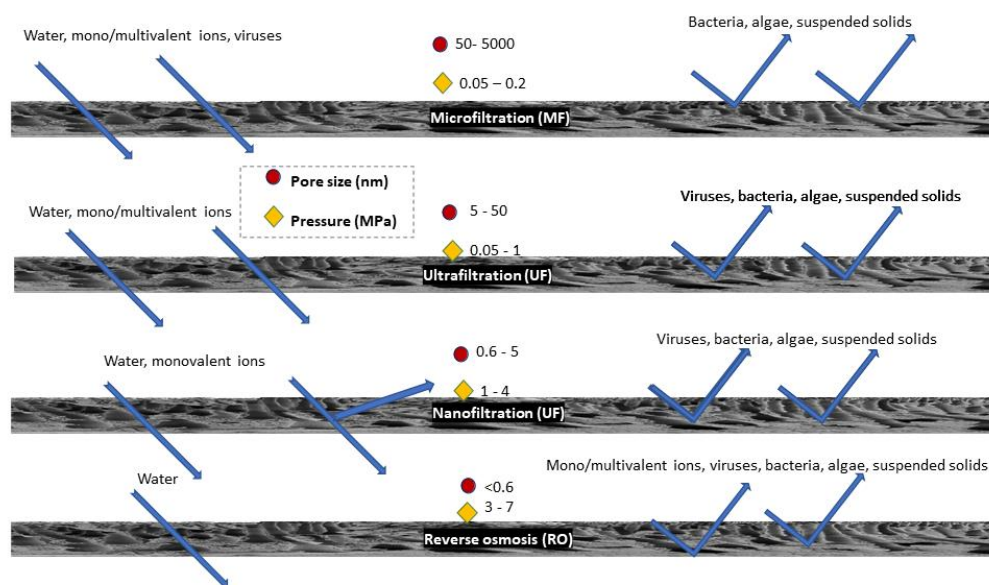
Figure 1.1 Different modes of pressure driven membrane filtration (Sirshendu De 2015)

1.6 POLYANILINE AS MEMBRANE MATERIAL

The introduction of conducting polymers (CPs) in environmental remediation has acquired significant recognition over the past few years (Sahu et al. 2019). Conducting polymers have emerged as potential candidates in the fields of smart materials, sensors, supercapacitors, and photocatalysis due to their excellent properties. Polyaniline (PANI), polythiophene (PT) and polypyrrole (PPy) are the most commonly used conductive

polymers for various applications. Its excellent bio-compatibility, non-toxicity, tuneable conductivity, and tuneable hydrophilicity make these conducting polymers an iconic material in membrane technology.

Like metals, the electrical conduction in organic materials is carried out by delocalized π-electron. In conducting polymers, there is a significant overlap of delocalized pi-electron along the polymer chain. The electrical conductivity in intrinsically conducting polymers results from the existence of charge carriers (through doping) and the ability of charge carriers to move along the π-bonded highway. In the neutral (undoped) state, polymers behave as semiconductors ($\sigma = 10^{-7}$ to 10^{-11} S/cm), and the conductivity can be achieved by doping, i.e., injection of electrons and holes to the superorbital of these materials. ($\sigma = 1$ to 10^5 S/cm) for CPs. The conjugated polymers can be of n-type (reduced) or p-type (oxidized) to a relatively high density of charge carriers. Polyaniline is a conducting polymer and occurs in three forms, which have different colours, stabilities, and conductivities. Leucoemeraldine is a colourless substance characterized by an absorption band at 343 nm (in *N*-methyl pyrrolidone). Since this polymer contains only benzene and amino groups, leucoemeraldine slowly oxidizes in the air and is not electrically conducting. Leucoemeraldine may be oxidized in an acidic medium to a conducting emeraldine salt form (*p* doping). Pernigraniline is composed of alternate aminobenzene and quinonediimine fragments. The quinonediimine group is unstable in the presence of nucleophiles, especially in water. Moreover, pernigraniline will readily decompose in the air.

The mass transfer properties of the Polyaniline membranes, like permeability for gases, solvents, water and acids, are discussed in the next chapter. It is reported that in the undoped state, the membrane is hardly permeable to inorganic ions (Wen and Kocherginsky 1999). PANI can be tuned with various protic acids (HCl, HNO_3, H_2SO_4) to make it conductive, and it can be easily used to form more permeable freestanding films (Rohani et al. 2017a; Zhang et al. 2010). Undoped PANI films are utilized in gas separation and sensing applications due to their void space in the polymer matrix. PANI membranes in their doped state are more permeable to water and solvents (Sairam et al. 2006). PANI can separate mixtures of liquids (pervaporation) due to the hydrophobic and hydrophilic characteristics of the undoped and doped films (Tan et al. 2003). Doping helps in the formation of the ES form of PANI, and the amine and imine functional groups can be created by chelating the metal ions, which helps in the removal of Chromium (Bozkir et al. 2012; Macdiarmid et al.

1987),(Ding et al. 2018; Qiu et al. 2015). Few researchers have used the particulate form of PANI for the removal of heavy metals, with limitations like regeneration and recycling of PANI (Tan et al. 2003). The major drawbacks of the PANI membrane are its low solubility and poor mechanical strength due to the rigid-rod macro-molecular chains (Rohani et al. 2017a; Yue et al. 2017; Yusoff et al. 2019). These drawbacks can be overcome by fabricating composite membranes to improve mechanical strength as well as filtration performance.

1.7 PHOTOCATALYTIC MEMBRANE REACTOR (PCMR/PMR)

A photocatalytic membrane reactor is a process in which both membrane filtration and photocatalytic degradation occur simultaneously. The hierarchical membrane on which nanoparticles are coated can act as a photocatalytic material for the degradation of pollutants. The photocatalytic membrane reactor can be operated in four different configurations depending on the configuration of the membrane for the water treatment, which are

(a) slurry photocatalytic reactor followed by a membrane filtration unit,

(b) ceramic or polymeric membrane submerged in a slurry photocatalytic reactor,

(c) membrane is placed inside a photocatalyst-coated (TiO_2) photoreactor and

(d) **photocatalytic membranes** (pure TiO_2 or TiO_2 -mixed matrix membranes) (Alex T Kuvarega and Bhekie B Mamba 2018).

The PMRs with solubilized and suspended catalyst can be further classified as integrative and split types. In the integrative type, the photocatalytic reaction and membrane separation take place in a single unit, and in the latter case, the photocatalysis and the membrane separation take place in two separate apparatuses (Argurio et al. 2018).

In immobilised systems (photocatalytic membrane configuration), UV light and reactive oxygen species pose a threat to the polymeric membranes, while in suspended systems, this risk can be reduced in specific types of arrangements (separation of reaction from membrane zones). Additionally, the abrasive effect of the photocatalyst particles in the slurry-type PMRs can harm both polymeric and ceramic membranes. Therefore, it is advised to conduct extensive research on the stability of membranes before choosing one (Mozia et al. 2018). The viability of pressure driven (using MF, UF, or NF membranes) PMRs for industrial sectors seems to be limited despite all these technological developments and accuracy (Molinari et al. 2004).

Polymer membranes have gained popularity in wastewater treatment and water purification. The most widely used polymeric membranes for the catalyst blending were PVDF (polyvinylidene fluoride) membranes (Argurio et al. 2018). Blending of nanoparticles into the membrane reduces leaching (Kumari et al. 2020) and the chocking due to fouling. The membrane serves simultaneously as support for the photocatalyst and also as a selective barrier for the molecules that must be degraded.

 The conjugated polymer like PANI can be used for the preparation of membranes because of its tunable properties and reductive adsorption towards hexavalent Chromium. TiO_2 is the most extensively explored nanoparticle for photocatalytic membrane synthesis. The photocatalytic nanoparticles can either be deposited onto the membrane surface or dispersed in the polymer solution prior to membrane casting. Several other methods have been proposed and tried for the fabrication of polymeric and ceramic photocatalytic membranes. In this work, both composite and hierarchical membranes will be fabricated and utilized for heavy metal filtration/degradation in a polymeric membrane reactor.

CHAPTER 2

LITERATURE REVIEW

2.1 IMPACT OF HEAVY METAL ON THE ENVIRONMENT

The release of heavy metals into the environment is a growing concern, where the heavy metal even damages the ecosystem. The most commonly found heavy metals are Lead (Pb), Chromium (Cr), Arsenic (As), Zinc (Zn), Cadmium (Cd), Copper (Cu), Mercury (Hg), and Nickel (Ni). The Minamata disease, which originated in the Minamata city of Japan, is a living victim of heavy metal poisoning in the world. The methyl mercury compound present in the drainage from the Chisso Minamata factory polluted the river, and the organic mercury accumulated in the bodies of fish and the intake of fish has led to an outbreak of infectious disease in humans. The heavy metals and health effects caused by the metals are given in table 2.1.

Table 2.1 Heavy metals and health effects ((Gautam et al. 2014), (Barakat 2011))

Heavy metal	Toxicities	Maximum contaminant level (MCL)
Arsenic	Skin manifestations (Causes melanosis, keratosis), visceral cancers, vascular diseases	0.05
Cadmium	Kidney and bone damage, renal disorder, Bronchitis, emphysema, anaemia, Acute effects in children	0.01
Chromium	Necrosis, nephritis, and death in humans, headache, diarrhoea, nausea, vomiting, carcinogenic	0.05
Copper	Liver damage, Wilson disease, insomnia	0.25
Nickel	Dermatitis, nausea, chronic asthma, coughing, human carcinogens	0.2

Zinc	Depression, lethargy, increased thirst, abdominal pain,lack of muscular coordination.	0.8
Mercury	Kidney disease affects the circulatory system and nervous system. It disturbs the cholesterol.	0.00003
Lead	Toxic to human and aquatic fauna, tiredness, anaemia, hypertension, behavioural changes in children, brain damage	0.006

Industrial effluent containing heavy metals is the major contributor to water pollution. This work concentrates on the heavy metal Chromium (VI) because of its effects on the ecosystem. The wastewater from industries like tanneries, metal plating, pulp, petroleum refining, paint, and pigment contains the heavy metal Chromium in its hexavalent oxidation state. Chromium metal primarily occurs in the form of Cr(VI) and Cr(III). The former is 500 times more toxic and can easily penetrate than the latter (Nur-E-Alam et al. 2020). The maximum acceptable levels of Cr(III) and Cr(VI) in the environment are 5 mg/L and 0.05 mg/L. In India, the concentration of Cr(VI) in polluted water is in the order of 10 – 100 mg/L (Sane et al. 2018). The excess amount of Chromium in drinking water causes severe skin disorders such as dermatitis, cancer, liver and kidney damage. According to Shankar et al. (2009), about 30-35 litres of water is used to process one kilogram of leather, and about 680 million litres of effluent is created daily (Shankar 2009). Although technological advancement has improved human life, it has also produced significant pollution. There should be a green and cheaper technique to mitigate toxic chemicals like Cr(VI) and further development of techniques to convert or remove it from the environment.

Many remediation strategies have been put forward to deal with Cr(VI) pollution, including adsorption, ion exchange, chemical precipitation, membrane filtration, and reductive techniques like photocatalysis. Reductive remediation with several natural and synthetic compounds is capable of reducing Cr(VI).

2.2 HEAVY METAL REMOVAL METHODS

There are various remediation technologies that have been used for the removal of heavy metals from water/wastewater. These remediation technologies are summarized below.

2.2.1 Electrocoagulation

The electrocoagulation technique utilizes electrodes, where the oxidation and reduction take place. The processes of oxidation, reduction, coagulation, and adsorption govern the process of electrocoagulation. For heavy metal removal, this is a cost effective and easy handling technique. This technique has been used for the treatment of dyes, heavy metals, nitrates, fluorides, and phenolic compounds from wastewater. Golder et al. first investigated the removal of Cr(III) from water by electrocoagulation methods (Golder et al. 2011). Removal of Cr(III) from aqueous solution by electrocoagulation using iron electrodes is a feasible process. This technique can be used for the reduction of pollutants down to the ppb level, but the high cost of resin makes the process costly for industrial scale applications. This technique produces secondary pollutants at the anode and the cathode edges during the Cr(VI) to Cr(III) conversion (Osipenko and Pogorelyi 1977).

2.2.2 Ion-exchange

The ion-exchange resins provide many advantages and are the most widely used techniques for the treatment of wastewater effluents. Lee and Nicol have used the Diphonix resin to remove ferric iron from a cobalt sulfate solution with various pH ranging from 0.5- 2.5 (Lee and Nicol 2007). A lower pH and a higher dose of resin give a higher removal of cations from the solution. In their work, elution of iron was observed with an increase of Ti(III) in the sulfuric acid eluent. It was found that the iron elution enhances with Ti(III), due to the combined effects of a reduction of Fe (III) and competitive adsorption of Ti(III) and Ti(IV) ions. The major disadvantage with the particular Diphonix resin lies in eluting iron from the resin and resins are comparatively expensive. Kononova et al. reported the recovery of simultaneous Cr(VI) and Mn (II) ions from aqueous solutions on an ion exchanger with long-chained cross linking agents   (Kononova et al. 2019). Nowadays, inexpensive sorbents are used to modify the resins and improve the sorption capacity.

2.2.3 Adsorption

Adsorption is one of the remediation techniques used for the removal of metal ions. Studies have been done for surface modifications of natural clays with reagents containing metal binding groups. The Montmorillonite clays were modified by embedding ammonium organic derivatives with different chelating agents. The modification of clays with organic and inorganic components could enhance their sorption capacity. Heavy metals have been

removed through the grafting of amino or mercapto groups onto the surface of the clay by a reaction with the silanol groups. Various low-cost adsorbents, including agricultural waste, industrial by-products like fly ash, waste iron, green sand, iron slags and hydrous titanium oxide, can be used to remove metal ions from wastewater. Other materials like hazelnut shell, rice husk, jackfruit and maize cob or husk can be used as an adsorbent for heavy metal uptake after chemical modification or converting them into activated carbon. Hydrogels are another attractive material used for adsorption. The presence of different functional groups in the structure facilitates metal ion adsorption. Biopolymers derived from chitin, chitosan and starch are chemically modified to obtain crosslinked forms and immobilized on insoluble support to facilitate metal ion adsorption.

Ali et al. reported the adsorptive removal of Cr(VI) from wastewater by acrylonitrile grafted banana peels (GBPs). The maximum adsorption of Cr(VI) was observed at pH 3.0, adsorbent dose 4 g/L, concentration 400 mg/L and at a contact period of 120 min. The modification of banana peels by chemical treatment has induced the functional groups of cellulose so that it can attach to metal ions. The activated banana peels can be used as an alternative to expensive activated carbon (Ali et al. 2016a). The different Cr(VI) removal techniques and their efficiencies are given in table 2.2.

Table 2.2 Removal efficiency of Cr(VI) using different methods

Initial Concentration	Removal method	pH	Efficiency	Reference
10 mg/L	Membrane separation	pH -3.0 - 5.0	100 %	(Jyothi et al. 2014)
20 mg/L	Photocatalysis	pH < 7	99.99 %	(Naimi-Joubani et al. 2015)
0.2- 8 mg/L	Catalytic membrane reactor	pH 3.0	100 %	(Pinos et al. 2016)
5 mg/L	Reductive remediation	pH 2.0	97 %	(Dubey et al. 2017)
0.1 mg/L	Membrane biofilm reactor	pH 6.5-7.5	98.7 %	(Long et al. 2017)
1 mg/L	Conductive membrane	pH 7.0	95.2 %	(Liu et al. 2019)

1000 mg/L	Ion exchange	pH 2.0	100 %	(Kononova et al. 2019)
1000 mg/L	Adsorption	Ph 2.0-3.0	100 %	(Peng et al. 2021)

2.3 PHOTOCATALYSIS

2.3.1 Heterogenous Photocatalysis

Coupled semiconductors have acquired importance in photocatalysis, showing less recombination of electron-hole pairs. In the recent past, coupled semiconductors have been used for the photocatalytic reduction of Cr(VI) to Cr(III) under visible light (Marinho et al. 2017; Mavinakere 2018). TiO_2 is the widely used semiconductor for photocatalytic degradation, but TiO_2 works under UV light, and it also has charge recombination limitations. To overcome this problem, TiO_2 is severely doped with semiconductors like SnO_2, ZnO, ZrO_2 and CdS to improve the efficiency of the photocatalysts. The higher bandgap (3.2 eV) and photoexcitation in the UV region make TiO_2 less efficient in many applications (Tian et al. 2008). Coupling WO_3 with TiO_2 can enhance the photocatalytic ability by serving as electron-accepting species in the TiO_2-WO_3 complex (Ke et al. 2008). Likewise, the coupling can be achieved using many methods like physical mixing of metal oxides, multistep grafting, sol-gel method, co-precipitation method, impregnation, hydrothermal methods, ball milling, and flame spray technique.

Natural organic acids such as citric acid, oxalic acid, tartaric acid, and compounds bearing aliphatic or aromatic hydroxyl groups (collectively called hole scavengers) have been found suitable for Cr(VI) removal by reductive remediation (Dubey et al. 2017). The presence of additives is obligatory in order to ensure the photoreduction of Cr(VI). Scavengers facilitate the separation of the pair (electron/hole) by scavenging the photogenerated holes, thus decreasing the chances of charges recombination. The alcohols like methanol, ethanol can be used as hole scavengers. Acids like tartaric acid, oxalic acid, citric acid, EDTA. The hole scavenging efficiency is due to the presence of carboxylic group in their structure (Djellabi and Ghorab 2015). Citric acid can serve as a donor scavenger to deplete the photogenerated holes from TiO_2 based catalysts, increasing the reduction rate of Cr(VI) as which prevented the reoxidation of Chromium species by the holes or hydroxyl radicals (Yang et al. 2010).   These materials may cause various secondary pollutants, sludge and

most of the methods require highly sophisticated equipment, expensive chemical reagents, and high capital and recurring expenditures. These methods are not suitable for small-scale industries like electroplating, paint and pigments, etc. (Joshi and Shrivastava 2011; Ingole and Dharpal 2012; Fernando and Arachchi 2013). Xianzhi et al. prepared TiO_2-SiO_2 and TiO_2-ZrO_2 materials by the sol-gel method and showed better catalytic efficiency in the case of oxidation of ethylene. By coupling the semiconductors, they could obtain compounds with a higher surface area and enhanced thermal stability (Xianzhi et al. 1996). Li et.al prepared TiO_2-Cu_2O by electrochemical synthesis. Unlike photoreduction, pollutants can be oxidized and degraded using this coupled semiconductor. The coupling has helped in the production of a large number of holes in the interface and boosted the oxidation reaction (Li et al. 2004).

Cu_2O/$BiVO_4$ photocatalysts were forged through a hydrothermal coupled polyol strategy to extend the activity of the catalyst towards visible light. This study showed that the coupled catalyst exhibited improved photocatalytic activities than individual catalysts for the degradation of methylene blue dye. The p-n junction catalyst reduced the frequency of charge carrier recombination (Wang et al. 2013).

Lixia Yang et al. studied WO_3 doped TiO_2 nanotube (NT) arrays in the presence of citric acid under UV irradiation (Yang et al. 2010). Scavengers can be avoided by making the visible catalyst light active catalyst and enabling the reduction process to be economically viable. The incorporation of WO_3 into TiO_2 will inhibit the recombination of photogenerated holes and reduce the bandgap of TiO_2 to the visible light range. Singh et.al (2013) synthesised TiO_2 -WO_3 by the solution combustion method (Singh and Madras 2013).

Upadhyay et.al (2019) prepared a TiO_2-ZnO catalyst and investigated the dye degradation performance under visible light. ZnO and TiO_2 have limited activity in the UV range. The coupled semiconductors were obtained by the sol-gel method with a lower bandgap of 3.1 eV. The catalyst showed a higher degradation efficiency of 90% under visible light (Upadhyay et al. 2019).

There are studies on the application of TiO_2-SnO_2 photocatalyst for the degradation of textile dye like RhB under UV light, but there is no report on TiO_2-SnO_2 composites for heavy metal reduction (de Mendonça et al. 2017; Patil et al. 2018). The high concentration of doped Sn ions causes a decrease in the density of TiO_2, and the existence of both anatase and rutile phases in the TiO_2-SnO_2 heterojunction leads to high photocatalytic activity (Huang et al. 2015). The catalytic activity of pure SnO_2 is very poor and has limited

applications, whereas, in the coupled state, SnO_2 has applications in numerous fields like sensors, solar cells, and photocatalysis (Magdalane et al. 2019; Ong et al. 2018; Cai et al. 2018; Nasirian and Milani Moghaddam 2015; Zakrzewska and Radecka 2012). The addition of SnO_2 to TiO_2 leads to an intensification of photocatalytic activity towards pollutants (Singh et al. 2018; Hassan et al. 2019). Moreover, it is reported that the negatively charged Chromium (VI) species could be adsorbed onto the surface of metal oxide semiconductor sorbents if the sorbent's point of zero charges (PZC) is above the pH of the solution (Cheng et al. 2015).

Liu et al. suggest that the nanocomposite TiO_2-WO_3 may prevent the recombination limitations by extending the spectral response range. The WO_3 content will also result in increased surface acidity and, thereby, enhance the photocatalytic activity. The photocatalytic performance was investigated with the RhB pollutants. Under UV light, TiO_2 could excite easily, but under visible light the activity is limited due to its wider bandgap. Liu et al. (2014) synthesised TiO_2-WO_3 catalysts by a one-pot hydrothermal method. TiO_2-WO_3 heterojunction helps in preventing photogenerated electron-hole recombination. Excited electrons on TiO_2 are transferred to the CB of WO_3, while holes remain in the VB of TiO_2 due to a difference in their energy levels (Dozzi et al. 2016). This effective separation will improve the photocatalytic activity of the TiO_2-WO_3 catalyst. The size of the catalyst obtained is in the range of 10.1-10.9 nm. The 1:99 (W:Ti) catalyst showed a 95.48% RhB reduction efficiency (Liu et al. 2014a).

The report by Mendonca et al. suggested that the hydrothermal annealing favoured the crystal growth, which is beneficial in improving the photocatalytic activity of the TiO_2-SnO_2 heterostructure. The report shows that the longer treatment has caused interface formation between two TiO_2 particles, which could act as recombination centres for photogenerated charge carriers and result in the depreciation of photocatalytic activity (de Mendonça et al. 2017). From all the reported methods, the hydrothermal method yields lower catalyst size, higher surface area, less time consumption, and better photocatalytic activity.

2.4 PHOTOREDUCTION OF Cr(VI)

In recent past, coupled semiconductors are used for the photocatalytic reduction of Cr(VI) under visible light (Marinho et al. 2017a; Mavinakere Ramesh and Shivanna 2018). Photocatalysis is a highly effective and economical process compared to other treatment

methods (Joshi and Shrivastava 2011). The direct use of sunlight/ UV light to activate the reduction reaction at ambient conditions without the consumption of reducing agents and absence of any secondary pollutants are the main advantages of photocatalytic processes (Li et al. 2018).

Different metallic oxides, oxynitrides, oxychlorides, oxysulphides, and sulfides have been explored for the photoreduction of Chromium (VI). Due to the wide bandgap, low electron mobility, fast charge carrier recombination, and low light conversion efficiency, a single semiconductor material has commercial limitations (Ahmed et al. 2019). Compared with a single photocatalyst, their hybrid materials can exhibit superior photocatalytic activity, improved optical properties, and thermal stability. The light absorption capacity of a catalyst can be shifted to the visible region by effective charge transfer and the synergistic effect of combining two different metal oxides. The conduction band (CB) and valence band (VB) are involved in the reduction-oxidation processes of a semiconductor.

The nanocomposite of TiO_2 and a metal oxide semiconductor with a smaller bandgap, such as WO_3, has revealed the potential mechanism of photoreduction. The photo-induced electrons will transfer from the CB edge of TiO_2 to the CB edge of WO_3. The electrons accumulated on WO_3 domains will be transferred to the active species like H^+ ions in the solution. In contrast, holes that remain in the valence band (VB) of TiO_2 will induce OH^- radical production by the oxidation of H_2O molecules. Photo-holes cannot be used for the reduction of Cr(VI) to Cr(III). Also, the $^{\bullet}OH$ radicals produced as a product of oxidation of water will induce a reverse reaction of Cr(III) oxidation to Cr(VI). The studies on different synthesis methods of TiO_2-WO_3 catalyst and TiO_2 coupled with wide bandgap material SnO_2 is given in table 2.3.

The slower activity of TiO_2-WO_3 can reduce the formation of $OH^{\bullet}$ radicals and will not require any additional hole scavengers. Chromium reduction consumes protons in the acidic solution. A higher concentration of H^+ in lower pH (less than pH 3.0) will yield a faster Cr(VI) reduction. The lower pH favours the reduction reaction as the thermodynamic driving force of an electron from a CB to Chromium (VI) increases at a lower pH. Moreover, TiO_2 will be positive charged at lower pH, favouring the adsorption of negatively charged chromate species onto the surface of TiO_2 (Wu et al. 2013).

Table 2.3 Photocatalysts synthesis methods

Sl. no	Reference	Synthesis method	Inference	Efficiency and experiment conditions	Application
1.	(Jentoft et al. 1997)	Ball milling	The surface area obtained is 80 m^2/g	-	Catalysis
2.	(Anandan et al. 2014)	ultra sound assisted method	33.39 nm with a higher surface area of 1.38 m^2/g.	100% (pH 6, 1 g/L catalyst loading)	MB dye degradation
3.	(Liu et al. 2014)	One-pot hydrothermal synthesis	10.1-10.9 nm. 1:99 (W:Ti)	95.48 %	Degradation of Rhodamine B
4.	(He et al. 2016)	Co-precipitation method	Surface area- 88 m^2/g	-	Reduction of NO by NH_3
5.	(Dozzi et al. 2016)	Sol-gel method	Size - 2-20 nm, surface area- 88 m^2/g.	100 %	Cr(VI) reduction and formic acid oxidation
6.	(de Mendonça et al. 2017)	The hydrothermal annealing method	Size- 5 and 20 nm	100 %	Degradation of RhB
7.	(Patil et al. 2018)	Wet impregnation method.	Size 10-25 nm Surface area - 70.41 m^2/g	100%	NH_3 gas sensing and mineralization of congo red dye
8.	(Hu et al. 2018a)	Sol-gel method	Size 12.28 nm	HC -10.56 %, NOx - 34.76 % and CO - 6.01 %	Decomposition of vehicle exhaust
9.	(Mugunthan et al. 2019)	Hydrothermal method	Size 50-102 nm, Surface area - 113 m^2/g	100% diclofenac removal	Degradation of diclofenac
10.	(Hassan et al. 2019)	Sol-gel method	Size 6.9-23.5 nm, Surface area 33.5 m^2/g	Xanthene - 93.5% MB and RhB-100% Phenol-90%	Xanthene synthesis, RhB, MB and phenol degradation

The other factors influencing the Cr(VI) reduction includes solution pH, initial concentration of pollutant, catalyst loading and light intensity. The pH of the solution is one of the most critical parameters in the photocatalytic process. The acidic pH favours the Chromium reduction over the alkaline pH. Many papers have published on photoreduction under acidic pH from 1.0-6.0 (Sane et al. 2018; Testa et al. 2004; Athanasekou et al. 2017). The effect of pH on the reduction of Cr(VI) depends on the electrostatic attraction between the sorbent and chromate ions.

On irradiation, the accumulated photoinduced electrons from the WO_3 domains will be transferred to H^+ ions in the solution while the holes remain in the VB edge of TiO_2. By employing three electrons to the Chromium (VI) ions, H^+ species converts them to Cr(III),when in the absence of reducing agents, H_2O accepts the holes (Liu et al. 2014a). The functional groups containing -O- on the surface can absorb Cr(III) to the surface of the catalyst (Xu et al. 2018). The coupling of metal oxide semiconductors can provide excess -O- groups. The anticipated photocatalytic reduction pathways under visible light in an acidic media and at a basic pH (Marinho et al. 2017a) can be expressed as

For acidic medium,

$$H_2CrO_4 + 6H^+ + 3e^- \quad \rightarrow \quad Cr^{3+} + 4H_2O \hspace{3cm} \rightarrow (2.0)$$

$$HCrO_4^- + 7H^+ + 3e^- \quad \rightarrow \quad Cr^{3+} + 4H_2O \hspace{3cm} \rightarrow (3.0)$$

For basic medium,

$$CrO_4^{2-} + 4H_2O + 3e^- \quad \rightarrow \quad Cr(OH)_3 + 5OH^- \hspace{2.5cm} \rightarrow (4.0)$$
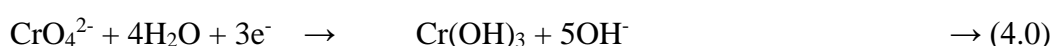
In an acidic pH, H^+ions will make the surface of the catalyst positive and enhance the adsorption of negatively charged metallic particles onto it (Sane et al. 2018). Any fair amount of catalyst can accelerate the reduction reaction, but in several cases, catalyst loading showed a negative effect on photoreduction (Khalil et al. 1998). The optimum catalyst loading is a balance between the generation of free radicals and the light screening effect due to the excess amount of catalyst. In general, depending on the nature of the target chemical and the catalyst, the optimum loading may differ (Sane et al. 2018). The initial concentration also affects the Cr(VI) reduction. As the initial concentration increases, the rate of Cr(VI) reduction decreases. A possible explanation would be the fact that increased Cr(VI) concentration increases the solution absorbance and, therefore, a lion's share fraction of the light is intercepted before reaching the catalyst surface, thus decreasing the

degree of reduction. The table (2.4) below summarizes information from the literature on the various photocatalysts used to reduce Chromium (VI).

Table 2.4 Different photocatalysts for the photoreduction of Chromium (VI)

Catalyst	Catalyst loading	pH	Scavenger	Light source	Removal Efficiency	Reference
Titania	0.1 g/L	2.0	Oxalic acid	450 W Xenon arc lamp	97%	(Testa and Qu₁ 2004)
Ag(NO₃)-doped TiO₂	1.6 g/L	3.0	-	UV light	38.1%	(Ma et al. 2012)
TiO₂ impregnated glutaraldehyde-crosslinked alginate beads	10 g/L	2.0	Fe(III)	UV light	100%	(Liu et al. 2013b)
TiO₂	1 g/L	2.0	Hydrogen peroxide	Solar collector	92%–99%	(Singh and Chaudhary 2013)
Nanotitania	0.1 g/L	7.0	-	15 W White fluorescent lamps	42.92%	(Paul et al. 2015)
ZnO/TiO₂	1 g/L	-	-	125W medium-pressure UVC lamp	99.99%	(Naimi-Joubani et al. 2015)
TiO₂ (Evonik P25)	2 g/L	2.5	Methanol	9 W UVA lamp (Radium Ralutec)	100 %	(Valari et al. 2015)
TiO₂	2 g/L	2.2	Tartaric acid 60	Natural sunlight	60.25%	(Djellabi et al. 2016)
CP2	0.75 g/L	2-3	-	300 W Xenon lamp with UV cut-off filter	100 %	(Djellabi et al. 2020)
Fe₂O₃	0.5 g/L	3.0	Tartaric acid	300 W Xenon lamp with UV cut-off filter	100 %	(Djellabi et al. 2021)

2.5 MEMBRANE SEPARATION OF Cr(VI)

Several methods have recently been developed and optimized for the fabrication of TiO_2 based photocatalytic membranes. Among them are dip-coating or spin-coating of porous supports using TiO_2 sols, filtration of TiO_2 nanofibers through glass filters followed by hot pressing or liquid phase pressurization, hydrothermal growth of free-standing TiO_2 nanowire membranes, anodization of titanium films sputtered on to stainless steel substrates, embedding TiO_2 nanoparticles into the matrix of the polymeric membrane collectively called as photocatalytic membrane reactor, electrospinning TiO_2 fibres or flat membranes by recasting, development of TiO_2 layers with rapid atmospheric plasma spray coating and the fabrication of free-standing and flow-through TiO_2 nanotube membranes. In a photocatalytic membrane reactor, photocatalysis and membrane filtration take place simultaneously. In this, not only pollutant filtration takes place but also degradation occurs simultaneously. The photocatalytic membrane reactors consist of nanoparticles in a slurry form in contact with a membrane or nanoparticles coated on the membrane.

Anderson et al., 1988 reported the synthesis of Titania and alumina ceramic membranes using alkoxide as starting material via the sol-gel method. In 2000, Wu et al. reported the effects of calcination temperature on the performance of TiO_2-based tubular membranes. Due to the phase shift of TiO_2 anatase to rutile during calcination, the membrane's pore size grew as the temperature rose. In 2009, Zi et al.; reported about a TiO_2 membrane on porous stainless-steel support and TiO_2 membranes with 0.08-0.2 µm thickness were prepared.

Hierarchical assembly of photocatalysts on polymer membranes has gained importance due to the easiness of catalytic recovery from the reactor. The hierarchical membranes consist of a support polymer membrane on which a thin film of photocatalytic nanoparticles is coated. The nanoparticles can be coated on membranes by different methods. The pressure filtration can yield a thin coat of nanoparticles on the membrane. The main challenge of hierarchical membrane preparation is to create microscopic pores that can maximize both nanoparticle loading and water flux. High water flux requires low friction and thus large pores. High particle loading requires a large surface area and thus small pores (Wang et al. 2013).

Surface-located TiO_2 polymer membranes are prepared through dip-coating or self-assembly chemical or photochemical processes based on chemical grafting and photopolymerization and physical deposition of a TiO_2 layer via ultrafiltration of a TiO_2

suspension through polymer membrane ultrafiltration. Photocatalytic polymeric membranes can be used for disinfection and pollutant removal.

In the dip-coating or self-assembly method, a layer of TiO_2 is coated on the surface of a membrane by dipping the membrane into a sol-gel TiO_2 slurry solution, followed by drying and pressing with compressed gas. The TiO_2 particles tend to self-assemble on the membrane due to the anchoring effect of the functional groups (e.g., carbonyl, sulfone) located on the membrane surface or through hydrogen bonding between the membrane surface groups and TiO_2. In the chemical grafting method, appropriate monomers containing the photocatalyst are immobilized and initiators are photo-irradiated on the support.

In the physical deposition method, the photocatalyst is physically deposited on the membrane surface through pressure-driven filtration of the photocatalyst suspension slurry. A photocatalyst cake builds on the surface of the membrane, the thickness of which can be controlled by varying filtration time and operational pressure. Bai et al. synthesized TiO_2 nano thorn spheres and assembled them on a piece of cellulose acetate polymer membrane through compression on a dead-end filtration set-up. The resulting TiO_2 nanothorn membrane was reported to exhibit a hierarchical porous structure, which gave a high-water flux and a multifunctional TiO_2 surface for mitigation of membrane fouling (Alex T Kuvarega and Bhekie B Mamba 2018).

Choi et al reported a novel dip-coating process to synthesize hierarchical multi-layer mesoporous TiO_2 membranes. Improved performance could be achieved by employing a surfactant templating strategy in an acetic acid-based sol–gel route. By multicoating a porous alumina support layer with various sols at different surfactant concentrations in succession, an asymmetric, three-layer TiO_2 membrane was obtained (Choi et al. 2006).

Ranjith and Rajendra Kumar reported hierarchical forms of self-assembled zinc oxide (ZnO) photocatalyst with a flower-like structure. It was synthesized by aqueous solution-based precipitation. It showed visible photocatalytic degradation efficiency of 98% against methylene blue (MB) dye in 120 min under natural solar irradiation and visible irradiation. The optically active defects played a vital role in improving the photocatalytic properties during both UV and visible irradiation (Ranjith and Rajendra Kumar 2017).

The PANI-based hierarchical structure is also reported in the literature. A Hierarchical PANI-electrospun polystyrene fibre composite was prepared for the detection and removal

of heavy metal ions from aqueous media. Nanowoven PANI− PS mats exhibit interesting properties in their interaction with heavy metal ions. Their high adsorption capacities toward dispersed Hg(II), Cd(II), Pb(II), Cr(VI), and Cu(II) ions make them promising materials for water remediation. PANI chains are organized into rod-like nanostructures that offer an increased surface area for the interaction with heavy metal ions dispersed in an aqueous solution (Alcaraz-Espinoza et al. 2015). In this work, PANI-coated coupled semiconductor incorporated polymer membranes will be prepared and applied in heavy metal removal. The photocatalytic degradation and membrane filtration will be carried out in a single photocatalytic membrane reactor.

2.6 POLYMER MEMBRANES FOR Cr(VI) REMOVAL

2.6.1 Composite membranes

Membrane separation has been widely used for the removal of inorganic pollutants in wastewater since1960. Among membrane separation, mixed matrix membranes (MMM) have gained more importance in the past few years. The composite membranes have enhanced properties like higher adsorption capacity, high rejection, and high permeate flux and all because of the synergistic effect of polymers and the inorganic additives (Arif et al. 2020; Mukherjee et al. 2015; Yong Ng et al. 2013). The different polymer composite membranes reported in the literature for the removal of Cr(VI) are tabulated in table 2.5.

Table 2.5 Polymer composite membranes for the removal of Cr(VI)

Polymer	Nanoparticle	Mode of operation	Membrane casting method	Cr(VI) concentration and pH	Rejection efficiency	Reference
PSf (aminated)	TiO$_2$	UF	NIPS	10 mg/L, acidic pH, 100 KPa	92 %	(Jyothi et al. 2016)
PVA	CNT	UF	-	20 mg/L	99 %	(Duan et al. 2017)
PAN		UF	-	<25 mg/L pH> 7	>90 %	(Muthumareeswaran et al. 2017)
PVDF	CNT/Stainless steel	UF	NIPS	1 mg/L pH 7	95.2 %	(Liu et al. 2019)

Polyamid	-	RO	-	4200 mg/L, pH 6.6, 4 MPa pressure	100 %	(Mohammed and Sahu 2019)
PVDF	TiO$_2$	UF	NIPS	8 mg/L, 6.1 pH	92 %	(Arif et al. 2020)
PES	Nano zerovalent iron/TiO$_2$	UF	NIPS	5 mg/L, pH 3	100 %	(Kazemi et al. 2020)

Among TiO$_2$ based MMMs, the heterojunction between TiO$_2$ and WO$_3$ can significantly yield better separation efficiency of charge carriers to be used in a photocatalytic membrane reactor (Zhao et al. 2021). In our work, we have selected PANI as the membrane material due to its doping-dedoping properties, membrane forming capability, higher affinity for Cr(VI) at acidic pH, and environmental stability.

2.7 POLYANILINE

Polyaniline exists in three forms based on the degree of oxidized monomer blocks, namely, fully oxidized pernigraniline, partially oxidized emeraldine, and fully reduced leucoemeraldine. Among these, pernigraniline and leucoemeraldine exist as salts or bases, and the emeraldine salt form is electrically conducting. The leucoemeraldine consists of benzene and an amino group, which slowly oxidizes in the air. Pernigraniline consists of alternating aminobenzene and quinonediimine fragments. The quinonediimine groups are unstable in water and decompose easily. Emeraldine salt is formed by doping of emeraldine base by organic acids. In acid doping, the protons primarily react with nitrogen atoms of imine groups and polycation formation occurs (shown in fig 2.1). The protonation of PANI produces the electronic defects in the polymer chain such as polarons and bipolarons, which are due to the addition of protons to the neutral polymer chain (Li et al. 2013).

Doping of PANI by hydrochloric acid, sulfuric acid (H$_2$SO$_4$), perchloric acid (HClO$_4$), phosphoric acid (H$_3$PO$_4$) has been reported in the literature. Organic acids with low molecular weight, such as acetic acid, formic acid, propionic acid, and high molecular weight long-chain organic sulfonic acids like camphor sulfonic acid, dodecylbenzene sulfonic acid (DBSA), methanesulfonic acid, can be used to dope PANI. The dopant ions

can alter the properties like crystallinity, permeability, processibility, and conductivity of PANI.
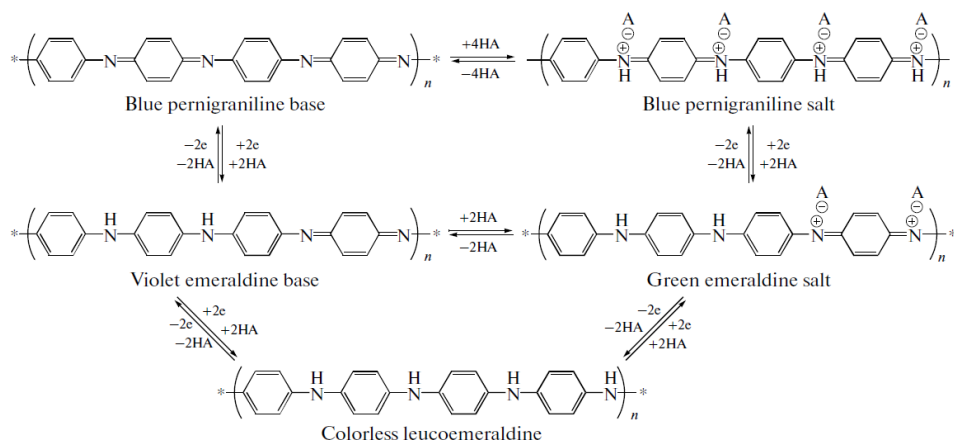
Figure 2.1 Different oxidation states of PANI (Boeva and Sergeyev 2014)

Due to increase in positive charge of the polymer which is localized on neighbouring nitrogen atoms, the total energy of polymer increases and it leads to the redistribution of electron density. Thus, unpairing of the lone electron pair of nitrogen atoms occurs without changing the number of electrons in the system. The cation radicals start delocalizing over a conjugation length and provide the conductivity of the polymer. The conductivity of PANI increases to ten-fold as the degree of protonation increases from 0-20%. The delocalization of PANI radical cations occurs either by an intermolecular or intramolecular mechanism, and the polymer should be oriented in one direction to ensure the transfer of π-electrons from one polymer chain to the another (Boeva and Sergeyev 2014).

2.7.1 PANI Nanocomposites for the environmental remediation

Polyaniline have been used as a binder, dopant, and as a pore forming agent by several research works to prepare composite materials (shown in table 2.6). The application of PANI-inorganic/organic composite includes water remediation, gas separation, and in fuel cells, etc.

PANI could improve the mechanical, chemical, and hydrophilic properties of nanocomposites. It was reported that the addition of PANI nanostructure increases the membranes' final active surface area and gives them new functionalities. Alcaraz-Espinoza et al. prepared PANI-(Electrospun Polystyrene) fibres for heavy metal remediation.

Table 2.6 PANI inorganic/organic materials composites

Membrane materials	PANI composites	Advantage of PANI incorporation	Application	Reference
PS	PS and PANI Composite	Enhanced electrical properties and wettability	Water remediation	(Liu et al. 2014)
PSf	TiO_2-PANI as hydrophilic additives	Improved permeability, higher hydrophilicity and antifouling property	Purification of water	(Pereira et al. 2014)
PSf	PANI as dopant	Improved porosity and selectivity	Purification of gas,liquid and electrolyte solutions	(Kurada and De 2018)
Sulfonated BC-PANI	Sulfonated bacterial cellulose and PANI composite	Bacterial cellulose has excellent water holding capacity and mechanical properties, High ionic conductivity, biocompatibility	Gel polymer electrolyte	(Yue et al. 2017)
PANI HFM	GO nanoparticle	Improved adsorption and hydrophilicity	microextraction techniques for the analysis of Ivermectin in environmental	(Rezazadeh et al. 2018)
PANI	PANI-Electrospun PS fiber Composite	Enhanced electrical properties and wettability	Heavy metal remediation	(Alcaraz-Espinoza et al. 2015)
PSf UF membrane	PSf-PANI/TiO_2 nanocomposite	hydrophilicity, water permeability, and better antifouling property with high rejection high porosity, surface area per volume	Fouling resistance of PSf membrane	(Teli et al. 2013)
polyaniline (PANI)-silica mesocomposite (PSM),	PANI silica meso-and nanocomposite	High thermal and mechanical properties, excellent friction	Comparative study of effect of inorganic fillers	(Chang et al. 2014)

nanocomposite (PSN) and PANI-raw silica (PRSN) membranes		and wear properties		
PANI/PVDF membrane support	Polyaniline composite membrane	Various acid dopants increase electrical conductivity and mechanical stability	Pressure filtration	(Rohani et al. 2017)
Sulfonated PES	Polyaniline coated sulfonated TiO_2 nanoparticles	Enhanced chemical, mechanical properties, Sulfonation increases hydrophilicity and conductivity	Membrane fuel cell	(Elakkiya et al. 2018)

A hierarchical PANI-PS composite was synthesised, and it was used to detect and remove heavy metal ions from aqueous solutions (Alcaraz-Espinoza et al. 2015). Lina Yue et al. (2017) prepared gel polymer electrolyte out of sulfonated bacterial cellulose-PANI composites. The superhydrophilicity of bacterial cellulose and the ion transport capability of PANI have enhanced the properties of the polymer electrolyte membrane. Repeated imine groups in PANI have acted as a weak Lewis base site effective for ion hopping.

Gu et al. prepared TiO_2/PANI and used it as an effective visible catalyst. PANI in TiO_2 can act as a template to stabilize TiO_2 particles at nanoscale through interfacial chemical bonds, and the TiO_2 anatase to rutile conversion can also be suppressed. The recent techniques used to prepare TiO_2 nanocomposites include the composite template supported method, the organic capped method, and surfactant-directed methods. These types of nanocomposites cannot be easily removed from the reaction mixture, and the removal by calcination leads to the change of partial morphology. The conducting polymers like Polyaniline offers higher efficiency due the properties like higher light and thermal stability and better recycling capacity. Conducting polymers with a conjugated backbone possess high absorption capacity in the range of visible light and also possess easier charge separation properties (Gu et al. 2012).

According to Vellaichamy et al., the reason for the poor mechanical stability of PANI is its morphological changes in doping and dedoping processes. But, the other inorganic PANI

composites, such as PANI/SiO$_2$, PANI/RuO$_2$, showed superior properties such as high conductivity, high surface area, better porous nature, and good environmental stability. Under acidic pH, MnO$_2$ possesses a negative charge and TiO$_2$ possesses a positive charge, and the TiO$_2$ binds with MnO$_2$ electrostatically. TiO$_2$/MnO$_2$ particles are encapsulated with PANI and forms a new nanocomposite material and used for Cr(VI) reduction. It was reported that under acidic pH, degradation of HCOOH occurs and in the presence of H$^+$ ions, reduction of Chromium anion occurs in the reaction mixture (Vellaichamy et al. 2017a).

Ning Wang et al. and co-workers reported the synthesis of PANI/TiO$_2$ for the removal of phosphate ions from wastewater. The high adsorption capacity of PANI, particularly at low pH (1-6) and the imine-amine groups of PANI act as adsorption sites for pollutants. Factors such as electrostatic interaction, ion exchange, hydrogen bonds, and Ti-Phosphate interaction favour the adsorption process. The dedoping properties of PANI helped in the desorption of phosphate and the regeneration of nanocomposite (Wang et al. 2017). PANI/TiO$_2$ has much adsorption capacity for Cr(VI) than other materials (Deng et al. 2019).

Besides an adsorption material, PANI was also used as an excellent photocatalytic material in photocatalysis studies. The sensitization of TiO$_2$ by PANI increases the photoresponse to the visible light and helps to enhance the photocatalytic activity of the composite. TiO$_2$/PANI was successfully used for the degradation of methylene blue dye under visible light (Wang et al. 2010). The major drawback in the process is the recovery of the composite after the degradation studies.

The incorporation of nanoparticles in the membrane helps in the development of photocatalytic membranes, which have the synergistic effect of catalytic degradation and membrane separation, which avoids difficulties such as,

❖ No need for separation and recycle the catalyst.
❖ TiO$_2$ nanoparticle can induce photocatalytic ability to the membrane
❖ Improves hydrophilicity and fouling mitigation.
❖ Contaminants could be decomposed in feed or permeate.

PANI as a filler in polymer membranes has been used for different applications. Polysulfone-PANI/TiO$_2$ nanocomposite ultrafiltration membranes have been used to enhance fouling resistance. TiO$_2$ emerges as a functional nanomaterial with high chemical

stability, nontoxicity, and good heat resistance. PANI helps to reduce the agglomeration of nanoparticles. PANI membranes have tuneable hydrophilicity and hydrophobicity. Undoped PANI membrane appeared to be more hydrophobic in nature, whereas doped PANI membrane is hydrophilic in nature. Emeraldine base form of PANI is soluble in most organic solutions, and these properties make PANI an ideal material to use in membrane applications. Membranes with PANI nanofiber incorporation were demonstrated significant improvements in permeability, water absorption, and contact angle values (Pereira et al. 2014).

Elakkia et al. prepared sulfonated TiO_2-PANI composite membranes for membrane fuel cells. They could enhance the overall hydrophilicity of the composite membrane and its ability to absorb more water molecules. It could facilitate a path for the transport of protons across the PANI matrix. Ion exchange capacity was improved due to the presence of sulfonic acid groups and amine groups. Rohani et al. reported that the existing selective polymer membrane can be modified using conducting polymers. The membrane free volume can be tuned using various electrolytes, which control the key properties like diffusivity and permeability (Elakkiya et al. 2019).

The nanoparticle-induced membranes will have the properties of both the polymeric material and nanostructures. The performance of the membranes can be enhanced via surface as well as internal modification (Nadig et al. 2021).

2.7.2 POLYANILINE- Membrane material

Scientists became interested in PANI membrane research 25 years ago. They reported on the PANI film casting technique using N-methyl-2-pyrrolidone solvent and the conductivities of the membranes when doped with various organic acids (Geng et al. 1997). The properties of PANI such as low cost, easier synthesis, suitable MWCO, unique doping-de-doping mechanism, easier casting capacities, tunable range of filtration, chelating, robust structure, environmental- mechanical- chemical stability has made the CP such as PANI (an organic metal) a more functional material (Karthik and Meenakshi 2015; Liu et al. 2019; Monjezi et al. 2018; Rohani et al. 2017a; Rosaih Rohani, Izzati Izni Yosoff 2018; Sahu et al. 2019),(Li et al. 2018a).

In 1998, Mirmohseni et al reported that PANI membranes can be tuned by applying an external electric field to alter the oxidation state of the PANI and further permeability of

the PANI membrane can be enhanced. It has been discovered that acid travels across the barrier devoid of any external driving force, enabling conductive ultrafiltration and nanofiltration. The properties of the PANI membrane have been tuned by applying an external electric field. Dodecylbenzene sulfonic acid (DBSA) was selected as the dopant for the conductive membrane due to its long alkyl side chains for stability and strong acidic group for conductivity. The conductive PANI membrane exhibited significant mitigation of membrane fouling under the application of negative voltage and the antifouling performance improved with the applied voltage increasing from 0 to 1V. While applying external voltage, the electrostatic repulsion is created between the PANI surface and model foulants. The fouling layer becomes loose on the membrane's surface, because of which hydraulic resistance decreases and flux reduces. The undoped membrane was fouled during the experiment (Mirmohseni and Saeedi 1998).

A PANI membrane can be used for separating acetic acid from aqueous solutions. The high chemical and environmental stability of PANI makes it a doting material for acidic environments. In an acidic pH, PANI will be in its emeraldine state. Acetic acid is an important chemical intermediate in the syntheses of vinyl acetate, terephthalic acid, cellulose ester, and other esters. Polyaniline can be cast as free-standing, dense films with pore sizes (<20 Å diameter) which can be used for reverse osmosis, pervaporation, and gas separation membranes. Membranes show selectivity for important gas pairs, such as the selective permeation of oxygen over nitrogen. The doping/undoping process leads to morphological and chemical changes that affect both the permeability and selectivity of polyaniline. Polyaniline membranes, in their base form, are quite hydrophobic; i.e., water does not wet their surfaces. As the polyaniline is doped, the positive charge of the polymer and the negative charge of counterions increase the polyaniline's hydrophilicity.

Natalia et al. explain the possibility of movement of acid dopants. Acid dopants in the steric positions swell slightly, and it would reduce free volume in the membrane and resist water flow across the membrane.

The ability of doped PANI films for gas separation was explained by Sairam et al. The doping process could control the morphology and porosity of PANI membranes. They confirmed that doped PANI films can be used to separate water/organic acid mixtures. It has been concentrations above 5–6 wt.% of PANI may lead to gelation. They have used secondary amines to reduce gelation of PANI solution. To achieve PANI membranes of

higher mechanical stability, PANI membranes can be prepared using high molecular weight PANI EB powder. Crosslinking can be done to ensure stability in organic solvents in PANI membranes. The literature on application of Polyaniline in different areas are tabulated in table 2.7.

Table 2.7 Polyaniline in different separation applications

Polymer	Method of preparation	Enhanced properties	Application	Reference
PANI	-	Permeability selectivity	Separation of acids	(Mirmohseni and Saeedi 1998)
PANI	Non-solvent induced phase separation NMP as solvent	Temperature stability Permeability selectivity	Pervaporation	(Huang et al. 1998)
PANI	Non-solvent induced phase separation NMP as solvent	High conductivity, mechanical strength Selectivity and permeability	Gas, liquid and electrolyte purification	(Sairam et al. 2006)
PANI membrane	Phase inversion	Higher flux at higher temperatures	Organic solvent filtration	(Sairam et al. 2009)
PANI/PVDF on stainless steel meshes	-	Under water super hydrophobic, superoleophobic membranes	Separation of oil in water emulsion	(Liu et al. 2016)
PANI and PS	Tetrachloroethylene solvent	Improved ion exchange characteristics Improved thermal stability	Fuel cell	(Amado et al. 2005)
PANI membrane	Phase inversion	Selectivity and permeability	Electrical tuneability	(Wang et al. 2019)
PANI membrane	Non-solvent induced phase separation NMP as solvent	Permeability Good conductivity hydrophilicity	Mitigation of membrane fouling	(Wang et al. 2019)

In a doped PANI membrane, conductivity of the membrane is the result of an increase in the positive charges focused on nearby nitrogen atoms, which raises the total energy of the

polymer and causes the electron density to be redistributed. Thus, unpairing of the lone electron pair of nitrogen atoms occurs without changing the number of electrons in the system. The cation radicals start delocalizing over a conjugation length and provide the conductivity of the polymer. The conductivity of PANI increases to ten-fold as the degree of protonation increases from 0-20%. The delocalization of PANI radical cations occurs either by intermolecular or intramolecular mechanism and the polymer should be oriented in one direction to ensure the transfer of π-electrons from one polymer chain to the another.

2.7.3 Preparation of PANI membrane

Polyaniline can be fabricated as a freestanding, dense film with pore size of 20 A^o diameter, which can be used in reverse osmosis, pervaporation, nanofiltration and gas separation applications (Sairam et al. 2006). Phase inversion technique offers a membrane morphology with relatively dense selective upper layer to a fully porous bottom layer with large macrovoids. The hydrophilicity of the membranes can be estimated by measuring the apparent contact angle of the membrane surface. The contact angle less than 90° indicates a hydrophilic membrane (Alhweij et al. 2021).

The rheological characteristics of the EB/2-methylaziridine (2-MA)/NMP system have been reported by Mattes et al. where a higher concentration of EB was used (15-40 mass %). The poor solubility of EB in NMP is due to the hydrogen bond formation. 2-MA interact with EB in NMP by forming hydrogen bonds without degrading the polymer. The EB/2-MA bonding continues and EB-EB interaction decreases in the solution. The viscosity of polymer solution is a measure of EB and 2-MA interaction. Hydrogen bond occurs between the amine protons of 2-MA and the lone pair electrons of the imine nitrogen of EB (Yang and Mattes 2002).

Norris et al. fabricated asymmetric Polyaniline hollow fibres by phase inversion method using 4-MP (4-methylpiperidine) as a gel inhibitor. Number of gel inhibitor molecules per EB tetramer repeat unit was maintained between 1 and 1.2. They have been able to prepare 15-20% PANI membranes. It has been reported that 4-MP is more suitable for anti-gelling than methylaziridine (2-MA). The polymer solution for casting was prepared by homogenously mixing the EB powder/4-MP/NMP at 280 rpm for 4 hours (Norris et al. 2005).

Sairam et al. prepared PANI films by dissolving PANI EB powder in NMP solvent using a mortar and pestle. PANI membranes of 40-100 um thickness was prepared by solution casting method (Sairam et al. 2006).

Chapman and co-workers prepared PANI membranes from the inhouse prepared PANI EB powder at -15°C and lithium chloride as the anti-freezing agent. The PANI membrane was prepared by phase inversion method and further the membranes underwent heat treatment to create a cross-linked, solvent-resistant membrane. Heat treatment of the membrane reduces the re-dispersion of the membrane in aprotic solvents (Chapman et al. 2008).

Huang et al. prepared poly (n-2-hydroxymethyl aniline) which is also called as n-PANI, from its monomers via chemical oxidative polymerization. The UF membranes were prepared by dissolving 30 wt% n-PANI in NMP without adding any anti-gelation agent. The n-PANI membranes were highly hydrophilic in nature and displayed a lower contact angle of 36 degrees. According to them, the pure PANI membranes did not exhibit satisfactory protein selectivity for typical UF operation. Additionally, the introduction of secondary amines like 4-methyl piperidine (4-MP) improved the membrane processability and remaining 4-MP reduces hydrophilicity (Huang et al. 2015a). The schematic diagram for the interaction of PANI/4-MP/NMP are shown in figures (2.2 and 2.3).
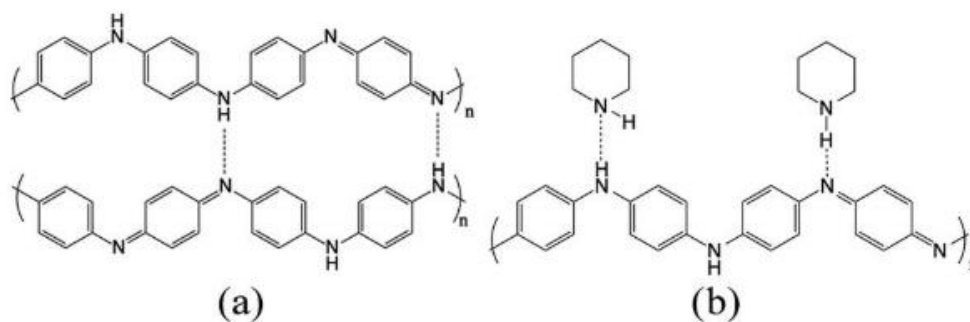
Figure 2.2 (a) Gelation of PANI caused by intermolecular hydrogen bonding (b). 4-MP inhibits PANI from gelling by holding some of the bonding sites (Huang et al. 2015).

The PANI membranes were prepared by nonsolvent induced phase separation (NIPS) method where 20 wt% PANI EB powder was dissolved in NMP and 4-MP (6.5 %) solvents. The reaction mixture was stirred for 4 hours to get casting solution. The solution then kept overnight for degassing. The membrane thickness was maintained at 250 um and the membranes were doped using HCl before the experiments. The membranes showed asymmetrical structure with four structural layers namely dense top skin layer, transitions region, a porous layer and non-woven support layer.
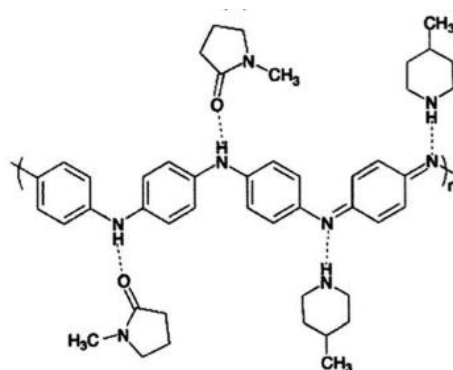
Figure 2.3 The schematic diagram of PANI/4-MP/NMP complex formed by hydrogen bonding.

However, the structure of the membranes depends on both the thermodynamic interactions and the phase inversion kinetics. To prepare mechanically stable PANI films, the PANI EB with higher MWCO can be prepared at lower temperatures at 5°C and 15°C (Xu et al. 2018).

Monjezi et al. prepared PANI nanofiltration membranes for the separation of solvent from dewaxed lube oil. The membranes were obtained by dissolving 16.7 wt% PANI EB powder in NMP/4-MP mixture and maleic acid was added for the cross linking of the PANI polymer. The solution was casted on a woven polyester fabric fitted with the glass plate mounted on a laboratory made film casting machine. The 250 um membranes with asymmetrical structures were obtained using this method (Monjezi et al. 2019).

2.8 PHOTOCATALYTIC MEMBRANE REACTORS (PMR)

PMRs have gained the interest of many researchers. The PMRs combines both the photocatalytic and membrane module in a single unit. The membrane techniques such as nanofiltration, ultrafiltration and microfiltration can be utilized to prepare photocatalytic membrane reactor. The main advantage of combined process is reduced size of installation and reuse of catalyst in further runs (Mozia et al. 2007). Photocatalytic membrane preparation can be obtained by two methods, membrane material modification and surface modification. The photocatalyst can be suspended in the reactor (Type I) or can be embedded and coated on the surface of the membrane (Type II). The main advantage of catalyst immobilized membranes over photocatalytic suspension includes easy recovery of nanocatalyst, small foot prints, low capital cost of infrastructure (Nair and Jagadeesh 2017),

(Bai et al. 2010). The recent details about the photocatalytic membrane reactor are listed in Table 2.8.

Table 2.8 Photocatalytic membranes for different applications

Membrane material	Configuration	Light source	Photocatalyst	Application	Major findings	Reference
Commercial membranes	Type I	500 W medium pressure mercury lamp	Degussa P25 TiO_2	Degradation of 4-nitrophenol	50% degradation with immobilized state and 80% photodegradation with suspended catalysts	(Molinari et al. 2000)
Photocatalytic membrane and NTR7410 membrane	Type I and II	Medium pressure Hg lamp	Degussa P25 TiO_2	Demineralization of Congo red and Patent blue	Slurry PMR was more efficiently degraded the pollutants than in entrapped PMR	(Molinari et al. 2005)
Commercial Polymer membranes (10)	Type I	20 W NECUV-A lamps	TiO_2	Membrane stability investigation	PTFE, PAN and PVDF membranes showed better stability Limitation: TiO_2 cake formation on membrane	(Chin et al. 2006)
Ceramic filter tube	Type II	UVA black light cathode lamp	Degussa P25 TiO_2	Acid red 4	Degradation is more in a dead-end system than in cross-flow system. Degradation increases with an increase in catalyst loading.	(Wang et al. 2008)
Hollow fibre membrane module	Type I	8W UV lamp	TiO_2	Degradation of Acid red 1	Higher efficiency of AR1 degradation. Back flushing is required to remove the fouling.	(Kertèsz et al. 2014)
PVDF flat sheet membrane	Type I	4 W UVC lamp	Degussa P25 TiO_2	Removal of virus bacteriophage f2	99.99% virus inactivation, backflushing required	(Zheng et al. 2015)

Cellulose acetate membrane	Type II	UV lamp	TiO_2 nanosheet/GO	Demineralization of Congored dye	Complete removal of dye, Fouling	(Nair and Jagadeesh 2017)
Cellulose acetate membrane	Type II	Sunlight	Ag/ TiO_2 nanosheet	Demineralization of Congored dye	Complete removal of dye in three passess	(Nair and JagadeeshBabu 2017)
Ceramic membrane	Type II	UV lamp	TiO_2	Removal of Humic acid	98.56% rejection. Better permeation and rejection rate and photostability	(Alias et al. 2018)
Ceramic microfiltration membrane	Type I and II	6W UVA lamp	TiO_2 P25	Removal of Oxytetracycline	Removal efficiency increased with slurry dosage and permeate flux decline was decreased during immobilization	(Espíndola et al. 2019)
MF Ceramic membrane	Type I and II	Visible light	N doped TiO_2	Removal of Diclofenac	Suspended PMR showed better removal ability. PMR with immobilized showed lesser fouling.	(Nguyen et al. 2020)
Polyacrylonitrile based hollow titanium dioxide nanofibers	Type I	30 W UV lamp	TiO_2	Removal of Bisphenol A	97.3% removal of Bisphenol A.	(Mohammad Jafri et al. 2020)
Mexican natural zeolite membrane	Type I	2.2 W lamp	$FeCl_3$	Removal of RB5 dye	92.3% degradation of RB5 dye	(Domenzain-Gonzalez et al. 2021)
PVDF hollow fiber membrane	Type I	UVA lamp	TiO_2	Removal of nitrate	60.3% removal in the presence of formic acid	(Petsi et al. 2021)

From the literature, we can conclude that the PMRs were mostly utilized TiO_2 catalyst, cellulose acetate/ceramic membranes and UV light for irradiation and degradation of organic pollutants. From the table, it has been revealed that there is a scope for visible light irradiated polymer membrane based PMRs for the degradation of inorganic pollutants. Yahui Shi et al has discussed about the requirement of visible light driven photocatalytic

membranes in water purification process, since the PMs has different intrinsic drawbacks (Shi et al. 2019a) such as,

1) PMs require additional customization

2) Membrane material suffers damage from irradiation and overoxidation

3) The restricted processing capacity

4) Low effective surface area of photocatalysts leads to lesser efficiency of PMs

5) Less life span of PMs due to catalyst deactivation

Amidst all disadvantages, the PMs can be modified with visible light active nanoparticles to prepare composite or hierarchical membranes.

A hierarchical membrane with surface coated nanoparticle on it is an alternative way for a multifunctional membrane (Bai et al. 2010). TiO_2 based materials have gained great absorption ability of Cr(VI) from the polluted water. Bai et al. reported a novel TiO_2 nanothorn coated multifunctional membrane was produced with enhanced water flux and reduced membrane fouling property (Bai et al. 2010). Various TiO_2 structures such as nanoparticles, nanowires, nanofibers, nano-thorns and microspheres have been considered as nanomaterials for the synthesis of hierarchical membranes (Bai et al. 2010; Nair and Jagadeesh 2017).

Nair et al. prepared TiO_2-graphene oxide nanosheet coated hierarchical membranes for the simultaneous photodegradation and filtration of Congo red dye under photocatalytic irradiation and the major drawback reported by them is the weakening of catalyst activity due to the fouling of membrane which is due to dye adsorption on the membrane (Nair and Jagadeesh 2017). In literature, various TiO_2 structures such as nanoparticles, nanowires, nanofibers, nano-thorns, and microspheres have been considered as compatible materials for the fabrication of hierarchical membranes (Bai et al. 2010; Nair and Jagadeesh 2017). Dzinun et al. reported immobilization of hybrid TiO_2/clinoptilolite (TCP) photocatalyst at the outer layer of the double-layer hollow fiber (DLHF) PVDF membranes. The TiO_2/CP photocatalysts were synthesized by the solid-state dispersion method. TiO_2 (10 wt%)/CP (90 wt%) could yield 95% demineralization of Reactive Black 5 (RB5) in the photocatalytic membrane reactor under UV illumination (Dzinun et al. 2019).

2.9 SCOPE AND OBJECTIVES OF THE STUDY

Over the past few decades, several methods have been employed for the removal of heavy metals from the wastewater. The commonly used procedures for removing the heavy metals from the contaminated water are chemical precipitation, ultra-filtration, ion exchange, reverse osmosis, electrowinning, carbon adsorption and phytoremediation. These methods have limitations like the formation of large amounts of sludge containing toxic compound, high cost, partial removal of specific ions, fouling due to sludge, and long time for the removal of metals. Thus, there is a need for new a technology to remove metal ions from wastewater, which could be filtration combined with degradation. There is literature on combining photocatalytic degradation and membrane separation in a single unit called photocatalytic membrane reactor. In this photocatalytic membrane reactor, TiO_2 can be used as a potential catalyst in the degradation of pollutants. In literature, pure TiO_2 is widely used in photocatalytic degradation of the pollutant dyes, but it has a limitation like agglomeration, electron-hole recombination, and separation of the secondary pollutant, separation of catalyst and negligible visible light absorption capacity. Similarly, pure membrane filtration has many disadvantages like membrane fouling, high cost, less reusability, reduction in flux and sensitive operating conditions (higher pressure). By using modified TiO_2 catalyst in the synthesis of the hierarchical membrane, the disadvantages mentioned above can be eliminated.

Based on the literature survey it has been found that, the nanoparticle incorporation in the membrane will enhance the membrane performance by reducing hydrophobicity. Addition of TiO_2 based nanoparticles and nanosheets in polymer nanofiltration membrane has not been reported. The conducting polymer Polyaniline (PANI) can be doped to enhance the visible range absorptivity of TiO_2 nanoparticle. PANI improves TiO_2 dispersion, prevents particle agglomeration and electron-hole recombination. Hierarchical membrane made out of conducting polymers can further help in improving the performance of the membrane. Hierarchical membranes with catalyst coated on the membrane can improve exposed catalyst area. There is no literature on the hierarchical membrane, particularly in the removal of heavy metals. The following objectives are formulated to carry out the suggested research effort in order to satisfy the requirement described above and to close the literature gap.

2.10 OBJECTIVES

1. **To synthesize TiO$_2$ based mixed oxide catalysts (TiO$_2$-WO$_3$ and TiO$_2$-SnO$_2$ through the hydrothermal method).**

a) To optimize the operating variables

b) To characterize the mixed oxide catalyst using TEM, FTIR, XRD, and BET

c) To analyse the performance of mixed oxide catalyst (Chromium (VI) degradation studies under visible light)

2. **Synthesis, characterization and performance analysis of pristine PANI membranes.**

a) To study the effect of operating variable on Chromium (VI) reduction (catalyst loading, initial concentration of Cr(VI) solution, and pH).

b) To characterize the prepared membrane using SEM, FTIR, and contact angle.

c) To analyse the performance of pristine PANI membrane (flux, water uptake, fouling, and the degradation studies under visible light).

3. **Synthesis, characterization and performance evaluation of composite membranes.**

a) To study the effect of operating variable on Chromium (VI) reduction (catalyst loading, initial concentration of Cr(VI) solution, pH).

b) To characterize the prepared membranes using SEM, FTIR, contact angle.

c) To analyse the performance of composite membrane (flux, water uptake, fouling, and degradation studies under visible light).

4. **Synthesis, characterization and performance analysis of hierarchical membranes**

a) To study the effect of operating variable on Chromium (VI) reduction (catalyst loading, initial concentration of Cr(VI) solution, and pH).

b) To characterize the prepared membranes using SEM, FTIR, and contact angle.

c) To analyse the performance of hierarchical membrane (flux, water uptake, fouling, and degradation studies under visible light).

CHAPTER 3

PHOTOCATALYTIC DEGRADATION OF CHROMIUM (VI) USING TIO$_2$-WO$_3$ COUPLED SEMICONDUCTOR OXIDE NANOPARTICLES

3.1 INTRODUCTION

In the recent past, coupled semiconductors are used for the photocatalytic reduction of Cr (VI) to Cr(III) under visible light. The coupling can be achieved using many methods like physical mixing of metal oxides, multistep grafting, sol-gel method, co-precipitation method, impregnation, hydrothermal methods, ball milling, and flame spray technique. The narrow energy bandgap of WO$_3$ will help in reducing the bandgap of coupled products, and thereby reducing the rapid electron-hole pair recombination. Moreover, the WO$_3$ coupling widens the spectral response range of nanocatalyst species. Coupling of WO$_3$ with TiO$_2$ can enhance the photocatalytic ability of the compound and can serve as electron-accepting species in the TiO$_2$-WO$_3$ complex.

In the current work, TiO$_2$-WO$_3$ visible light photocatalysts (direct Z-scheme for the catalyst is given in Figure 3.1) were used in the reduction of highly toxic hexavalent Chromium ions to less toxic trivalent Chromium (III). Reduction is possible in the conduction band (CB) of TiO$_2$ at lower pH, and because the reduction potential of Cr(VI)/Cr(III) involves the transfer of 3 electrons. Hence, the TiO$_2$-WO$_3$ catalyst helps in increasing the overall reaction rate. However, overloading of WO$_3$ will decrease the photocatalytic ability of the composite.
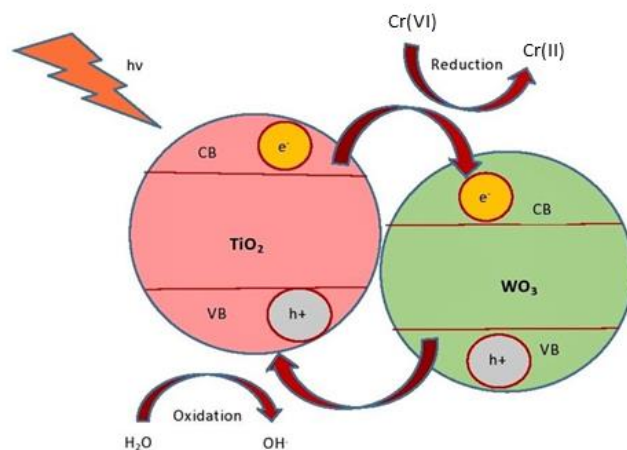
Figure 3.1 Direct Z-scheme of TiO$_2$-WO$_3$ catalyst

The direct Z-scheme of TiO$_2$-WO$_3$ catalyst is shown here in figure 3.1. On photocreated charge excitation in the presence of visible light, the electrons in the photocatalyst move one with a higher CB position. In the meantime, holes in the two photocatalysts follow a reverse migration. The CB of TiO$_2$ is above the CB of WO$_3$, and the electron transfer occurs from TiO$_2$ CB to the WO$_3$ CB, and thus the reduction of Cr(VI) to Cr(III) occurs on the catalytic surface. The oxidation of water occurs in the VB of WO$_3$. This process promotes spatial separation and suppressed recombination of charge carriers.

WO$_3$ is an n-type semiconductor with a narrow bandgap (2.6-2.8 eV) as compared to TiO$_2$. It helps as a charge carrier in heterogeneous photocatalysis. WO$_3$ is a promising material and used in different applications such as photoreduction of Cr(VI), gas sensing, LEDs, and the degradation of textile dyes and pharmaceutical waste.

3 mg/L Cr(VI) was totally photoreduced using heterogeneous catalyst MgCr$_2$O$_4$/WO$_3$ within 120 min at pH 4 under sunlight. The WO$_3$ helped in charge separation of electron-hole pairs and avoided photocorrosion (Ben et al. 2022). Lewen et al. utilutilized spatial gasochromic properties to develop a hydrogen gas sensor (Nie et al. 2022). Insaaf et al. used hydrothermally prepared WO$_3$ nanostructures for the photocatalytic degradation of phenol. The WO$_3$ was synthesized within a short span of 4 hours and showed excellent efficiency of 98 % degradation of phenol. The WO$_3$ nanostructures showed better optical properties and they have been used in blue LEDs (Assadullah et al. 2022). Jirayus et al. used sunlight-responsive WO$_3$/AgBr heterojunction photocatalyst for the degradation of Rhodamine B dye and ofloxacin antibiotic under solar energy (Piriyanon et al. 2021). The hydrothermal route of synthesis of TiO$_2$-WO$_3$ can ensure an efficient coupling between two

metal oxide semiconductors, thus it can exploit the electron storage capability of WO_3 for the reduction reaction.

3.2 MATERIALS

The materials used in this section include titanium (VI) isopropoxide (97%) from Sigma Aldrich, sodium tungstate dihydrate ($Na_2WO_4.2H_2O$) (Emplura), and acetic acid glacial (99-100%) from Emplura, India. Ethanol (99%) and Potassium dichromate were procured from Fischer, WO_3 was purchased from Sigma Aldrich. Distilled water was used for all the experiments. All the chemicals were used without any purification.

3.3 METHODS

3.3.1 Preparation of Nanocatalyst

TiO_2-WO_3 photocatalyst was prepared hydrothermally at different Ti: W ratios (1:1, 10:1, 20:1, 30:1 and 40:1). For preparing a 1:1 catalyst, 2 ml of titanium isopropoxide was dissolved in 20 ml of ethanol under stirring. 1.5 ml of acetic acid and 5 ml of distilled water were added to the reaction mixture and stirred for 10 min. Then, 2.214 g of sodium tungstate dihydrate was dissolved under constant stirring almost for 1 hour, and the reaction mixture was transferred into a Teflon-lined autoclave. The autoclave was heated at an elevated temperature of 160°C for 24 hours. After the reaction, the product was centrifuged and washed several times with deionized water and with ethanol. The obtained solid product was dried in an oven at 60°C overnight. The dried nanoparticles were ground using a mortar pestle and stored for further use. The prepared photocatalysts were designated as T1W1, T10W1, T20W1, T30W1 and T40W1 based on the Ti:W ratios used.

3.3.2 Characterization of catalysts

Transmission electron microscopy (TEM) was used to analyse the morphology of the prepared catalysts. The X-ray diffraction pattern was recorded using JEOL DX-GE-2P Goniometer operated at 25°C. Brunauer-Emmett-Teller (BET) analysis and Barrett-Joyner-Halenda (BJH) analysis were conducted in Quantachrome Nova instrument to calculate the available surface area, pore volume, and pore diameter of the prepared catalysts. Optical properties of the catalyst were studied using UV-Visible spectroscopy (U-2900 Hitachi). Attenuated total reflectance Fourier transform infrared (ATR-FTIR) spectra were obtained

to study the functional groups in the prepared catalyst. Commercially available TiO_2 and WO_3 were taken as a reference to compare the characteristics of the prepared catalyst.

3.3.3 Photocatalytic reduction of Chromium (VI)
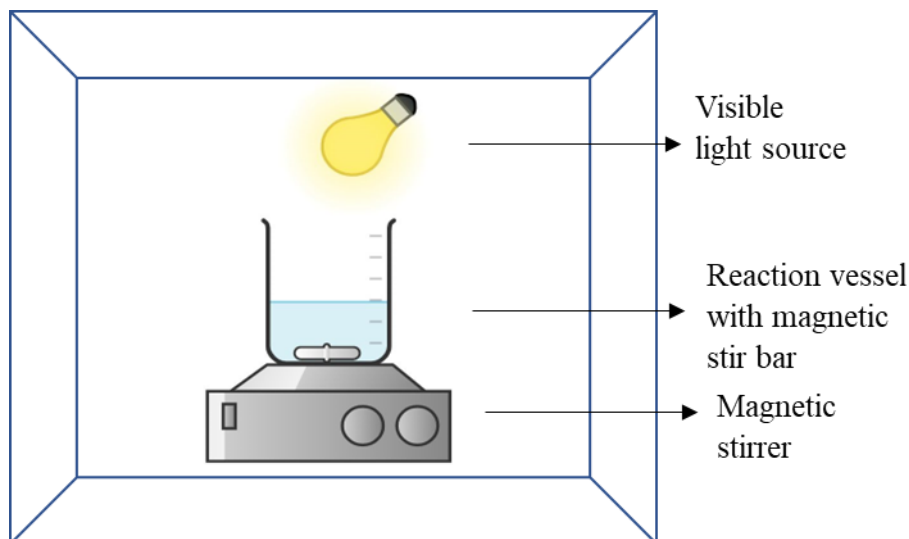
Figure 3.2 Pictorial representation of the batch photocatalytic reactor

The performance study of TiO_2-WO_3 photocatalysts was carried out in a batch photoreactor of 100 ml volume and the reaction was irradiated using 400 W metal halide lamp (in Figure 3.2). Chromium solution was prepared by dissolving 2.828 g of potassium dichromate in 1000 ml of deionised water (Djellabi et al. 2016). The pH of the solution was adjusted by using 1 M H_2SO_4 and pH was frequently monitored using a pH meter. The performance of all the prepared catalysts, prepared with different molar ratios ranging from 1:1 to 40:1 was analyzed and compared. The pH (1 to 6), catalyst loading (0.1–0.6 g/L), and initial concentration of Chromium (10-40 ppm) were optimized by using the OVAT method. The reaction mixture was exposed to visible light under constant stirring for 5 hours in a beaker with 100 ml reaction volume as shown in Fig. 3.2. At a constant interval of time, 2 ml sample was collected from the reaction mixture and subjected to various analysis like UV-Visible spectroscopy and inductively coupled plasma optical emission spectroscopy (ICP-OES).

The reduction of hexavalent Chromium in the reduced solvent was calculated using the following equation,

Percentage Chromium (VI) remaining (%) = $[C/C_o]*100$ $\rightarrow$ (1.0)

Where C is the final concentration of Chromium (VI) solution (ppm) and C_o is the initial concentration of Chromium solution (ppm) at a measured time after reduction.

3.3.4 Box Behnken method of statistical analysis

Response Surface Methodology (RSM) was employed to optimize the photocatalytic Chromium (VI) reduction. Generally, RSM helps to develop an approximate model closest to an actual regression model. Box–Behnken method of statistical analysis and the response surface methodology was employed to probe the three independent variables. The independent variables selected in this study are the pH of the solution, initial concentrations of the chromate solution, and catalyst loading. The low, centre and high levels of each variable are assigned as -1, 0, and +1 respectively. The upper and lower values of each variable were decided through the preliminary experiments. The resultant response function used in the study is percentage Chromium degradation. A total of 18 experimental runs were employed to evaluate the current model. RSM model has been created and analysed using Design-Expert 11, (Stat-Ease, Inc., Minneapolis, MN) software.

3.4 RESULT AND DISCUSSION

3.4.1 Surface morphology of the catalyst

Morphology of the synthesised TiO_2-WO_3 photocatalysts was analysed using JEOL JEM-2100 TEM. The catalyst prepared using different Ti:W molar ratio was observed under TEM. The TEM images (Figure 3.3) shows that the prepared catalyst is in different size and in agglomerated hexagonal shape (Figure 3.3.(f)). It was also observed that TiO_2-WO_3 grows more uniformly than pure TiO_2 catalyst (Liu et al. 2014). The average particle size obtained from TEM results for different catalyst were T1W1 - 21.1 nm, T10W1 - 20.048 nm, T20W1 - 16.93 nm, T30W1 - 20.06 nm and T40W1 - 12.61 nm and pure TiO_2 size - 21 nm. The average size of T40W1 (40:1) was the lowest among the other catalysts. It is revealed that, WO_3 content causes reduction in the size of the nanoparticles as reported in the literature (Mugunthan et al. 2018a);(Liu et al. 2014). The hexagonal shaped edges are diffused in solution and offers better photocatalytic activity.
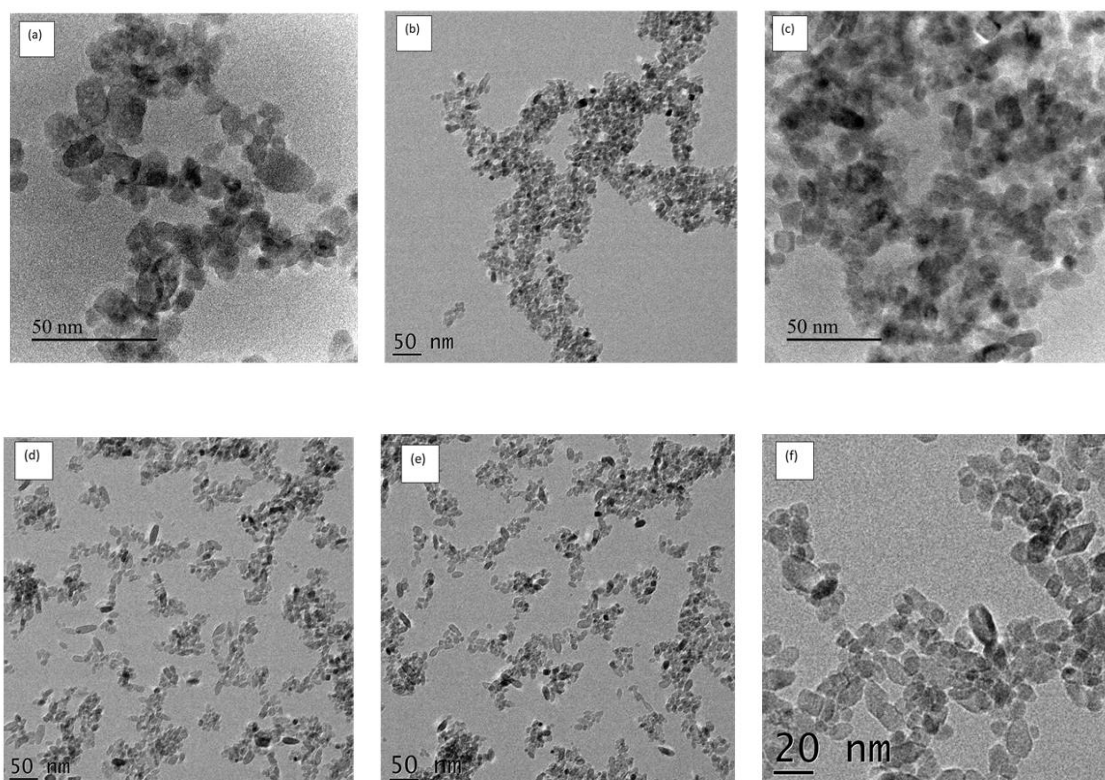
Figure 3.3 (a) TEM images of T1W1, (b) T10W1, (c) T20W1, (d) T30W1, (e) T40W1 and (f) T40W1at 20 nm resolution obtained for T40W1 catalyst respectively.

3.4.2 X-ray diffraction pattern for Photocatalysis
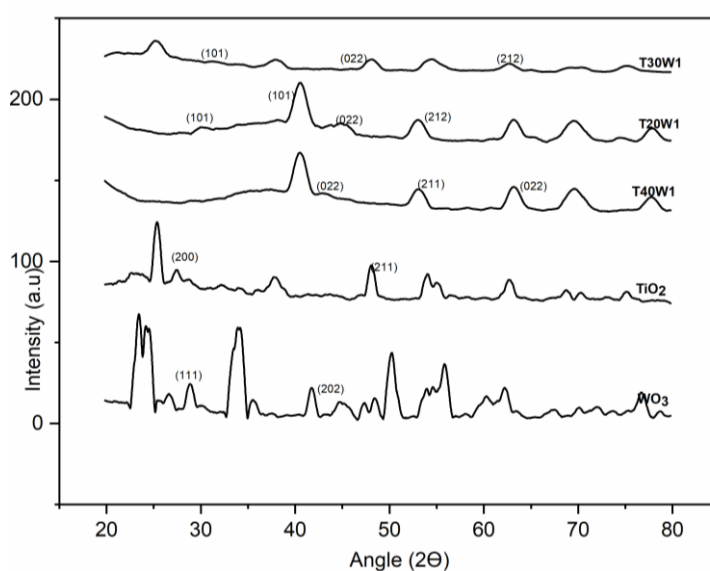
Figure 3.4 X-ray diffraction pattern for photocatalysts.

The XRD pattern of the prepared catalysts were shown in Figure 3.4 The catalysts prepared were in crystalline nature, in which TiO_2 anatase peak and W monoclinic peak were

48

observed. The peak at 2Θ =25.672° and 37.881°corresponds to (101) planes of anatase phase of TiO_2, and the peaks at 48.41°, 55.707° and 54.278° corresponding to (200), (211) and (105) plane of anatase phase of TiO_2 (Crystallography open database: 00-002-0406).

The peaks obtained at 2Θ=25.65°, 38.912 ° and 49.684 ° correspond to (111), (022) and (202), crystalline phase of monoclinic $WO_3.H_2O$ (Crystallography open database: 01-084-08086). The catalysts T40W1 and T20W1 were shown more prominent peaks similar to pure TiO_2.

3.4.3 FTIR Analysis for photocatalyst
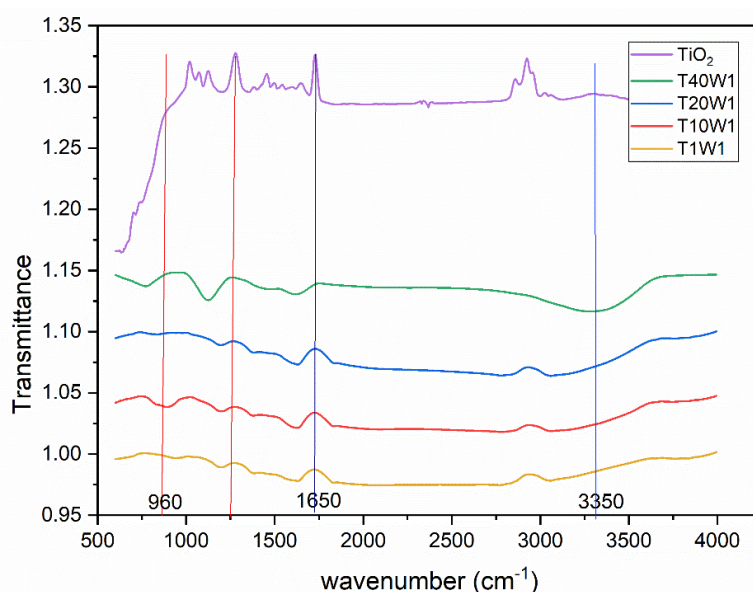
Figure 3.5 ATR-FTIR spectra for prepared photocatalysts

The ATR-FTIR spectra of photocatalysts of different molar ratios are shown in the Figure 3.5. The peak at 960 cm^{-1} corresponds to the Ti-O bond stretching of Ti-O-Ti bonds. A peak at 1650 cm^{-1}, and peaks in the range between 2945-3051 cm^{-1} attribute to the surface hydroxyl groups caused by the adsorbed water in the sample. The peak at 1650 cm^{-1} represents the bending vibrations of OH$^-$ group. The peaks at to 631 cm^{-1} (in T40W1) corresponds to W-O-W bond, and similarly the peak attributed to 814, 1631-1634, 2356 cm^{-1} (in T20W1) are corresponds to ν(W-OW), ν(W$_3$O$_9$), O-H/ H-O-H, O-H and 3307 cm^{-1} (T40W1) associated with W-OH, H_2O respectively as reported by J. Díaz-Reyes et al. (Díaz-Reyes and Balderas-López 2008). In TiO_2-WO_3 catalysts, the change in intensity of the peak observed at 1630 cm^{-1} and 3350 cm^{-1} attributed to -OH vibrations. The absorption

peaks associated with the surface water and hydroxyl groups are especially stronger in the T40W1 hybrid nanoparticles, which indicates that TiO_2-WO_3 has a better photocatalytic activity and hydrophilicity (Boga et al. 2018; Hu et al. 2018a).

3.4.4 BET Analysis

Table 3.1 BET and BJH analysis data for TiO_2-WO_3 catalyst

Catalyst	Pore volume (cc/g)	Pore diameter (nm)	Surface area (m^2/g)
T1W1	0.086	5.436	35.673
T10W1	0.157	3.473	60.047
T20W1	0.152	1.74	71.660
T30W1	0.165	3.318	152.064
T40W1	0.215	5.994	173.157
TiO_2	0.214	2.819	45.551

The surface area, pore diameter, and pore volume of the prepared catalyst were analysed and tabulated in Table 3.1. The catalysts prepared with a molar ratio of 40:1 and 30:1 of Ti: W showed a higher surface area among all the prepared catalysts. The addition of WO_3 leads to improved surface area and active sites, and making TiO_2-WO_3 a high photoactive catalyst. The reason for high surface area might be due to the cavitation bubbles formed during the synthesis (Anandan et al. 2014). T1W1 has the lowest surface area (35.673 m^2/g), among other catalysts. It might be due to the higher concentration of WO_3, which has resulted in low dispersion of WO_3 in TiO_2; and excess amount of WO_3 could act as a recombination centre for charge carriers. The Barrett–Joyner–Halenda (BJH) analysis report shows the mesoporous structure formation in the range of 2-20 nm, as stated by Dozzi et al. (Dozzi et al. 2016).

3.4.5 Bandgap calculation

The photoabsorption studies were carried out using prepared TiO_2-WO_3 catalysts with UV-visible spectroscopy. The optical energy bandgap of the catalyst was calculated from the Tauc expression (Ohta et al. 2018). The bandgap obtained for catalyst of different molar ratios are 3.1 eV, 3.2 eV, 2.97 eV, 2.94 eV and 2.9 eV for 10:1,1:1 ,20:1,30:1 and 40:1 respectively. T1W1 catalyst showed a higher energy bandgap among all the prepared catalysts. As the WO_3 loading increases, bandgap value decreased to 2.9 eV (in Figure 3.6).

All TiO$_2$-WO$_3$ catalyst had a longer wavelength in the range 380-750 nm, which fall in the visible light region. TiO$_2$-WO$_3$ catalyst can attract a longer section of the solar spectrum, and the recombination of electron-hole pairs can be reduced with its lower Fermi energy level. Similar observations were reported in the literature (Mugunthan et al. 2018a),(Anandan et al. 2014).
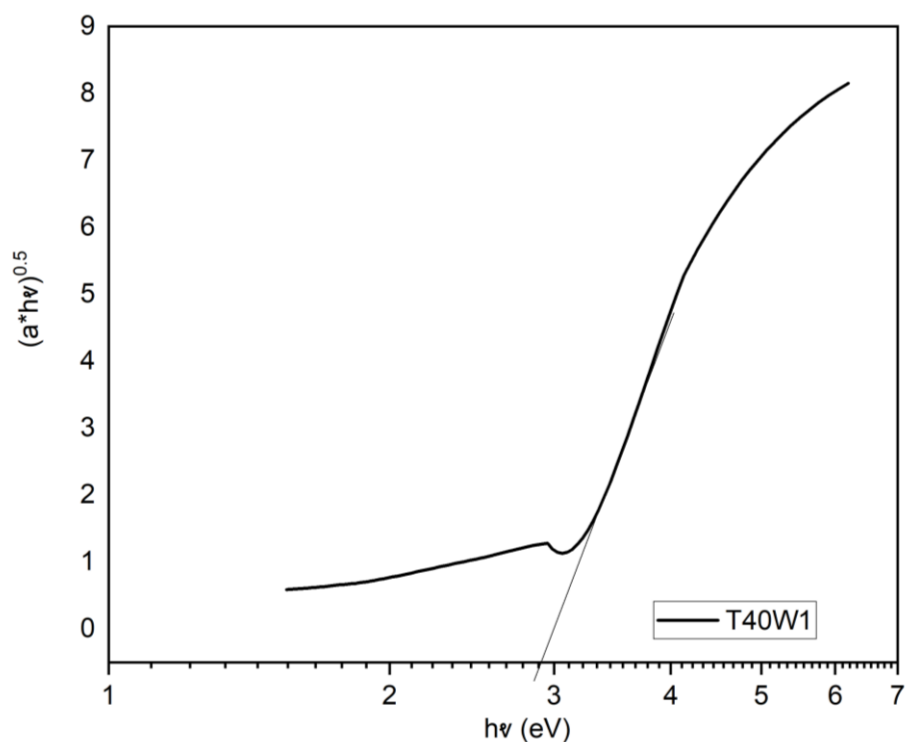
Figure 3.6 Bandgap diagram for TiO$_2$-WO$_3$ (40:1) catalyst.

3.5 PHOTOCATALYTIC REDUCTION OF CHROMIUM (VI)

The catalytic potential of the prepared TiO$_2$-WO$_3$ catalyst for reducing potassium dichromate solution i.e., from hexavalent Chromium to trivalent Chromium under various operating conditions like different pH, initial Chromium concentration and catalyst dosage were analysed. The accumulated photo-induced electrons from the WO$_3$ domains will be transferred to H$^+$ ions in the solution, whereas the holes remain in the VB edge of TiO$_2$. H$^+$ species attacks the Chromium (VI) ions and reduces it to Cr(III) using three electrons (in equation 2.0 and 3.0). H$_2$O accepts the holes in the absence of any reducing agents (Liu et al. 2014). In basic pH, Cr(VI) ions can be precipitated to Cr(OH)$_3$ form of Cr(III) (shown in equation 4.0) . The functional groups containing -O- on the surface can absorb Cr(III) on the catalyst (Xu et al. 2018). The coupling of metal oxide semiconductors can provide

excess -O- groups. The photocatalytic reduction under visible light in acidic medium and basic pH (Marinho et al. 2017) can be written as,

For acidic medium,

$$H_2CrO_4 + 6H^+ + 3e^- \quad \rightarrow \quad Cr^{3+} + 4H_2O \qquad \qquad \rightarrow (2.0)$$

$$HCrO_4^- + 7H^+ + 3e^- \quad \rightarrow \quad Cr^{3+} + 4H_2O \qquad \qquad \rightarrow (3.0)$$

For basic medium,

$$CrO_4^{2-} + 4H_2O + 3e^- \quad \rightarrow \quad Cr(OH)_3 + 5OH^- \qquad \qquad \rightarrow (4.0)$$
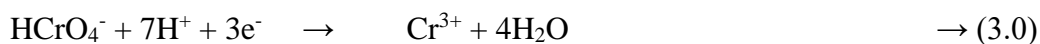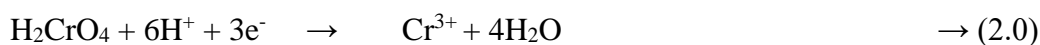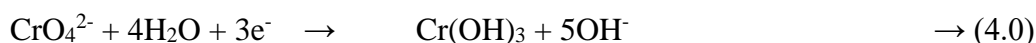
3.5.1 Photocatalytic reduction and effect of molar ratios of catalyst
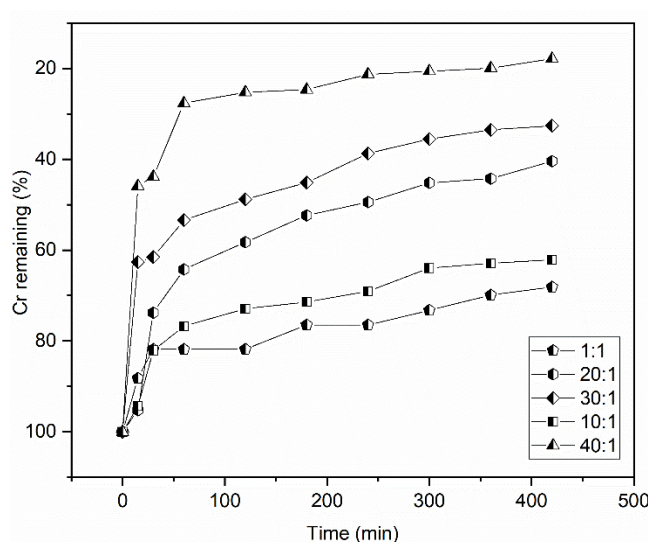
Figure 3.7 Chromium (VI) removal studies using TiO_2-WO_3 catalyst (at a catalyst loading of 0.6 g/L, 100 mL Cr(VI) of 30 ppm initial concentration and a pH of 4.20).

The reactions were carried out according to the method described in section (3.3.3). From the Figure 3.7, it was observed that the catalyst prepared with a molar ratio of 40:1 has shown higher photocatalytic activity among the other catalyst molar ratios. The photoactivity of the catalyst is observed to be in the decreasing trend of tungsten content. This can be due to the higher concentration of tungsten content, which might have inhibited the reaction (Dozzi et al. 2016; Mugunthan et al. 2018a). The efficiency of the catalyst increased as the WO_3 content decreased in it. The overloading of WO_3 content might have created structural defects in the anatase TiO_2, which might have played as electron-hole recombination centres. Among the prepared catalyst, the catalyst with molar ratio T1W1

showed lesser photocatalytic activity, and the lesser surface area which has hindered the efficiency. Moreover, the higher concentration of WO_3 in T1W1 also reduces photocatalytic activity (Dozzi et al. 2016). T40W1 catalyst was used in the remaining experiment to obtain maximum hexavalent Chromium reduction.

3.5.2 The effect of concentration on Chromium removal

The effect of initial concentration on Chromium removal was illustrated in Figure 3.8 (at 120th min). The removal studies were carried out in a batch reactor with a reaction volume of 100 ml under normal room temperature. Chromium solutions of 5 ppm, 10 ppm, 15 ppm, 20 ppm, and 30 ppm were prepared, and the reaction was carried out with a catalyst loading of 0.6 g/L, and the solution pH was kept constant. The reaction mixture containing Chromium solutions and catalyst were kept under dark conditions for 30 min to stabilize the catalyst. Then, the reactor was exposed to a 400 W halogen visible light source and continued the reaction for 120 min. 2 ml samples were collected at every 15 min for an initial period of one hour and then for every 30 min. The collected samples were then analyzed in a UV-visible spectrophotometer at a wavelength of 350 nm (Sanchez-Hachair and Hofmann 2018). Initial Cr(VI) concentration of 5 ppm solution, undergone complete reduction within 15 min under visible light irradiation. When the reaction was conducted at an initial concentration of 10 ppm, the percentage removal almost tended to zero at 120 min. As the concentration increased, the rate of Cr(VI) reduction decreased, as shown in the Figure 3.8. For further analysis, the initial concentration of 10 ppm Chromium solution was used.
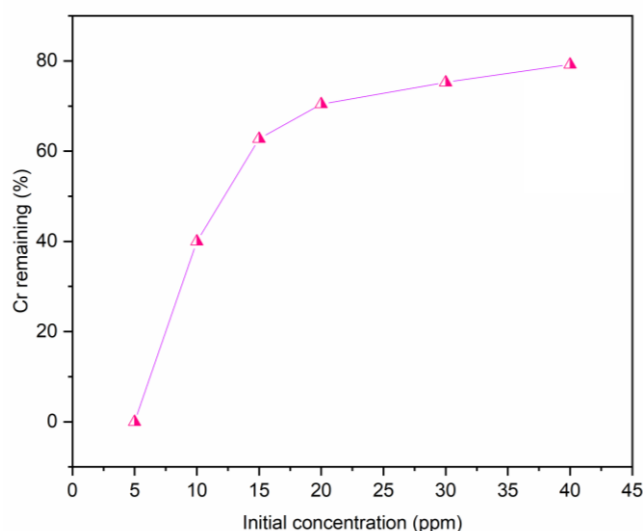
Figure 3.8 The effect of initial concentration on Chromium (VI) removal.

53

3.5.3 The effect of catalyst loading on Chromium removal

The effect of catalyst loading on Chromium removal is shown in Figure 3.9. The removal study was performed under visible light using 10 ppm solution at a constant pH with varying catalyst loading from 0.1 g/L to 0.6 g/L. It was observed that the removal efficiency increased up to a catalyst dosage of 0.4 g/L, and then decreased and remained stable. It can be due to the light scattering and screening effects caused by the excess amount of suspended catalyst in the Chromium solution (Mugunthan et al. 2018a).
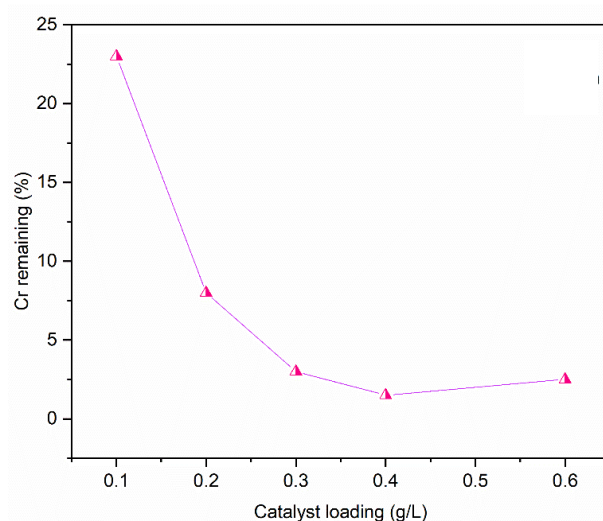
Figure 3.9 The effect of catalyst loading on Chromium (VI) removal.

3.5.4 The effect of pH on Chromium removal

The removal of inorganic pollutants like Chromium is highly pH-dependent. Researchers have revealed that the removal of Chromium increases with a decrease in pH (Joshi and Shrivastava 2011). T40W1 was used to carry out the reduction reaction to investigate the effect of pH on Chromium (VI) removal via photocatalysis under visible light, which is represented in Figure 3.10. The removal study was carried out by varying the solution pH from 1 to 6, at an initial concentration of 10 ppm, and a catalyst loading of 0.4 g/L. The reaction was allowed to perform under dark for 30 min ahead of photocatalysis reaction. During pre-adsorption time, the pH remained the same. In the presence of light, the pH started to decrease during the initial 120 min, but for higher initial pH, the solution pH reduces for an initial period of 120 min and then increases. At lower pH (pH 2.0), the adjusted pH decreases to pH 1.53, and for pH 5.0, the pH initially fell and increased to a pH 6.0, which can be due to the oxidation reaction occurring at higher pH. Increased

amount of OH⁻ species in the reaction medium under necessary conditions can contribute towards the oxidation of reduced Chromium (III) back to Chromium (VI).
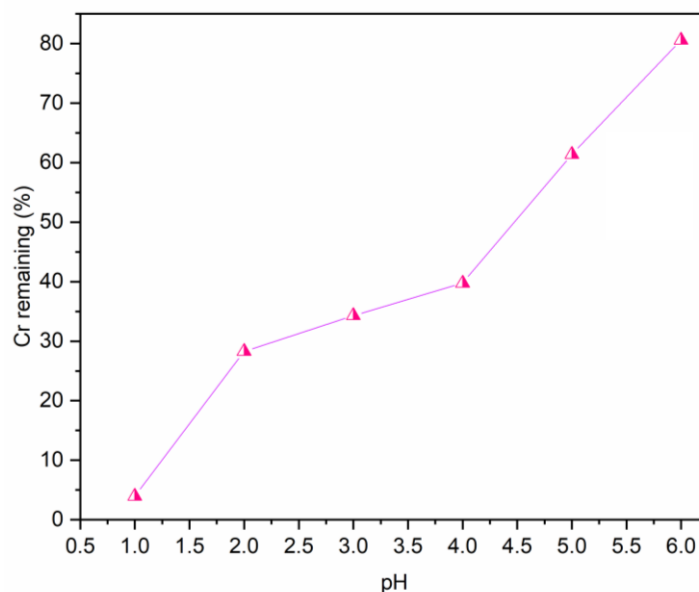
Figure 3.10 The effect of pH on Chromium (VI) removal.

3.6 RESPONSE SURFACE METHODOLOGY

For formulating the RSM model, the Box-Behnken design is used in this study. The solution pH, initial concentration of the Chromium solution, and catalyst dosage were selected as design parameters. The coded values and independent variables are listed in Table 3.2 and the experimental data for Chromium removal in Box Behnken Method is tabulated in Table 3.3.

Table 3.2 The coded values and independent variables taken for optimization

Independent variables	Symbol	Levels		
		-1	0	+1
pH	A	1	2	3
Concentration (ppm)	B	10	20	30
Catalyst loading (g/L)	C	0.2	0.4	0.6

Table 3.3 Experimental data for Chromium removal in Box Behnken Method.

Stand ard	S. no	Factor 1 A: pH	Factor 2 B: Concentratio n (ppm)	Factor 3 C: Catalyst loading (g/L)	Response Degradatio n (%) (Actual)	Response Degradation (%) (Predicted)
10	1	2	30	0.2	46.38	46.33
2	2	2	10	0.6	79.54	79.59
13	3	3	10	0.4	44.91	44.98
5	4	2	30	0.6	49.86	49.79
6	5	2	10	0.2	47.48	47.54
14	6	1	20	0.6	95.99	95.94
12	7	2	20	0.4	71.23	71.35
8	8	2	20	0.4	70.73	71.35
4	9	3	30	0.4	26.58	26.76
15	10	3	20	0.2	25.32	25.18
2	11	2	20	0.4	71.75	71.35
18	12	2	20	0.4	70.97	71.35
7	13	3	20	0.6	56.91	56.78
10	14	1	10	0.4	96.91	96.24
9	15	2	20	0.4	71.37	71.35
1	16	2	20	0.4	72.06	71.35
3	17	1	20	0.2	92.71	92.83
17	18	1	30	0.4	83.35	83.27

Table 3.4 Analysis of variance (ANOVA) associated response surface quadratic model for decomposition of Chromium.

Source	Sum of squares	df	Mean square	F-value	p-value	Column 1
Model	7940.80	9	882.31	2076.97	< 0.0001	significant
A-pH	5794.80	1	5794.80	13641.01	< 0.0001	
B-Concentration	501.49	1	501.49	1180.52	< 0.0001	
C-Catalyst Loading	609.18	1	609.18	1434.01	< 0.0001	
AB	7.40	1	7.40	17.42	0.0031	
AC	191.96	1	191.96	451.88	< 0.0001	
BC	204.20	1	204.20	480.70	< 0.0001	
A²	13.26	1	13.26	31.20	0.0005	
B²	465.15	1	465.15	1094.97	< 0.0001	
C²	118.54	1	118.54	279.05	< 0.0001	
Residual	3.40	8	0.4248			
Lack of Fit	2.19	3	0.7303	3.02	0.1323	not significant
Pure Error	1.21	5	0.2415			
Cor. Total	7944.20	17				

The lack of fit F-value of 3.02 (in Table 3.4) is not significant as the p-value is >0.05. The non-significance lack-of-fit showed that the model was valid for the work (Mourabet et al. 2017).

The relation between the independent variables and the response can be given as y = f $(X_1, X_2, X_3 \ldots X_k)$, where y is the response function and X_1, X_2 etc. are the independent variables. The RSM quadratic model obey the general equation,

$$Y = \beta_0 + \sum \beta_i X_i + \sum \beta_{ii} X_i^2 + \sum \sum \beta_{ij} X_i X_j \qquad \rightarrow (5.0)$$

Where β_0 is a constant, β_i, β_{ii} and β_{ij} are the linear regression coefficient, quadratic and cross-product coefficients, respectively.

A quadratic equation (given in equation 6.0) to predict the percentage degradation in terms of an independent variable obtained through the statistical analysis as follows,

Cr(VI) Degradation (%)

$$= +62.07 - 45.02 \, \text{pH} + 5.03 \, \text{Concentration}$$
$$+ 150.04 \, \text{Catalyst Loading} - 0.13 \, \text{pH} * \text{Concentration} + 34.63 \, \text{pH}$$
$$* \text{Catalyst Loading} - 3.57 \, (\text{Concentration} * \text{Catalyst Loading})$$
$$+ 1.742 \, \text{pH}^2 - 0.10 \, \text{Concentration}^2 - 130.3 \, [\text{Catalyst Loading}^2]$$
$$\rightarrow (6.0)$$

A positive value for the coefficient represents an outcome favouring the optimization, and a negative value suggests an inverse correlation between the component and the response. The coefficient of determination (R^2) of the model is 0.9996, which specifies a good fit between predicted values and the experimental datum. The R^2 value conveys that the independent variables explain 95.5 % of the variations for percent Chromium (VI) degradation, and this means that the model does not talk about 4.5 % of the difference. Predicted R^2 explains how well the model foresees a response value. The adjusted R^2 and predicted R^2 should be within 0.20 of each other to be in rational concurrence. In this respect, the predicted R^2 of 0.9954 is in reasonable consent with the adjusted R^2 of 0.9991. Adequate precision estimates the signal to noise ratio and differentiates the range of the predicted values at the design points to the average prediction error. The ratio greater than four is advisable and designates adequate model distinction. In this work, the rate is found to be 24.49, which stipulates the liableness of the experiment data. The coefficient of variation (CV = 0.64) and standard deviation (SD = 0.42) indicate the gradation of accuracy. The low values of CV and SD manifest the acceptability with which the experiment is carried through (Mourabet et al. 2017a).

3.6.1 Interaction of variables

The shape of the contour plots provides the information on the nature and extent of the interactions. The interaction of process variables is shown in Figure 3.11, where Figure 3.11(b), 11(c) and 11(d) represents the interactions between A-(pH) – B- (concentration of Chromium solution), A-(pH)- C-(catalyst loading) and B and C (Concentration and catalyst dosage), respectively. The optimum pH at which the maximum photocatalytic Chromium removal was observed as 1 for 0.4 g/L catalyst loading and at an initial concentration of 10 ppm.

The RSM model was validated by conducting experiments. The deviation of the measured value from the predicted value is given by the predicted versus actual value plot in Figure 3.11(a). The closeness of the predicted value and measured value depicts the ideal line. The deviation of the measured value from the ideal line indicates the accuracy of the design. The RSM contour plots on the effect of two independent variables on degradation, while keeping one variable constant are depicted in Figure 3.11. In Figure 3.11(b), the interaction of pH and initial concentration is shown. Figure shows that the Chromium removal efficiency increases as the pH decreases for a concentration of 10 ppm. Figure 3.11 (c) and (d) show the effect of catalyst dosage, and pH on the concentration of Chromium. The removal percentage is higher at the following conditions; catalyst dosage - 0.4 g/L and an initial concentration -10 ppm at a constant pH – 2.0. The lower pH favours the higher Chromium removal for a TiO_2-WO_3 catalyst loading of 0.4 g/L. The lowest pH of 1 and 2 offers higher degradation percentages.
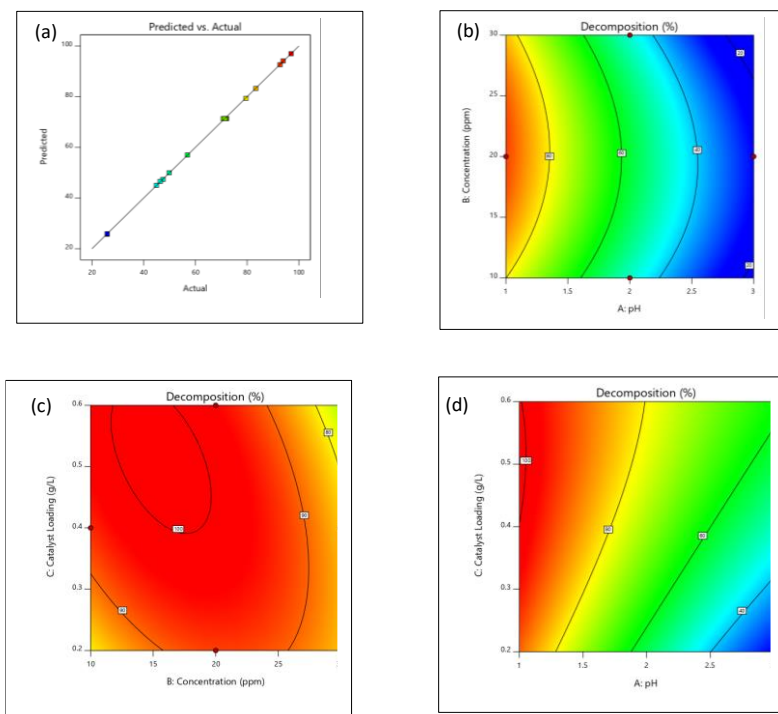
Figure 3.11 Contour plots representing the effect of interaction of different variables on degradation of Chromium (VI). (a) Predicted versus actual value plot, (b) effect of pH/concentration (ppm) on degradation (at a catalyst loading 0.4 g/L), (c) effect of catalyst loading and concentration on degradation (at pH 1), (d) effect of pH/catalyst loading on degradation (at an initial concentration of 10 ppm).

3.7 CONFIRMATORY REDUCTION TEST

A model was developed using RSM via design expert software. Initial experiments were conducted to get the optimal reduction using the OVAT method. The optimized variables were used in RSM to develop a model to predict the percentage of degradation. The predicted values were confirmed with raw experimental data. The final optimized values to achieve maximum degradation are pH 1, 20 ppm Chromium solution, and 0.4 g/L catalyst loading. The predicted and experimental values are comparable with each other.

CHAPTER 4

PHOTOCATALYTIC REDUCTION OF CHROMIUM (VI) USING TiO$_2$-SnO$_2$ METAL-OXIDE 7SEMICONDUCTOR CATALYST

4.1 INTRODUCTION

The excess amounts of heavy metals in water bodies cause a menace to social well-being. Heavy metal removal is a key to avoid this threat. The most commonly found heavy metals are cadmium, arsenic, zinc, lead, nickel, and chromium. Among the heavy metals, Chromium is one of the most toxic and is discharged as tannery, electroplating, acid mining, paint, dyes, and pigment wastewater. Chromium concentrations may intoxicate the food chain (Cheng et al. 2015; Ekramul Mahmud et al. 2016; Vellaichamy et al. 2017). Chromium exists in nature as Cr(III) and Cr(VI) oxidation states. Rendering to the California Department of Public Health advises Cr(VI) to limit to 0.01 mg/L of drinking water (Yin et al. 2018). According to Indian standards, the limit of Cr(VI) in the potable water is 0.05 mg/L. Cr(VI) remediation technique includes chemical reduction processes, ion exchange, evaporation, coagulation-flocculation, membrane filtration, adsorption, and photocatalysis (Peng et al. 2019; Shankar 2009). Semiconductor-sensitized photoreactions with TiO$_2$-like nanoparticles have drawn the researchers' attention due to their applicability in degrading an extensive variety of environmental pollutants, easy availability, and high turnover (Asha and Kumar 2015a; Marinho et al. 2017a; Sane et al. 2018). The photoexcited charge carriers have a flash recombination time in the shorter ranges of 10^{-8} – 10^{-3} sec, which reduces the overall quantum efficiency (Liu et al. 2019).

A wide variety of photocatalysts have also been employed to remove metal pollutants, including TiO$_2$, Zn, CdS, ZnS, WO$_3$, etc. TiO$_2$ is the most widely used metal oxide photocatalyst due to its non-toxicity, chemical stability, easy availability, and high turnover (Asha and Kumar 2015a). The photoactivity under visible light is greatly hampered by the higher bandgap of the metal oxide semiconductor stated above. The bandgap reduction of a semiconductor by combining it with other semiconductor has given a way for a new research focus in recent years. To reduce the recombination of photo-excited charge

carriers, TiO_2 can be coupled with SnO_2, which is a wider bandgap semiconductor (3.8 eV) (Hassan et al. 2019).

The mixing of TiO_2 with SnO_2 will reduce selectivity and upsurge the surface area through evading grain growth (Mendonça 2017; Patil et al. 2018). The major problem in photocatalysis is electron-hole recombination and the low reaction rate can be alleviated using hole scavengers. Addition of right quantities of these reducing species to the reaction mixture prevents the electron-hole recombination. Citric acid is one of the majorly recommended scavenger which can enhance the photon efficiency of the Cr(VI) reduction (Kabra et al. 2008). To the best of our acquaintance, photocatalytic removal of Cr(VI) with TiO_2-SnO_2 is reported nowhere in the literature.

This work demonstrate the following objectives; (i) synthesis and characterization of TiO_2-SnO_2 catalyst; (ii) removal of Cr(VI) using TiO_2-SnO_2 catalysts under visible light (by evaluating the effect of pH, initial concentration, catalyst loading and citric acid concentration on photoreduction of Cr(VI) to Cr(III)). It is anticipated that the TiO_2-SnO_2 will show a better removal efficiency of Cr(VI) under visible light in the presence of citric acid.

4.2 MATERIALS

Titanium isopropoxide (TTIP, Ti[OCH(CH)]), tin(IV) chloride pentahydrate ($SnCl_4.5H_2O$) of Sigma Aldrich, $K_2Cr_2O_7$ of 99% purity, from Merck and Anhydrous citric acid ($C_6H_8O_7$) obtained from Loba Chemie Pvt Ltd, India were used without any further purification. All the solutions were prepared in deionized water throughout the experiment.

4.3 METHODS

4.3.1 Synthesis of catalyst

TiO_2-SnO_2 catalyst was prepared using titanium isopropoxide (TTIP, Ti [OCH(CH)]), and tin (IV) chloride pentahydrate ($SnCl_4.5H_2O$) as precursors. Solution mixture containing 5 mL of TTIP, 13 mL of ethanol and 4 mL glacial acetic acid was stirred for 30 min and 5 mL of deionized water was added for hydrolysis. The reaction mixture was kept under vigorous stirring for 30 min to get a transparent sol. To this, a calculated amount of tin (IV) chloride pentahydrate ($SnCl_4.5H_2O$) was added to have various molar ratios (10:1, 20:1, 30:1, and 40:1) and stirred for another 1 hour to get yellow-coloured solution. The above

solution was transferred to a Teflon-lined autoclave and heated at 200°C for 24 h in an electric oven. After the reaction time, the autoclaved mixture was cooled to room temperature. The mixture was then washed with scopious ethanol and water. The final product was dried at 60°C overnight, and then powdered and stored for further use. The prepared TiO_2-SnO_2 catalyst with molar ratios 10:1, 20:1, 30:1, and 40:1 was designated as TS10, TS20, TS30, and TS40, respectively.

4.3.2 Characterization of materials

The morphology of the prepared samples was analysed using a JEOL/JEM 2100 Transmission Electron Microscope (200 kV, LaB6 Electron gun, with a point resolution of 0.23 nm). The catalyst samples were prepared and stored in a vacuum desiccator before analysis to remove moisture. The structural characteristics of nanoparticles were analyzed using XRD JEOL DX-GE-2P Goniometer operated at room temperature, at an accelerating voltage of 30 kV using CuKα radiation (λ = 0.15406 nm), with scattering angle from 20° to 80°. X'pert HighScore Plus software was used to analyse diffraction patterns. The crystallographic characteristics were performed using the ICDD (International Centre of Diffraction Data) database. The specific surface area of the prepared sample was calculated by Brunauer-Emmett-Teller (BET) analysis. Barrett- Joyner Halenda (BJH) analysis was used to determine the pore size distribution of the prepared samples. Hitachi U-2900 Spectrophotometer was used to analyse the prepared catalyst's bandgap energy and to estimate Cr(VI) concentration in the solution. XPS (X-ray Photoelectron Spectroscopy) analysis was performed in ultra-high vacuum using Omicron ESCA$^+$ instrument. SEM-EDX (Scanning Electron Spectroscopy – Energy Dispersive X-Ray) analysis was used to calculate the nanoparticle surface elemental compositions. ATR-FTIR spectra (Attenuated Total Reflectance-Fourier Transform Infrared Spectroscopy) were obtained to analyse the functional group present in the prepared catalyst. ICP-OES (Inductively Coupled Plasma-Optical Emission Spectroscopy, Agilent Tech) was used for elemental analysis of the Cr(VI) samples before and after reduction studies.

4.3.3 Chromium reduction study using TiO_2-SnO_2 photocatalyst

TiO_2-SnO_2 catalyst was prepared by the hydrothermal method and its reduction capacity of Cr(VI) under 400 W metal halide visible light source (2600 Lux) in a 100 mL reaction volume was analysed. The Chromium reduction was carried out using TiO_2-SnO_2 catalysts prepared using different molar ratios (10:1 to 40:1) and varying the parameters such as pH

(3 to 9), catalyst loading (0.2 - 0.8 g/L), initial Chromium (VI) concentration (10-30 ppm), and scavenger loading (0.2 - 0.8 g/L). The reduction reaction was carried out till the concentration reached equilibrium.

The direct UV –Visible spectrometry was used to analyse the amount of chromium (based on the natural colour of chromate ion) in the solution to avoid excessive dilution of samples and also due to the limited stability of DPC-Cr(VI) complex in the diphenylcarbazide (DPC) method. The Cr(VI) ions under acidic conditions (pH 2.0 - pH 5.6) exist in hydrogen chromate ion form ($HCrO_4^-$), and at a pH above 6.4 exist as chromate (CrO_4^{2-}) ions. The absorbance peak at 350 nm is considered to get the unknown concentration of Chromium (VI) in the reaction mixture. The unknown concentrations of Cr(VI) solutions were calculated using a calibration curve.

The reduction of Cr (VI) is reported as:

$$Cr \ (VI) \ remaining \ (\%) = C/C_o \qquad\qquad \rightarrow (1.0)$$

Where C_o is the initial concentration (ppm) of Cr (VI) and C is the concentration (ppm) after an irradiation time, t.

4.4 RESULT AND DISCUSSION

4.4.1 X-Ray Diffraction Analysis

Figure 4.1 represents X-Ray diffraction patterns of TiO_2-SnO_2 catalysts synthesized at different molar ratios like 10:1, 20:1, 30:1, and 40:1. The presence of Sn ions and TiO_2 anatase and rutile forms was found in all the catalysts. The significant peaks were observed at 25.70º and 38.42º which correspond to anatase phase planes (101) and (004) of TiO_2 (ICDD 01-075-1537) respectively.

The peak position of (101) anatase plane is shifted to a larger diffraction angle, which confirms the co-existence of both rutile and anatase phases. The co-existence of anatase and rutile phases may result in a decreased lattice spacing. The peak at 27.68º corresponds to (110) rutile plane of TiO_2. The peak at 54.67º corresponds to (221) rutile SnO_2 plane (ICDD 01-088-1172) which is as shown in Figure 4.1, and the peak is only present in TS catalysts, which differentiates the TiO_2 spectrum from other spectra. The peak shift observed at 53.18º corresponds to rutile SnO_2 (220) whereas the anatase phase disappeared (ICDD 00-050-1429). The peak at 63.35º represents (311) plane of rutile plane of SnO_2

(ICDD 01-050-1429). The peak at 34.51° attributes to the rutile (101) plane of SnO_2, as reported by Bolagam et al. (Bolagam et al. 2017). The results indicates that Sn^{4+} ions have been successfully incorporated into the crystal lattice sites of the TiO_2 to form TiO_2-SnO_2 metal oxide composite.
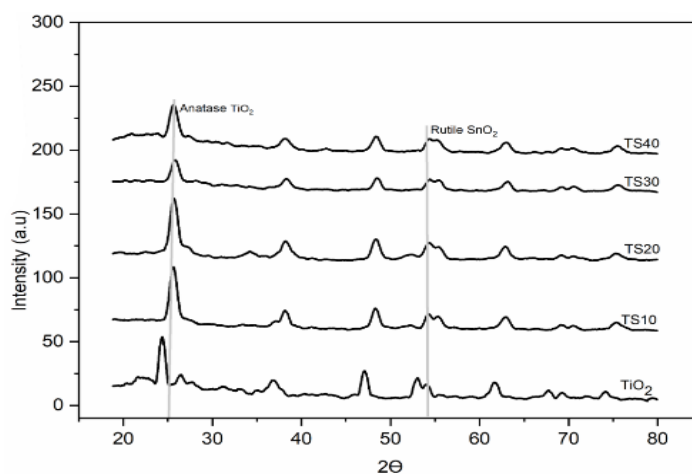
Figure 4.1 X-ray diffraction pattern of TiO_2, TS10, TS20, TS30 and TS40 catalyst.

4.4.2 ATR-FTIR Analysis for photocatalysts

The ATR-FTIR spectra of TiO_2-SnO_2 catalyst and pure TiO_2 are shown in Figure 4.2. The peak at 3491 cm^{-1}, is assigned to the stretching vibration of ^-OH and physically adsorbed water on the catalyst surface. Peak at 1631 cm^{-1} is related to the bending vibration of hydroxyl groups on the oxides' surface (Shaposhnik et al. 2012). The broad band observed between 1000 - 633 cm^{-1} is associated with the stretching vibrations of bridged Sn-O-Sn, Ti-O-Ti and Ti-O-Sn bonds of titanium and tin oxides (Arora et al. 2014; Hassan et al. 2019a; Magdalane 2019).
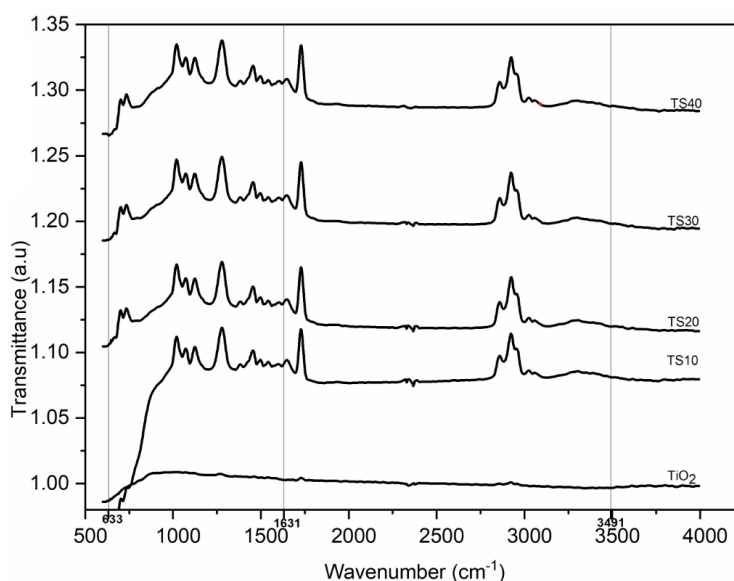
Figure 4.2 ATR-FTIR spectra for TiO_2, TS10, TS20, TS30 and TS40 catalyst.

4.4.3 BET Analysis

The BET surface area and BJH analysis data for TiO_2, TS10, TS20, TS30, and TS40 catalyst are tabulated in Table 4.1.

Table 4.1 The BET surface area and BJH analysis data for TiO_2, TS10, TS20, TS30 and TS40 catalyst.

Catalyst	Surface area (m²/g)	Pore volume (cc/g)	Pore diameter (nm)
TiO_2	45.551	0.214	2.189
TS10	100.182	0.193	6.036
TS20	109.485	0.208	6.041
TS30	148.526	0.254	6.016
TS40	166.637	0.243	6.066

Pure TiO_2 has the lowest surface area among all the prepared catalyst and as the Sn content increases, the surface area increases to 3- 4 times the surface area of TiO_2 as listed in Table 4.1. TS40 catalyst showed the highest surface area of 166.63 m^2/g and TS10 showed the lowest surface area of 100.182 m^2/g, which can be due to the existence of rutile TiO_2 in the catalyst (Hassan et al. 2019). The photocatalytic activity of the catalyst is directly related

66

to the total active surface and the availability of additional active sites for adsorption and desorption of metal pollutants (Vellaichamy et al. 2017b);(Mugunthan et al. 2019).

4.4.4 Bandgap analysis of photocatalysts

The prepared TiO$_2$-SnO$_2$ catalysts were subjected to photo-absorption studies in UV-Visible spectrophotoscopy. The bandgap of the catalyst was estimated using Tauc's relation. The obtained bandgap is 2.87 eV as shown in Figure 4.3. The bandgap energy of the TiO$_2$-SnO$_2$ metal oxide semiconductor is lower than the bandgap of the individual metal oxides (TiO$_2$ and SnO$_2$) and it will be active in the visible light region (Magdalane et al. 2019).
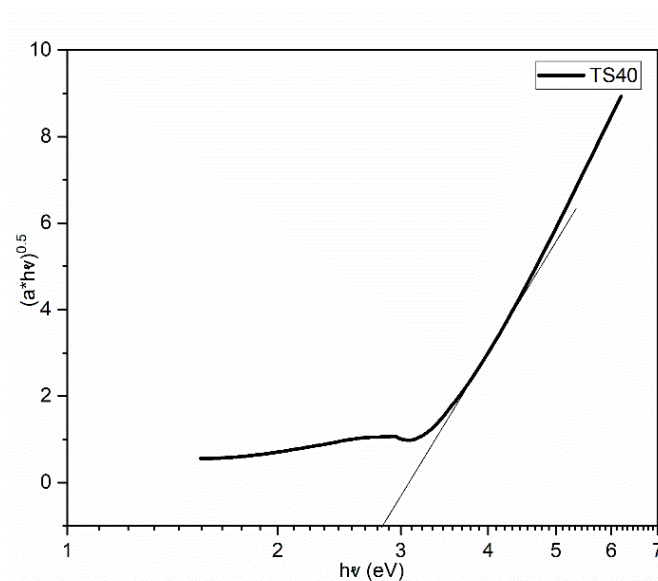
Figure 4.3 The band gap of prepared catalyst.

4.4.5 Morphological analysis of the photocatalysts

The photocatalytic performance of the catalyst depends on the catalyst geometry and catalyst size. The TEM images and lattice spacing for different catalysts (TS10, TS20, TS30, and TS40) are shown in Figure 4.4. From the image it is clear that the average size of TiO$_2$-SnO$_2$ catalysts ranges from 11 nm to 16 nm.
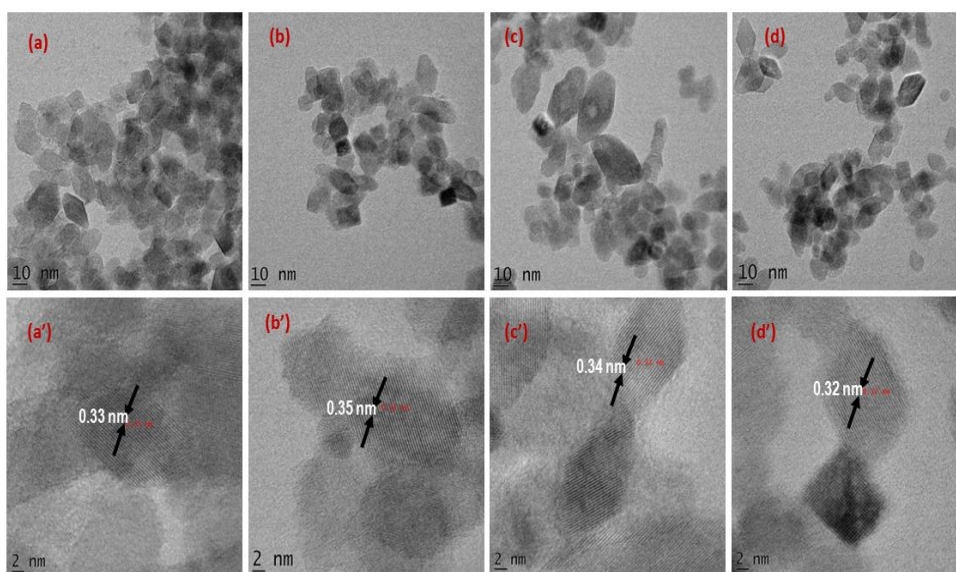
Figure 4.4 TEM (Transmission Electron Microscopy) image of particular catalyst and lattice spacing obtained for (a,a'). TS10 (0.33 nm), (b,b'). TS20 (0.35 nm), (c,c'). TS30 (0.34 nm) and (d,d'). TS40 (0.32 nm) catalyst.

Table 4.2 Size (nm), lattice spacing and corresponding planes obtained from TEM analysis

Catalyst	Avg. size	Lattice spacing	d-spacing in SAED
TS10	14.17 nm	0.33 nm	SnO_2 (110)
TS20	11.96 nm	0.35 nm	TiO_2 (A)
TS30	15.84 nm	0.34 nm	TiO_2 (101)
TS40	11.97 nm	0.32 nm	SnO_2 (R) (110)

The particle size and surface area are the key factors in the adsorption of pollutants in a photocatalytic reaction. In this research, through hydrothermal route we could achieve quantum sized particles (in Table 4.2), which also matches with the reported literature (Huang et al. 2015a). The analysis provides information on the phase composition as well as the spatial distribution of TiO_2 and SnO_2. Atomic planes with a lattice spacing of 0.33 nm (TS10), 0.35 nm (TS20), 0.34 nm (TS30) and 0.32 nm (TS40) corresponds to SnO_2, TiO_2 (anatase) and TiO_2 (rutile) phases. These results are consistent with XRD analysis results for the TiO_2-SnO_2 catalyst. The planes correspond to (110) and (101) (rutile TiO_2, SnO_2 and anatase TiO_2) were also present in the XRD results.

4.5 PHOTOCATALYTIC REDUCTION STUDIES FOR CHROMIUM (VI)

4.5.1 The effect of catalyst molar ratio on photoreduction of Chromium (VI)

The Chromium reduction was carried out using TiO_2-SnO_2 catalysts prepared using different molar ratio from 10:1 to 40:1 using the following condition; constant pH of 2, catalyst loading 0.6 g/L and an initial concentration of 10 ppm, as shown in Figure 4.5. The catalyst 40:1, showed a faster reduction compared to the other catalysts and for further study, the TS40 catalyst was used. Further, it was observed that the reduction reaction started approaching equilibrium from 180th min.

The TS30 has the lowest reduction efficiency compared to TS10 and TS20 and this might be due to the defects formed during the catalyst synthesis, which acted as recombination centres, and hence lowered the efficiency. The catalysts with molar ratio 40:1 and 10:1 have a higher surface area than 20:1 and 30:1, but coupled semiconductor catalyst TiO_2-SnO_2 had improved surface area than pure TiO_2, and also, the effect of Sn loading enhanced the catalytic activity.
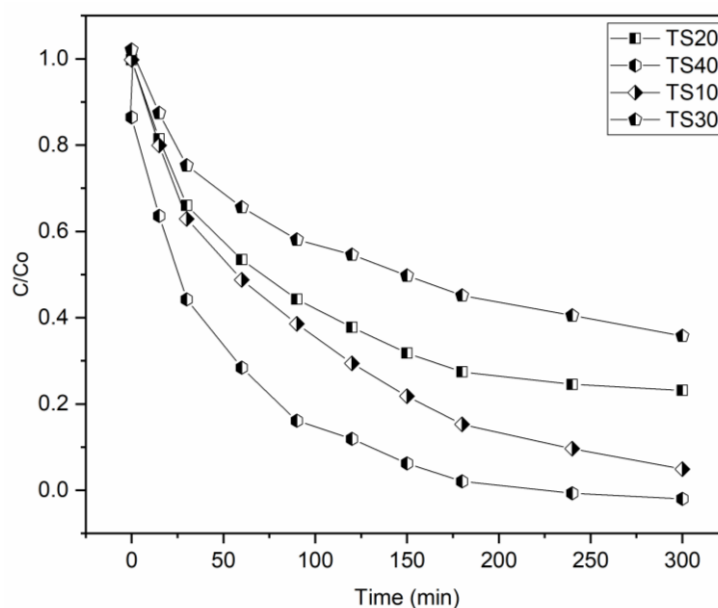
Figure 4.5 The effect of catalyst molar ratio on photoreduction of Chromium (VI)

4.5.2 The effect of initial concentration on photoreduction of Chromium (VI)

The effect of the initial concentration of Chromium solution on Chromium (VI) reduction was investigated over the range of 10 to 30 ppm at a constant pH and at a catalyst loading of 0.6 g/L. The results show that the reduction efficiency gradually decreases with an

increase in initial concentration, as given in Figure 4.6. After 120 min of reduction, there was a slight increment in chromium (VI) concentration, and this indicates the reoxidation of Chromium (III) to Chromium (VI) in the presence of excess OH$^-$ in the solution. The low efficiency at a higher initial concentration of Chromium (VI) solution will be due to the availabilities of fewer active sites for the photoreduction (Baloyi et al. 2014); (Marinho et al. 2017). From the result, Cr(VI) with a lowest concentration (10 ppm) showed complete Cr(VI) reduction within 120 min. For further experiments 10 ppm solution was used as the initial pollutant concentration.
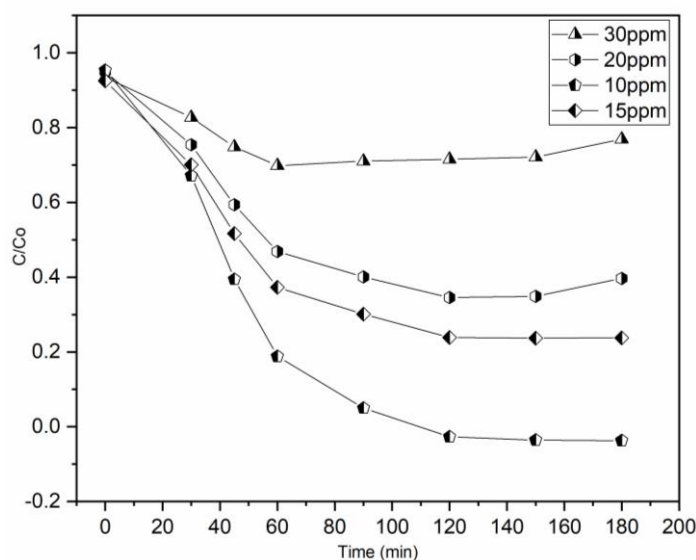
Figure 4.6 The effect of initial concentration on the photoreduction of Chromium (VI)

4.5.3 The effect of pH on photoreduction of Chromium (VI)

The effect of initial pH on the reduction of Cr (VI) using TiO$_2$-SnO$_2$ photocatalysts under visible light is shown in Figure 4.7. The process was investigated by varying pH from 3 to 9 at a constant photocatalytic dosage of 0.6 g/L and initial Chromium (VI) solution of 10 ppm. The pH of Chromium solution was adjusted to desired value by using 0.1 M H$_2$SO$_4$ and 1N NaOH. The reduction reaction was slower in higher pH, whereas a faster response was observed at pH=3.0. This result implies that a lower pH favours the photocatalytic reduction of Chromium (VI) (Asha and Kumar 2015b). At lower pH, the surface of catalyst gets protonated, and there is a strong electrostatic attraction between the positively charged catalyst surface and oxyanions of Cr(VI) (Ali et al. 2016b). At pH <6.2, HCrO$_7^-$ and Cr$_2$O$_7^{2-}$ ions exists in the aqueous solution. The catalyst surface gets more positively charged due

to the adsorption of H$^+$ ions on to the surface of catalysts at acidic pH. The Cr(VI) adsorption takes place on the surface and the reduction occurs.
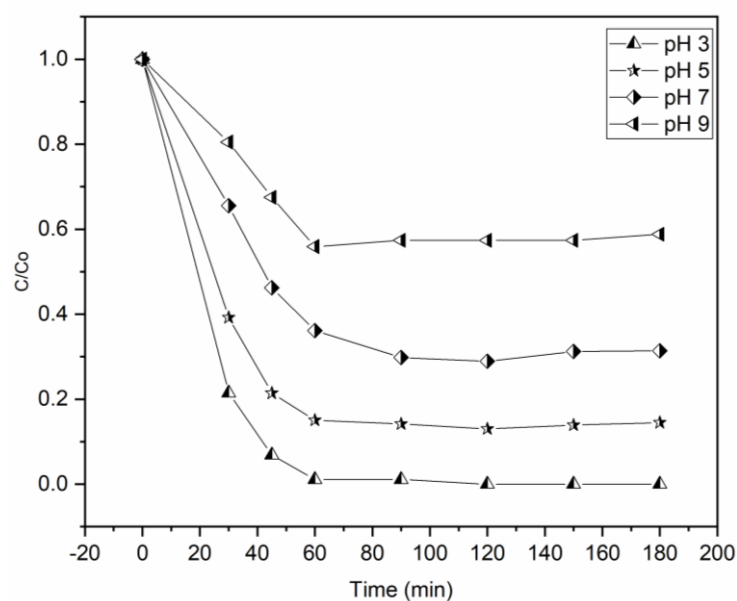
Figure 4.7 The effect of pH on photoreduction of Chromium (VI)

4.5.4 The effect of catalyst loading on photoreduction of Chromium (VI)

The effect of catalyst loading on Chromium (VI) reduction was investigated by varying the dosage of catalyst from 0.2 g/L to 0.8 g/L at a constant pH of 3.0 as shown in Figure 4.8. The catalyst's photocatalytic activity is directly related to the total active surface and the availability of additional active sites for adsorption and desorption of metal pollutants (Mugunthan et al. 2019; Vellaichamy et al. 2017). The higher the adsorption capacity, the higher will be the photocatalytic reduction efficiency. It was observed that the Cr(VI) reduction increased till 0.6 g/L catalyst dosage and after that reduction efficiency decreased considerably. The excess catalyst dosage incites the light scattering and screening effect, which intern reduced the photocatalytic activity of the catalyst (Mugunthan et al. 2018a).
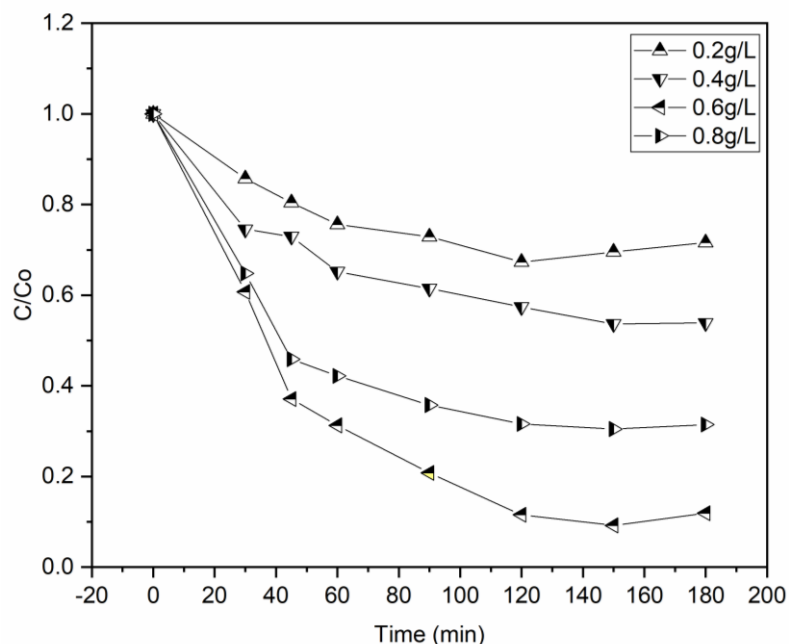
Figure 4.8 The effect of catalyst loading on photoreduction of Chromium (VI)

At a catalyst loading of 0.8 g/L, the reduction efficiency is low compared to 0.6 g/L catalyst loading, which is described in Figure 4.8 and could be due to the unavailability of active sites for adsorption of Cr(VI) species (Yin et al. 2018). The catalyst loading of 0.6 g/L is thus considered as optimum loading, at which the Cr(VI) reduction is maximum at a given catalyst loading (Sane et al. 2018). Figure 4.8 shows that Cr(VI) concentration reduces gradually till 120 min and after that the Cr(VI) in the reaction mixture increased. This can be due to the complete utilization of H^+ for the reduction of Cr(VI) and the .OH radicals were reacting with the h^+ , which has caused the reoxidation of Cr(III) to Cr(VI). The entire process is depicted in equations (2-5).

TiO_2-SnO_2 + hν → h^+ + e^- $\qquad\qquad\qquad\qquad$ → (2.0)

$Cr_2O_7^{2-}$ + 14 H^+ + 6e^- ↔ 2Cr^{3+} + 7 H_2O $\qquad\qquad$ → (3.0)

H_2O + h^+ → ·OH + H^+ $\qquad\qquad\qquad\qquad\qquad$ → (4.0)

Cr (III) + h^+ (·OH) → Cr(VI) + HO^- $\qquad\qquad\qquad$ → (5.0)
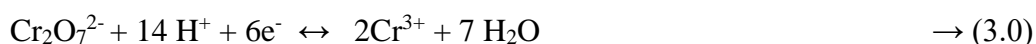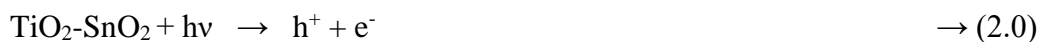
4.6 SCAVENGING STUDIES

The chromium reduction, carried out under visible light using TiO_2-SnO_2, showed a gradual decrease in chromium (VI) concentration, up to 120 min, and then the Chromium (VI) concentration increased. Gradual increase in Chromium concentration could be due to the

rise in the holes, which is contributed by the excess hydroxyl groups, leading to the reoxidation of Chromium (III) to Chromium (VI). These shortcomings are suppressed by adding chelating agents like citric acid (Ngo et al. 2018). Meichtry et al. studied Chromium (VI) reduction using TiO_2 nanoparticles in the presence of citric acid as a radical scavenger. Thus, it is revealed that the reoxidation of Cr(III) to Cr(VI) was arrested using a sacrificing agent like citric acid (Meichtry et al. 2007).

The Figure 4.9 depicts the reduction of Cr(VI) using different concentration of citric acid (CA) as scavenger. The citric acid ($C_6H_8O_7$) anhydrous of different concentrations (0.2 g/L,0.4 g/L, 0.6 g/L, and 0.8 g/L) are added to 15 ppm Chromium solution of pH 3.0 and with a catalyst loading of 0.4 g/L TS40 (40:1). The hexavalent Chromium reduction to trivalent Chromium consumes 3 electrons (Marinho et al. 2017a). The equations (6), (7), and (8) represents the reactions involved in the photoreduction,

$$HCrO_4^- + 7H^+ + 3e^- \leftrightarrow Cr^{3+} + 4H_2O \qquad \rightarrow (6.0)$$

And in solution,

$$H_2O + h^+ \leftrightarrow OH^- + H^+ \qquad \rightarrow (7.0)$$

In the presence of citric acid,

$$4Cr_2O_7^{2-} + C_6H_5O_7^{3-} + 41\ H^+ + 6e^- \leftrightarrow 8Cr^{3+} + 6CO_2 + 23\ H_2O \qquad \rightarrow (8.0)$$
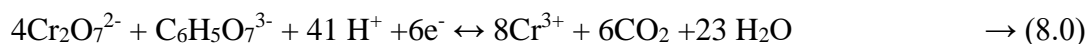
The h^+ ions in the valence band (VB) diffuses to the TiO_2 surface and adsorbed water molecules forms hydroxyl radical (equation 3.0) (Khaki et al. 2017), which will oxidize Cr(III) to Chromium (VI). The Chromium (VI) is reduced with one electron, and Cr (V) will form in the solution. This Cr(V) reacts to create a very stable and carcinogenic Cr(V)-Citric acid complex. Finally, on photoreduction, this complex is converted to less noxious Cr(III) (Meichtry et al. 2007; Ngo et al. 2018). According to Pingfan Xu et al. (2018), citric acid can separate the photogenerated electron-hole pair on the catalyst's surface, and it prevents the oxidation of reduced Cr species. Citric acid captures photogenerated holes in the solution, and also, it combines with Chromium (VI) to form a stable complex and thereby increase the reaction rate (Xu et al. 2018), which is depicted in equation (8.0).

The reduction reaction was faster in the presence of citric acid, and as the citric acid concentration increased, the reduction of Chromium (VI) also increased. The complete reduction happened within 30 min, and the yellow-coloured Chromium solution changed

to colourless liquid for a citric acid loading of 0.8 g/L. The TiO_2-SnO_2 catalyst became green coloured, indicating the presence of Chromium (VI and III) adsorption. The percentage reduction obtained is 94.7% in the presence of 0.6 g/L of catalyst for a duration of 1 hour, and 0.4 g/L loading showed complete degradation after 90 min of photocatalytic reaction. The result was slower for 0.2 g/L citric acid loading and reached a reduction efficiency of 88.53% in 180 min. The experimental values shows that Cr(VI) reduction increases with an increase in initial citric acid concentration. These results are also comparable with the results by Jeffrey et al. (2014) (Baloyi et al. 2014).

4.7 XPS ANALYSIS
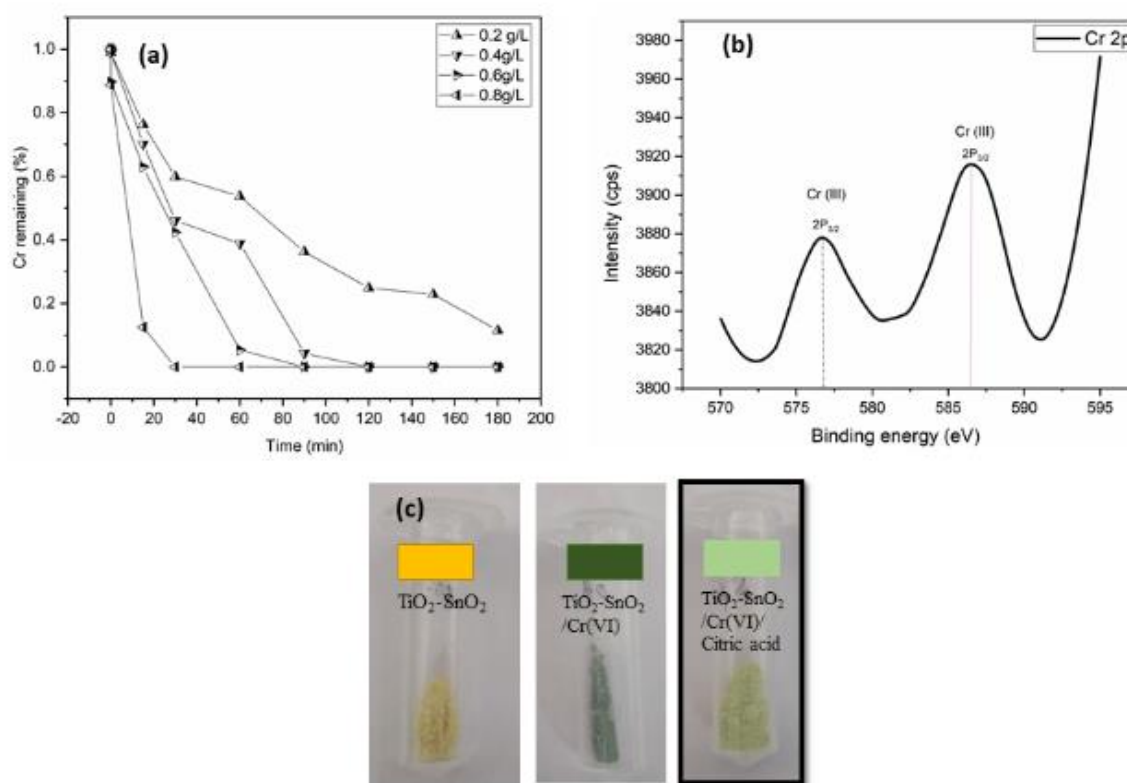
Figure 4.9 (a). Scavenging studies using CA, (b). XPS pattern for the catalyst after scavenging studies, (c). The colour of the catalyst in original, after Cr(VI) reduction and after reduction using CA

TiO_2-SnO_2 (TS40) catalyst were collected and dried after the Chromium reduction reaction carried out at optimum conditions (15 ppm Cr(VI) solution, 0.6 g/L catalyst loading, pH 3.0, and 0.8 g/L citric acid loading). The light green coloured samples (Figure 4.9(c)) were subjected to XPS analysis and the spectra obtained are shown in Figure 4.9(b). The Auger

peak observed at binding energies of 576 eV and 586 eV corresponds to Cr(III), which implies that the Chromium (VI) reduced to Cr_2O_3 in the presence of citric acid under visible light and adsorbed on the TiO_2-SnO_2 catalyst (Biesinger et al. 2011). At lower pH (pH< 5), the Cr(III) exists in the form of Cr_2O_3 (Biesinger et al. 2011), whereas in higher pH, pH>5, Cr(VI) exist in the form of $Cr(OH)^{2+}$ because $Cr(OH)_3$ was the main species under this pH (Liu et al. 2014).

4.8 KINETICS OF PHOTOCATALYTIC REDUCTION OF CHROMIUM (VI)

The photocatalytic degradation kinetics of scavenging experiments were performed. The kinetic results show that the photocatalytic reduction of Chromium (VI) follows pseudo-first-order reaction (Figure 4.10) which is described as follows,

$$r = dC/dt = - kC \qquad\qquad \rightarrow (9.0)$$

Where r, C, k, and t represent the rate of photocatalytic reduction, Chromium (VI) concentration, the rate constant, and time respectively. The rate constants are obtained by fitting the experimental data to the first-order kinetic equation,

$$-\ln C/Co = kt \qquad\qquad \rightarrow (10.0)$$
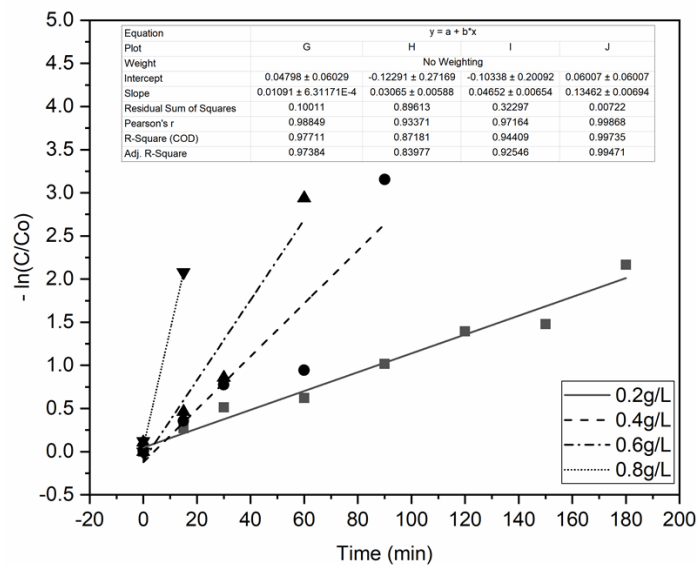
Figure 4.10 Kinetic studies of TiO_2-SnO_2 catalyst with varying citric acid concentration.

The rate constant, k, and correlation coefficients are listed in Table 4.3. From the slopes, it has inferred that, as the citric acid concentration increases, the rate of reduction reaction increases, and the constant rate value is high for the reaction with 0.8 g/L citric acid.

Table 4.3 Kinetic analysis of TiO$_2$-SnO$_2$ catalyst with varying citric acid concentration.

Equation	y = a + b*x			
Plot	0.2g/L	0.4g/L	0.6g/L	0.8g/L
Slope	0.011±6.311E-4	0.030±0.005	0.046± 0.006	0.134 ± 0.006
Residual Sum of Squares	0.100	0.896	0.322	0.007
Pearson's r	0.988	0.933	0.971	0.998
R^2 (COD)	0.977	0.871	0.944	0.997
Adj. R^2	0.973	0.839	0.925	0.994

4.9 REPEATABILITY AND STABILITY OF THE CATALYST

The stability of the catalyst is a notable feature for its industrial application (Acharya et al. 2018). The repeatability and stability of the catalysts were evaluated at optimized conditions in the presence of citric acid (0.8 g/L) for a reaction time of 120 min. The first reduction reaction at the first cycle showed a complete reduction within 30 min. Two sets of reactions were kept simultaneously and evaluated for the Cr(VI) reduction. The catalysts were washed with deionized water several times and recovered after every cycle. After the first cycle, the catalyst in the first beaker was subjected to sonication for activating the reactive sites by avoiding Cr(VI) adsorption on the catalyst surface, whereas filtered catalysts in another beaker are directly taken for the second cycle without sonication. The process was repeated for three cycle and Chromium (VI) reduction was analysed. TiO$_2$-SnO$_2$ catalyst showed excellent reduction efficiency under visible light in the presence of citric acid. The Chromium (VI) reduction efficiency remained the same when the catalysts were sonicated and used. The unsolicited catalyst performance decreased in the third cycle, and a decrease of 17.21 % Chromium (VI) removal was observed. It is more advantageous and economical to use sonication to strip the adsorbed functional groups of Chromium species from the catalytic surface. Even though, the photocatalytic efficiency is not reducing while using sonicated nanoparticles. The separation of these particles from the reaction mixture will make the entire process less economical. The immobilization is better option to avoid this drawback.

4.10 COMPARISON OF OUR WORK WITH OTHERS WORK

Table 4.4 Studies on Chromium (VI) photoreduction

Sl. No	Catalyst	Catalyst loading (g/L)	Light source	Efficiency	Reference
1.	Titania (Presence of oxalic acid)	0.1	High pressure Xenon arc lamp (Osram XBO,450W)	97%	(Testa et al. 2004)
2.	$AgNO_3 – TiO_2$	1.6	Ultraviolet (UV light)	38.1%	(Ma et al. 2012)
3.	TiO_2 impregnated with glutaraldehyde alginate beads	10	Ultraviolet	100%	(Liu et al. 2013)
4.	TiO_2	2	Solar collector with trough collector (650-800 W/cm^2)	90-92%	(Singh and Chaudhary 2013)
5.	Nanotitania	0.1	White fluorescent Lamp (3000 Lux, 15W)	42.92%	(Paul et al. 2015)
6.	TiO_2-ZnO	1	125 W medium type UVC lamp	99.99%	(Naimi-joubani et al. 2015)
7.	TiO_2	2	Natural sunlight (1.6-1.8 mW/cm^2)	60.25%	(Djellabi et al. 2016)
8.	$ZnO/ZnAl_2O_4$	2	500 W high pressure Hg lamp	92.5-100%	(Yuan et al. 2017)
9.	TiO_2	0.5	UV lamp	79%	(Sane et al. 2018)
10.	$Bi_2(O,S)_3$ and Zn(O,S)	0.4	150 W Halogen visible lamp	99.5%	(Ahmed et al. 2019)
11.	**TiO_2/WO_3**	**0.4**	**400 W metal halide lamp**	**97.91%**	**Our work**
12.	**TiO_2/SnO_2 Presence of 0.8 g/L citric acid**	**0.6**	**400 W metal halide lamp**	**100 %**	**Our work**

The study on photoreduction of Chromium (VI) using various metal oxide semiconductors reported in the literature and our work has been tabulated in Table 4.4.

The following conclusions are drawn from this comparison table.

❖ Catalyst synthesis using hydrothermal method could yield TiO_2-WO_3 and TiO_2-SnO_2 nanocomposites of quantum size and larger surface area.

❖ The higher surface area can give higher reduction at lower catalyst loading. For complete reduction of Cr(VI) 0.4 and 0.6 g/L of TiO_2-WO_3 and TiO_2-SnO_2 catalyst was used.

❖ The selection of the lowest solution pH (pH 1.0 and pH 3.0) could yield better reduction efficiency.

❖ Significant photocatalytic reduction ability was shown by TiO_2-SnO_2 catalyst and sonication helped in catalyst recovery and reduction in catalyst exhaust to a great extent.

❖ TiO_2-WO_3 catalyst showed better performance under visible light without any hole scavengers.

CHAPTER 5

VISIBLE LIGHT ASSISTED PHOTOCATALYTIC REDUCTION OF CHROMIUM (VI) USING PANI/TiO$_2$ NANOCOMPOSITE FROM AQUEOUS SOLUTIONS

5.1. INTRODUCTION

Chromium toxicity in the environment has become a major concern among researchers. Among the different oxidation states of chromium, Cr(VI) is highly soluble in water than Cr(III) at all solution pH and the former is 500 times more toxic than the latter. The conventional methods used for the removal of hexavalent Chromium from polluted water include electrochemical precipitation, chemical coagulation, reverse osmosis, membrane separation, adsorption, etc. (Jahan et al. 2018), (Samani and Molamahmood 2017). The major drawback of TiO$_2$ semiconductors under visible light (wavelength above 400 nm) is their faster recombination of charge carriers due to their wider bandgap, and also their toxicity, which limits their usage in wastewater treatment (Novaković et al. 2016);(Wang et al. 2010b). This can be overcome by doping and further by controlling the particle size. The most promising technique is to dope the TiO$_2$ with conducting polymers.

The electrical tunability, optical and photoelectrical properties, chemical stability, non-toxicity, higher conductivity, and ease of preparation make the conducting polymer Polyaniline an efficient material for various applications (Sharin and Azam 2017);(Vidya et al. 2019); (Dognani et al. 2019);(Eskandari et al. 2020). PANI proved to be a better electron acceptor when combined with metal oxide semiconductors. Pi-conjugated polymer is highly stable under environmental conditions and has a high coefficient of absorption in the visible light region. The recombination of charge carriers can hinder photocatalytic activity in wide bandgap materials like TiO$_2$. PANI can accept holes from the valance band of TiO$_2$ and helps in reducing the recombination of photoradiated charge carriers. The synergistic effect of PANI and TiO$_2$ will enhance the photoactivity of the newly formed nanocomposite.

Zhu et al. prepared a polyaniline-TiO$_2$ nanocomposite for electrochemical biosensor development (Zhu et al. 2015). Huang et al. prepared a superhydrophobic polyaniline-TiO$_2$ nanocomposite for corrosion-resistant coatings. The TiO$_2$ will help to decrease the delamination of the coating (Huang et al. 2020); (Sharin and Azam 2017); (Gilja et al. 2018). According to Deng et al., PANI modified on TiO$_2$ is rich in positively charged amino groups, which can efficiently adsorb Cr(VI) and make the Cr(III) leave the reaction interface quickly (Deng et al. 2020). Cr(VI) or Cr(III) attracts nitrogen atoms in PANI and forms a co-ordinate bond with them. The ion exchange capacity of PANI increases with a decrease in the solution pH (2.0-6.0) (Samani and Molamahmood 2017).

Here in this section, the PANI-TiO$_2$ was prepared using different weight percentages of PANI by the in-situ chemical polymerization method and used for the removal of Cr(VI) under visible light irradiation.

5.2 MATERIALS AND METHODS

5.2.1 Materials

TiO$_2$ Degussa P25, Aniline (An), ammonium persulfate (APS), hydrochloric acid (HCl), 1,5-diphenyl carbazide (DPC) were procured from Sigma Aldrich and K$_2$Cr$_2$O$_7$ was purchased from Merk. All the chemicals were used without any pre-treatment. Throughout the experiment, distilled water was used to prepare solutions.

5.3 METHODS

5.3.1 Synthesis of PANI-TiO$_2$ nanoparticle

The PANI/TiO$_2$ nanocomposite was prepared according to in-situ chemical polymerisation reported by Novakovic et al. (Novaković et al. 2016). The mole ratio of An:APS was kept at 1:1.25 and the nanoparticles were prepared in different weight ratios of PANI and TiO$_2$ (1, 5, 10, and 15 %). The prepared catalyst was designated as PT1, PT5, PT10, and PT15, respectively.

5.3.2 Characterisation

The prepared PANI/TiO$_2$ nanocomposites were characterised using ATR-FTIR (JASCO FTIR-4100) to analyse the surface functional groups, the surface area and pore volume of the nanocomposite were analysed using a BET (NOVA Quantachrom) analyser. The

structural and morphological properties of the nanoparticles was investigated using High resolution-TEM (JEOL/JEM 2100) analysis and the thermal stability of the composite were studied using TGA analysis in nitrogen atmosphere. UV-Visible spectroscopy was used to analyse the Chromium (VI) after the reduction experiment by Diphenyl carbazide (DPC) method at 540 nm. ICP-OES was used to calculate the total Chromium in the initial and final samples.

5.4 RESULT AND DISCUSSION

5.4.1 Characterization of Nanocomposite materials

5.4.1 TEM analysis

The TEM images of the PT15 catalyst at different magnifications are shown in Figure 5.1. PANI polymerization occurred on the surface of TiO_2 and hence the particulate aggregation has reduced a lot (Novaković et al. 2016). All particles appeared in an irregular rectangular sheet like structure, and the size varied from 13.44 nm to 33.83 nm. Figure 5.1(c) shows the lattice planes of nanocrystallites of TiO_2, with a deposition of amorphous material at the grain boundaries. A thin layer of (~1 nm) PANI coating was appeared on the surface of TiO_2 nanocrystallites. Masid et al. and Olad et al. reported 1 nm and 5 nm thick PANI shells on the surface of TiO_2 produced through the in-situ chemical polymerization of Aniline in the presence of TiO_2 (Masid et al. 2015),(Olad and Nosrati 2012).
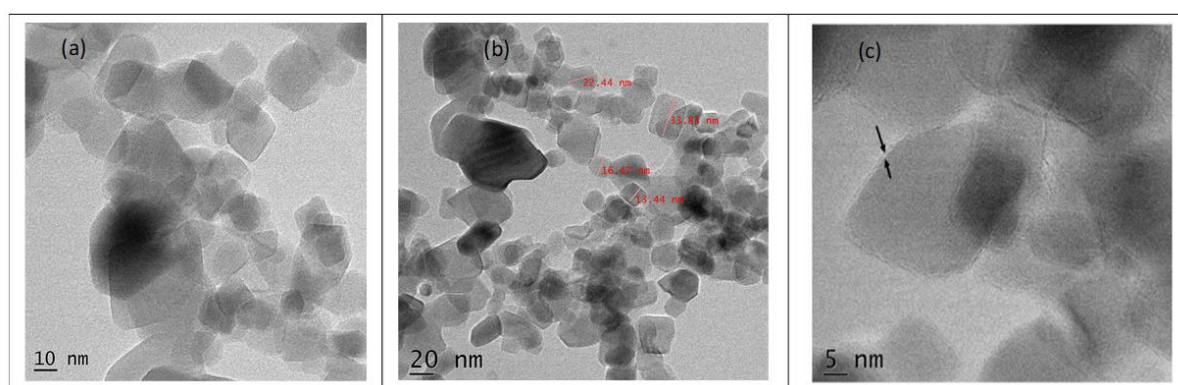
Figure 5.1 (a). TEM image of PT15 nanocomposite, (b). The particle size measured for PT15 ranges from 13.44-33.38 nm and (c). PANI shell on the surface of TiO_2 produced through in-situ chemical polymerization (shown in black arrows).

5.4.2 ATR-FTIR analysis

ATR-FTIR spectra of PANI/TiO$_2$ nanocomposites were analysed in the region of 4000-600 cm^{-1} and it is shown in Figure 5.2. The peak observed between 3380-3560 cm^{-1} are attributed to the stretching vibration of OH- group (Feizpoor et al. 2018), (Sarmah and Kumar 2011). Peak observed at 3457 cm^{-1} (PT10) corresponding to N-H stretching of PANI. Peaks observed at 1586 and 1481 cm^{-1} are attributed to C=N and C=C stretching modes for the quinoid and benzenoid units of PANI. The peaks correspond to 1307 and 1248 cm^{-1} of C-N bond stretching of the quinoid and benzenoid rings of PANI, respectively (Bolagam et al. 2017). The bond stretching corresponds to 697 cm^{-1} representing Ti-O of TiO$_2$. These characteristic peaks in PANI/TiO$_2$ nanocomposites confirm the strong interaction between PANI and TiO$_2$ and the stability of the materials.
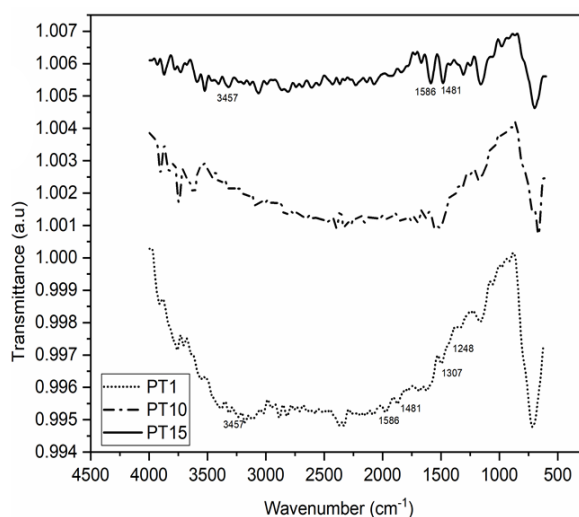
Figure 5.2 ATR-FTIR spectra for PANI/TiO$_2$ nanocomposites

5.4.3 TGA analysis

The analysis temperature was varied from 20°C to 800°C at a heating rate of 10°C. The initial amount and the rate of change of mass of the prepared catalyst sample are given in Figure 5.3. The decomposition of Pristine PANI ES powder (PT0) was observed at 500°C and 820°C. After decomposition and degradation, the total residue obtained was 37.81 % (PT0), 100% (PT1), 93.93% (PT5), 87.97% (PT10) and 86.44% (PT15) respectively. The initial weight loss of nanocomposites was due to the presence of volatile components, moisture, and other adsorbed solvents. There was no significant weight loss for PANI/TiO$_2$ nanocomposites. The presence of metal oxide TiO$_2$ nanoparticles leads to the higher

thermal and oxidative stability of the PANI/TiO$_2$ nanocomposite (Pakizeh et al. 2013);(Alam et al. 2013).
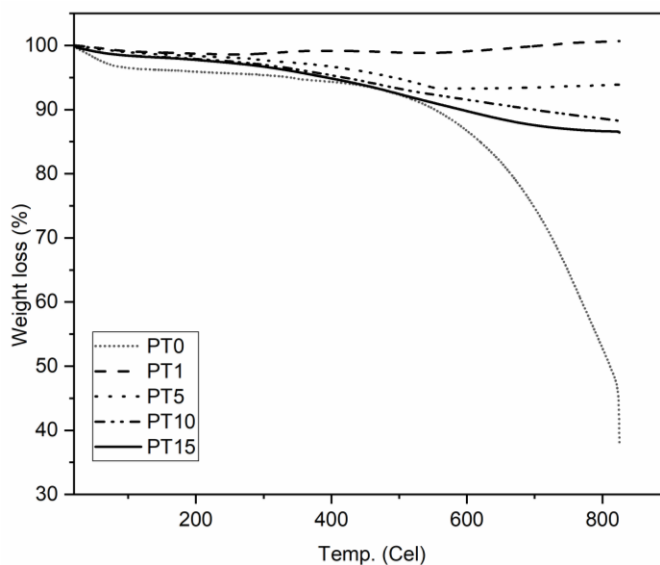
Figure 5.3 TGA curve for PANI/TiO$_2$ nanocomposites

5.4.4 BET analysis

The specific surface area and porosity of the mesoporous PANI/TiO$_2$ nanocomposites were investigated by using the N$_2$ adsorption-desorption isotherm and the Barrett-Joyner-Halenda (BJH) method. The nitrogen adsorption-desorption pattern follows a typical type IV isotherm with an H3 loop, which indicates the formation of aggregated plate-like particles giving rise to slit-shaped pores (Yurdakal et al. 2019). The specific surface areas of the PT1, PT5, PT10 and PT15 nanocomposites were 54.01, 46.08, 42.24 and 47.95 m^2/g, respectively. The prepared PANI/TiO$_2$ nanocomposites have a wider pore size distribution (He et al. 2015). The higher total pore volume and surface area for PT1 than for PT15 nanocomposite indicates that the surface area is an index of physicochemical properties but not a decisive index of photocatalytic activity (Yang et al. 2017). The pore size distribution is 20.12 nm (PT1), 19.59 nm (PT15), 19.92 nm (PT5) and 20.24 nm (PT10) and the particle size distribution is between 5 and 89 nm as shown in Figure 5.4(b).
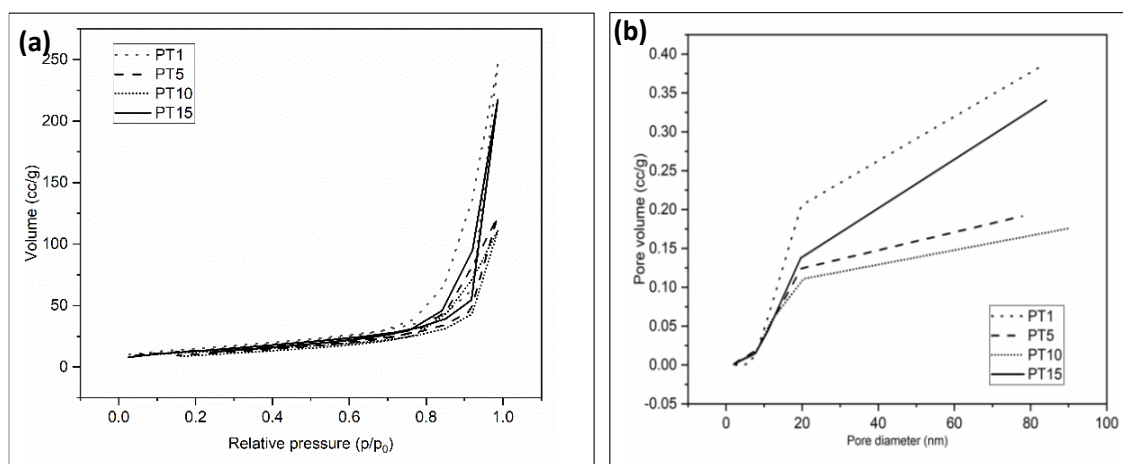
Figure 5.4 (a). Nitrogen adsorption-desorption isotherms of prepared PANI/TiO$_2$ nanocomposites (b). The pore size distributions of prepared PANI/TiO$_2$ nanocomposites.

5.5 PHOTOCATALYTIC REDUCTION OF CHROMIUM (VI)

Cr(VI) reduction experiments were carried out batch-wise in a reaction vessel of 50 mL volume containing 15 ppm Cr(VI) solution, using prepared nanocomposites PT1, PT5, PT10 and PT15 irradiated with a 400 W metal halide lamp for a period of 300 min. Cr(VI) solution consist mainly of $Cr_2O_7^{2-}$ and $HCrO^{4-}$ anionic forms at pH below 6.8. $HCrO_4^-$ ions has a high reduction potential that leads to rapid conversion to Cr(III) under visible light (Qiu et al. 2015). PANI can reduce Cr(VI) to Cr(III) with the quiddity of electron transfer from leucoemeraldine or emeraldine state to pernigraniline state.

It can be seen that after 90 min of visible light irradiation (shown in Figure 5.5), at 1.0 g/L catalyst dosage and pH 3.0, the PT15 showed complete reduction of Cr(VI). The reduction experiment result showed that as the PANI content increases, the Cr(VI) reduction also increases. The colour of the prepared PANI(ES)/TiO$_2$ catalyst changed from dark green to purple, which indicates the deprotonation by superoxidation of the polymer layer on the TiO$_2$ surface. In the presence of visible light, Polyaniline can accept holes from the TiO$_2$ valence band and transfer an excited electron to the conduction band of TiO$_2$. Under visible light irradiation, electrons in the PANI LUMO will shift to PANI HOMO. These electrons then enter into the conduction band of TiO$_2$. Thus, the synergistic effect of PANI and TiO$_2$ under visible light contribute to excess electrons in TiO$_2$ surface for the reduction of Chromium (VI) (Wang et al. 2010);(Sarmah and Kumar 2011). It was observed that after 90 min (for PT15 nanocomposite) of irradiation the colour of the Cr(VI) solution is changed

from yellow to colourless on the complete reduction and the PANI ES changed to the purple (pernigraniline) colour due to oxidation (shown in figure 5.5(a)). PT1 with low PANI content showed the slowest reduction (53.20 %) compared to PT5, PT10 and PT15 nanocomposites under visible light. It can be observed that as PANI content increases, the photoactivity of the TiO_2 extends to the visible region and the nanoparticles become capable of adsorbing Cr(VI) and reducing it into the Cr(III) form. The nanocomposite can be recovered after the reduction reaction and reused for at least three cycles by doping it with 1N HCl.
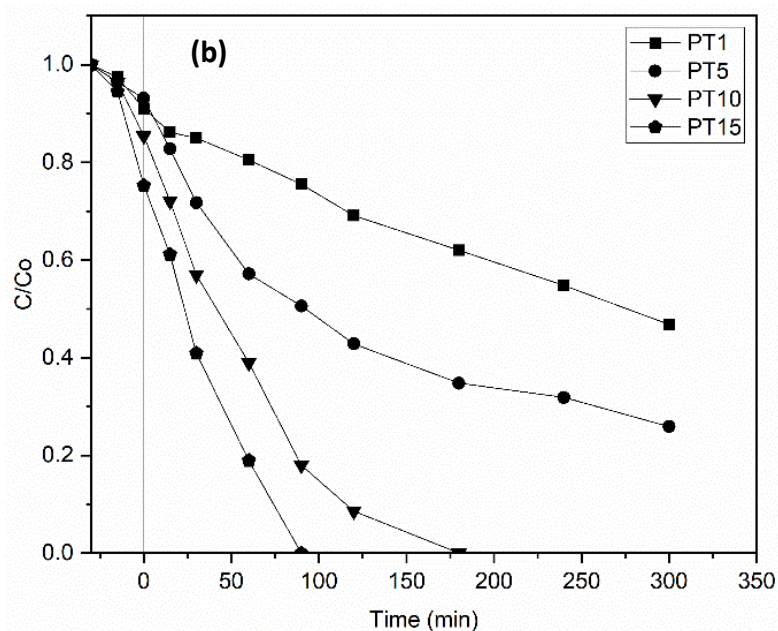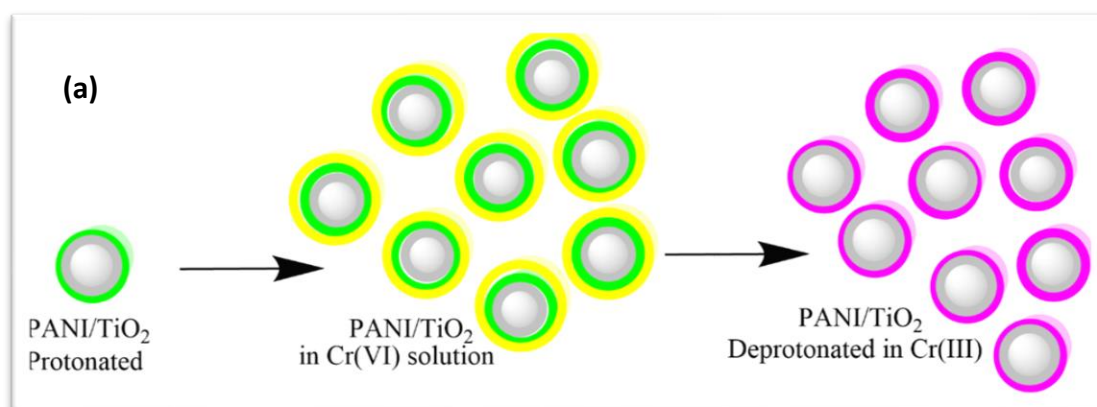
Figure 5.5 (a). Schematic diagram showing photoreduction of Cr(VI) using protonated PANI/TiO_2 nanocomposite, (b). Photocatalytic reduction of Cr(VI) under visible light using PANI/TiO_2.

Even though the PANI/TiO$_2$ nanoparticles are showing better Cr(VI) adsorption and reduction properties, the glitches like recovery of nanoparticles, deprotonation of PANI layer and degradation of Polyaniline in the highly oxidizing atmosphere limits the practical application of these nanoparticles. The other alternative, like the incorporation of nanoparticles in the membrane by coating or blending, will improve the process efficiency.

CHAPTER 6

SYNTHESIS OF POLYANILINE MEMBRANES BY PHASE INVERSION METHOD AND ITS APPLICATION FOR CHROMIUM (VI) REDUCTION AND SEPARATION

6.1 INTRODUCTION

Conjugated polymers such as PANI have gained attention as a membrane material due to their promising characteristics, such as permselectivity and better electrical tunability. Unlike conventional polymers, PANI shows higher conductivity, and hence it is called 'synthetic metal'. Over the past few years, PANI has attracted considerable attention in the fields of electrocatalysis, sensors (Kumar and Yadav 2016), energy conversion, and storage applications. PANI offers ease of preparation, economic viability, environmental stability, higher conductivity, excellent tunable properties, and redox behaviour (Huang et al. 1998);(Ding et al. 2018).

PANI has three oxidation states, which include leucoemeraldine, emeraldine, and pernigraniline. All these types of PANI can be converted into each other by oxidation or reduction in the presence of bases and acids. The amine nitrogen in the emeraldine form of PANI can be protonated in the presence of strong acidic media and the imine groups are easier to protonate even in mild acidic conditions. The protonation induces a transition from insulator to conductor while maintaining the π-electrons constant in the polymeric backbone.

PANI EB powder can be synthesized using several techniques, including chemical polymerization, electrochemical polymerization, plasma polymerization, and enzyme polymerization. Among these methods, chemical oxidative polymerization is the simplest and most economical procedure to produce PANI in larger quantities (Xu et al. 2018). The high molecular weight PANI EB powder is required to produce the membrane with excellent permeability and mechanical strength. In this study, we have purchased commercially available PANI EB powder (100,000 MW) of average particle size 1.2 nm

and the dynamic light scattering (DLS) analysis result is shown in the Figure 6.1(a). The molecular weight of the PANI can be measured using gel permeation chromatography rather than using a Dynamic Light Scattering machine. Figure 6.1(b) represents the UV-Visible analysis result obtained for the PANI EB powder. A typical PANI EB shows two distinct absorption peaks located between 315-345 nm (polaron-π^* transition of benzenoid ring) and 610-650 nm, which corresponds to the transition from a localized benzene orbital to a quinoid molecular orbital (Shubha et al. 2016; Stejskal et al. 1993).
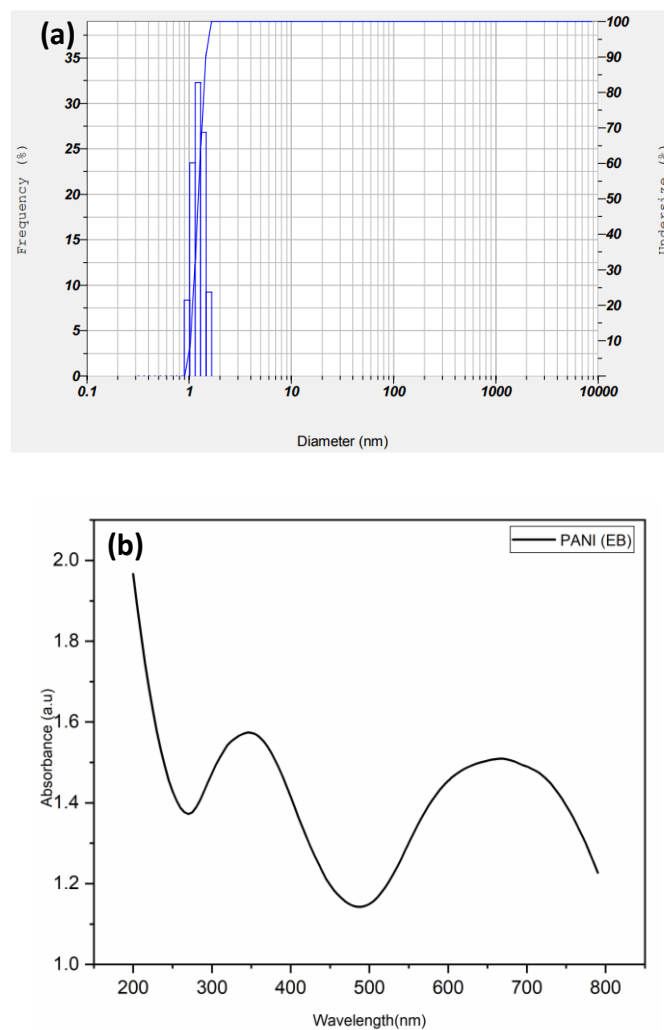
Figure 6.1 (a). Particle size distribution of PANI EB of molecular weight 100,000, (b) UV-Visible absorption spectra for PANI EB powder.

Even though the PANI nanoparticles show better photosensitization and better adsorption of pollutant molecules, the separation of nanoparticles from the reaction mixture after the process is difficult due to higher cost and time consumption. Hence, researchers are

interested in developing polymer composites and the photocatalytic nanoparticle incorporated PANI membranes, which could be an emerging alternative to this.

According to Huang et al., PANI EB powder can be fabricated as a freestanding film and can be utilized for various filtration processes such as reverse osmosis, pervaporation, and gas separation (Huang et al. 1998). The PANI membrane exhibits different permeability and ion selectivity in the undoped and protic acid doped states. Wen and Kocherginsky et al. (1999) have discussed H^+ ion transport and anion transport across the PANI membrane. PANI membranes have been used for organic solvent nanofiltration due to their exceptional chemical stability and higher retention of solute molecules (Wen and Kocherginsky 1999).

An undoped PANI film is more permeable to gases due to void space in the polymer (Tan et al. 2003). The PANI membrane in its undoped emeraldine base (EB) form is fairly hydrophobic when it comes to liquid filtration. At its doped condition, positive charge is induced in the polymer and the negative charge on the counter ions helps to increase the hydrophilicity of the membrane. Doping of the polymer alters the morphological properties of the membrane on the very nano-scale which enhances the diffusion of permeating species.

The major membrane formation techniques include phase inversion, diffusion cell polymerization, electrospinning, radiochemical graft polymerization, etc. Among these, the phase inversion method is the most widely used method to produce films with a PANI content of 15-25 wt% (Xu et al. 2018). The major problem related to the PANI EB dissolution in NMP solvent is the gelation when the EB powder concentration exceeds 6% in the NMP solution due to its intra-intermolecular hydrogen bonding. The relatively high molecular weight (150,000 MW) PANI EB in NMP is stable at room temperature. For viscous PANI-NMP solution, to occur gelation, at least 4 hydrogen bonds were disrupted (Yang and Mattes 2002). The drawbacks like gelation could be overcome by controlling the EB powder loading, secondary amine concentration and maintaining a lower temperature (Yang and Mattes 2002). The secondary amine (4-MP) prevents gelation of PANI EB powder in NMP solution by forming an H-bond between the imine and amine groups (Chapman et al. 2008). The major drawbacks of bare PANI membranes are low flux and mechanical strength, which can be overcome by fabricating integrally skinned asymmetric PANI membranes with a thin top separation layer and a thick porous layer at

the bottom. Conducting PANI is effective in converting Cr(VI) to a less toxic Cr(III) form (Liu et al. 2013a).

In this section, we have optimized the casting of bare PANI membranes by the simplest non-solvent induced phase inversion method for different PANI concentrations (10, 12.5, 15, and 17.5 wt%) at room temperature. The membranes were characterized to study their physical properties, and furthermore, the reduction capacity of the membranes was also investigated.

6.2 MATERIALS

Polyaniline EB powder (100,000 MW), N-methyl pyrrolidone (NMP), 4-methyl piperidine (4-MP) were purchased from Sigma Aldrich. 1,5-diphenyl carbazide (DPC) was procured from Loba Chemie Pvt. Ltd., and potassium dichromate ($K_2Cr_2O_7$) from Fisher. Bovine serum albumin (BSA) was purchased from HiMedia Laboratories, India. Distilled water was used throughout the experiments to prepare solutions.

6.3 METHODS

6.3.1 Membrane preparation

The membranes were prepared by the non-solvent induced phase inversion method. The calculated amount of NMP and a portion of 4-MP were added and stirred in a magnetic stirrer at 500 rpm, and to this mixture, PANI EB (100,000 MW) powder was added using a spatula (as mentioned in table 6.1). After 4 hours of mixing, the viscous melt was then cast on a glass plate using a polished glass rod. The glass plate was kept for air drying and then immersed in a coagulation bath. The membranes were removed and stored in the refrigerator for further use.

Table 6.1 Bare PANI membrane compositions

Membrane (wt%)	PANI (EB) (g)	4-MP (g)	NMP (g)
10	2.5	1.875	20.625
12.5	3.125	1.875	20
15	3.75	1.875	19.375
17.5	4.375	1.875	18.75

6.3.2 Membrane performance studies and characterization

The membrane performance studies using bare PANI membranes were carried out in a custom-made membrane testing cell with a quartz glass window connected to a 2 L feed tank operated at a 0.5 MPa pressure as shown in Figure 6.2.

1.Oxygen cylinder   2.Gauges   3.Feed tank (2L)   4.Valve   5.Visible light (400W)   6.Dead-end filtration set-up
7.Quartz glass window   8.Graduated beaker   9.Protonated PANI membrane and mesh
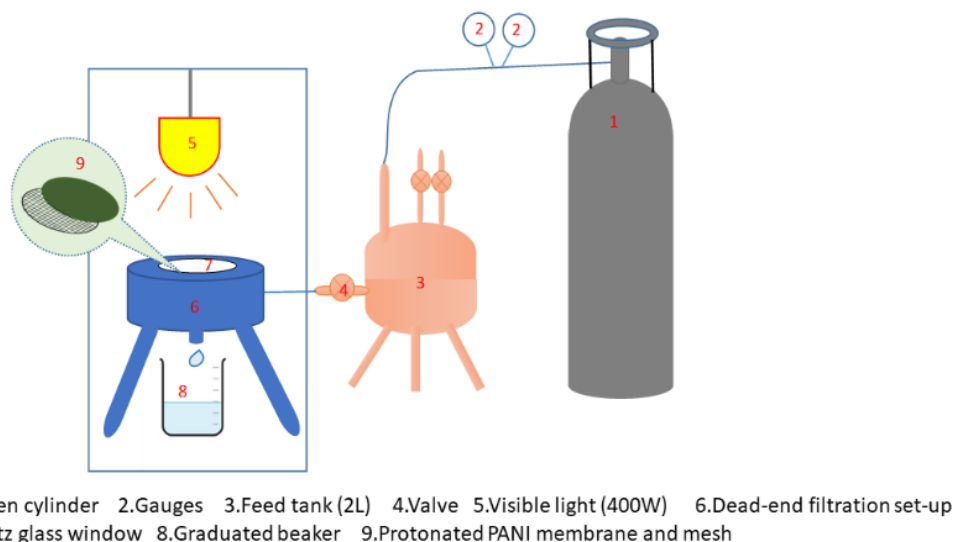
Figure 6.2. Photocatalytic membrane reactor set-up

The effective membrane area is 14.6 cm^2 and the membranes were protonated with HCl before every filtration process.

The pure water flux of the membrane is calculated by the following equation

$$Jw = \frac{V}{(\Delta t.A)} \qquad\qquad \rightarrow (1.0)$$

Where Jw is the flux (L/m^2.h), A is area of the membrane (m^2) and V is the volume (L) of the water collected in time interval, t (h).

6.3.3 Water uptake and porosity of bare PANI membranes

The water uptake and swelling degree calculation was done by dipping 2 cm x 2 cm membrane pieces in deionized water for 24 h and wiped with blotting paper and then the membrane wet weight (Ww) was measured. The membrane pieces were then allowed to dry at 75°C till it reached a constant weight (Wd) in a hot air oven. The swelling degree (%) and porosity (%) was calculated by the equations given below,

$$\text{Water uptake (\%)} = \frac{Ww - Wd}{Ww} * 100 \qquad\qquad \rightarrow (2.0)$$

91

$$\text{Porosity (\%)} = \frac{\frac{(Ww-Wd)}{Dw}}{\frac{Ww-Wd}{Dw}+\left(\frac{Wd}{Dp}\right)} *100 \qquad \rightarrow (3.0)$$

Where Dw is the density of water (0.998 g/cm^3) and Dp is the density of polymer (1.17 g/cm^3) (Etemadi et al. 2017; Li et al. 2017).

6.3.4 Protein rejection

Rejection studies were carried out using BSA as a typical feed solution. Feed solutions with a concentration of 1 g/L of protein are prepared using DI water and filtered through each membrane individually for 120 min. The BSA permeate concentration, which was collected over a 10 min time interval, was then estimated using a UV-Visible spectrophotometer (U-2900 HITACHI) at a wavelength of 277 nm (Bai et al. 2012). The BSA rejection (%R) of the membrane is determined using the following equation,

$$\% R = \left(1 - \left(\frac{Cp}{Cf}\right)\right) *100 \qquad \rightarrow (4.0)$$

Where Cp (g/L) and Cf (g/L) are the BSA concentrations in permeate and feed, respectively.

6.3.5 Antifouling property

The ability of a membrane to resist fouling was determined in terms of flux recovery ratio (FRR) (Nair et al. 2016). After BSA rejection, the membranes were washed thoroughly with DI water and subjected to PWF study once again. The ratio of initial pure water flux to the recovered flux indicates the recycling potential of the membrane. FRR is evaluated using the following equation (where Jw_1 and Jw_2 are PWF before and after BSA rejection, respectively).

$$\% FRR = \left(\frac{Jw2}{Jw1}\right) * 100 \qquad \rightarrow (5.0)$$

6.3.6 Adsorption studies

A circular shaped membrane piece was dipped in a 50 mL Cr(VI) solution having 10 ppm concentration. After the Cr(VI) adsorption, the membranes were cleaned, deprotonated to remove all the Cr(VI) traces from the membrane, and protonated with acid for future use. During the adsorption experiment, 2 mL of sample was collected for a known time interval to check the Cr(VI) concentration up to 7 hours. The adsorption capacity was calculated using the following equation,

$$qe = \frac{(Co-Ce)V}{m} \qquad\qquad \rightarrow (6.0)$$

qe – Adsorption capacity at equilibrium (mg/g)

Co- Initial concentration (mg/L)

Ce – Equilibrium concentration (mg/L)

V- volume of the Cr(VI) solution (mL)

m – Weight of the adsorbent (g).

6.4 RESULT AND DISCUSSION

CHARACTERIZATION OF PANI MEMBRANES

6.4.1 FESEM Analysis for the membranes
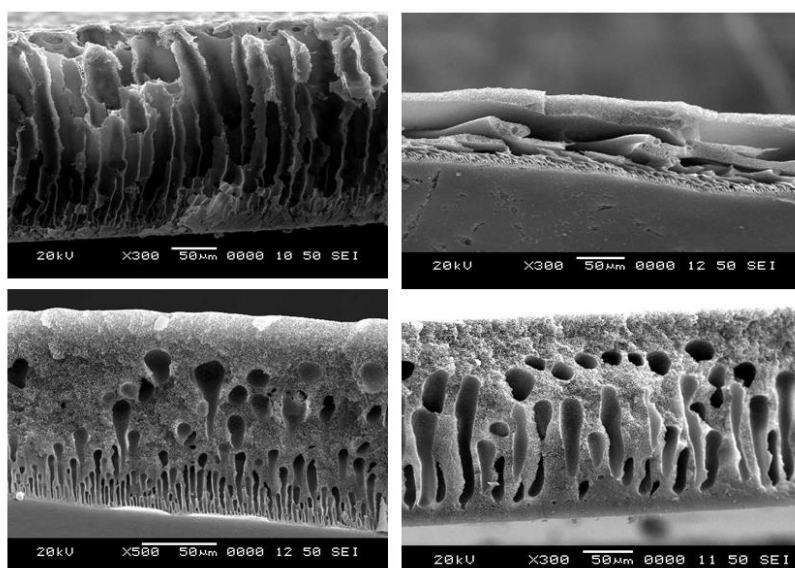
Figure 6.3 SEM images of (a)10wt%, (b)12.5wt%, (c)15wt%, and (d) 17.5wt% pristine PANI membranes

Figure 6.3 shows the SEM images of the prepared membranes. Figure 6.3(a) and (b) shows the incompletely developed asymmetric structure of 10 and 12.5 wt% membranes. The lower PANI EB (size 1.2 nm) concentration in NMP yielded extremely brittle and thin membranes. The instantaneous demixing of solvent- non-solvent might have led to the porous top layer and finger-like substructure (Alhweij et al. 2021). The lack of stability and mechanical strength limits its application in membrane filtration. Figure 6.3(c) shows that the 15 wt% PANI EB content membrane has typical asymmetrical structure with a thin skin

layer on the top and microvoids supporting layer at the bottom. Figure 6.3(d) also has an asymmetrical structure with a dense top layer at the surface. The thicker top layer provides water or solvent transportation resistance during the filtration process. The 15 wt% membrane has a pore diameter of 10 µm, pore size of 50.40 µm long, and the 17.5 wt% had an average pore diameter of 17 µm and a depth of 70 µm. Figure 6.4(a) and (b) represents prepared undoped and doped PANI membrane. Undoped PANI appeared as a smooth, shining surface, and after acid doping, the shine has disappeared. The undoped membranes appear in copper bronze, and the doped films appear in deep blue.
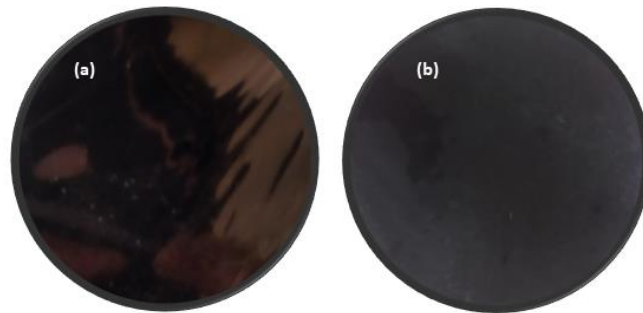
Figure 6.4 (a). Undoped and (b). Doped PANI membrane

6.4.2 Contact angle analysis

Figure 6.5 shows the contact angle of all the membranes synthesized with different weight percentages of PANI. The membranes with lower PANI concentrations showed a rough surface and higher hydrophilicity. The EB membranes of 15 and 17.5 wt% appeared bronze-coloured, and the hydrophilicity obtained for the membranes was 41.12° (10 wt%), 44.76° (12.5 wt%), 76.27° (15 wt%), and 87.55° (17.5 wt%). Even though the 10 and 12.5 wt% membranes showed the lowest contact angle and higher water affinity, they showed poor mechanical properties. Among all the membranes synthesized, 15 wt% membranes showed better hydrophilicity and mechanical strength, which were used for further analysis.
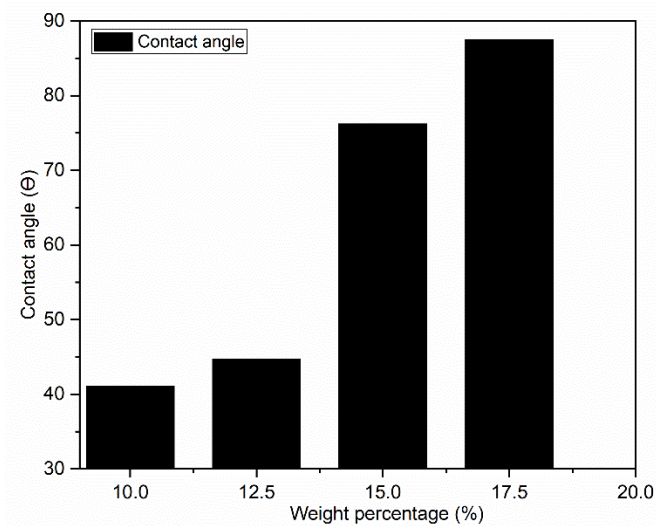
Figure 6.5 Contact angle for prepared 10 wt%, 12.5 wt%, 15 wt%, and 17.5 wt% membranes.

6.4.3 ATR-FTIR analysis
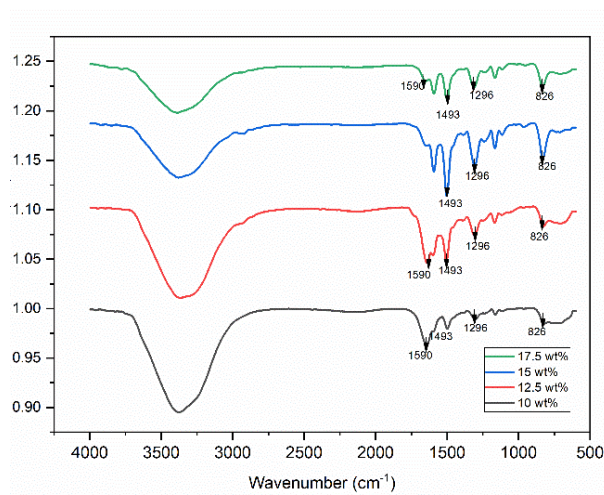
Figure 6.6 ATR-FTIR spectra for undoped 10wt%, 12.5wt%, 15wt%, and 17.5wt% membranes.

Figure 6.6 shows the ATR-FTIR spectra of the prepared membranes at their EB states. The peaks at 1116 cm^{-1} correspond to C-H bending, while 1590 cm^{-1} and 1493 cm^{-1} peaks correspond to the quinoid and benzenoid rings of PANI (Harijan and Chandra 2016). The functional group affects the membrane permeability and Cr(VI) reduction properties.

6.4.4 Pure water flux, protein rejection, and antifouling properties.

The membranes prepared with 10 wt% and 12.5 wt% PANI were mechanically weak and could not withstand the permeation pressures. However, the membrane with 15 wt% PANI showed an asymmetric structure with a top thin skin layer, which helped the membrane to withstand the pressure, and the macrovoids in the bottom layer enabled fluid transport. The permeation properties are also higher for the 15 wt% membrane than for the other compositions.

Doping converts the imine group (=N-) into the amine group (-N.-) (Xu et al. 2018a) of PANI. PANI in the EB form consists of half-amine and half-imine nitrogen groups. On complete doping, imine nitrogen gets protonated. PANI shows poor processibility in its emeraldine salt state. The protonation with formic acid and acetic acid yields improved processability but lower mechanical strength. The doping process helps to remove residual NMP from PANI membranes (Sairam et al. 2006). HCl doping improves the permeability and selectivity of the membranes (Wen and Kocherginsky 1999). The permeability and water uptake profiles obtained for the different bare PANI membrane compositions are shown in Figure 6.7. The porosity and water uptake values for 10 wt% is 80.27% and 80.93%. The rough surface and macrovoid pores enhanced the water uptake ability of the membrane. The 12.5 wt% membrane could yield a porosity and water uptake of 78.31 % and 77.25%, and the 15 wt% membrane yielded 77.25% and 74.38%. Similarly, 17.5 wt% could yield a porosity and water uptake capacity of 75.49 and 72.44%. It was observed that the membranes with lower polymer contents were appeared more hydrophilic than the 15 and 17.5 wt% membranes.
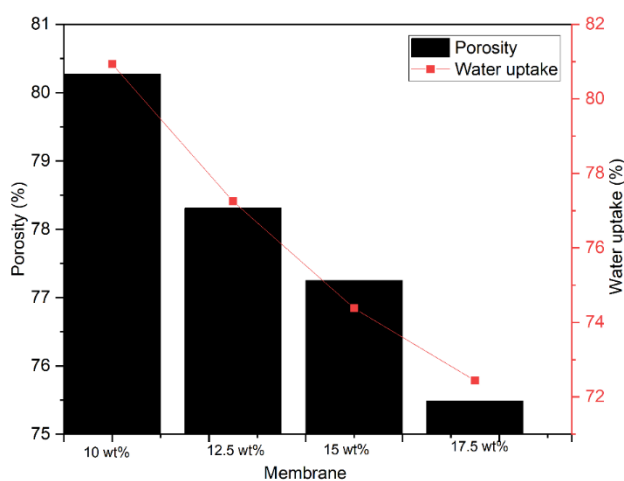
Figure 6.7 Porosity and water uptake study of membranes.

6.5 CHROMIUM (VI) ADSORPTION AND REDUCTION

The doped PANI has been proved to be an excellent sorption material for Cr(VI) removal (Zhang et al. 2010). The filtration study was conducted in the presence of visible light. The permeate Cr(VI) concentration decreased rapidly in the initial hours due to the adsorption and filtration. It was observed that the temperature of the whole set-up increased due to the prolonged exposure of light. It leads to the loosening up of membrane pores, and Cr(VI) in the permeate increases gradually from 90 min. The membrane filtration was performed under dark conditions, and a removal of 51.26 % and 57.60 % was obtained by the 17.5% and 15% membranes (given in Table 6.2). The Cr(VI) concentration in the permeate was first decreased initially due to the adsorption and attain the saturation level. The doped membranes could yield a Cr(VI) removal of 32.26% and 30.20% for 15 and 17.5 wt% membranes, respectively, at 120th min under visible light (in Figure 6.8).

Table 6.2 Adsorption studies

Cr(VI) adsorbed during membrane filtration (With light) (%)			
Undoped		**Doped**	
17.50 (Wt %)	**15 (Wt %)**	**17.50 (Wt %)**	**15 (Wt %)**
18.30 %	21.20 %	30.20 %	32.26 %
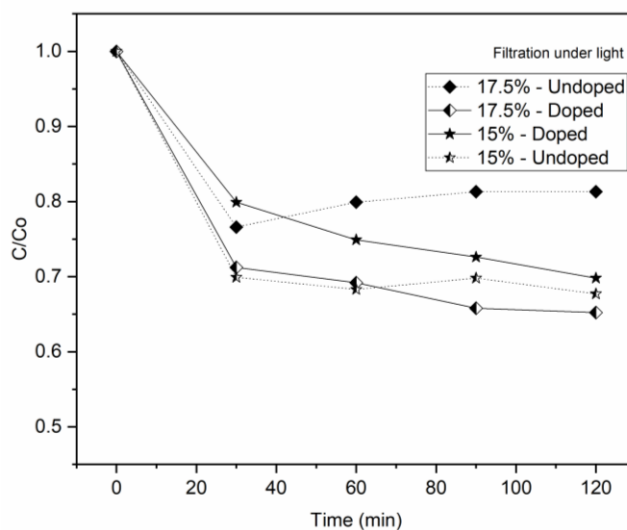
Figure 6.8 Chromium (VI) filtration under visible light

The amines of ES form can perform the role of electron donors for Cr(VI) reduction, chelating, and adsorbing sites for negatively charged Cr(VI) ions in the solutions. The Cr(VI) adsorption on the PANI membrane is higher at lower pH in the doped state (given in table 6.2 and Fig 6.8). At lower pH (pH 2-6.2), Cr(VI) exists as $HCrO_4^-$ or $Cr_2O_7^{2-}$ in aqueous solutions, and the protonated adsorbent membrane will have a positive surface charge due to amine groups. In solution pH higher than 5.5, Cr(VI) exists in CrO_4^{2-} ions. The mechanism of Cr(VI) adsorption on HCl doped PANI membrane occurs by the anion exchange process. The Cl^- anion exchanges with $HCrO_4^-$ ions. The positively charged surface helps to remove metal anions also by electrostatic attraction and reduces Cr(VI) to merely toxic Cr(III) (Karthik and Meenakshi 2014). The membranes became deprotonated as the Cr(VI) reduction occurred in the membrane (at higher concentrations). The undoped membrane shows very little or no reduction of Cr(VI) as the H^+ ions and amine groups are absent. When filtration was performed using undoped membranes in a PMR at dark, the permeate was lacking in the initial pressurized times. But the permeation started due to the transmembrane pressure.

6.6 ADSORPTION ISOTHERMS

To investigate the Cr(VI) adsorption behaviour of the bare PANI membranes, which were dipped in the Cr(VI) solution, the amount of Cr(VI) adsorption was observed using the UV-Visible spectroscopy method. The adsorption process attained equilibrium within 6 h, and the color of the Cr(VI) solution was achromatized. Furthermore, all the experiments were repeated in duplicate for 7 h. The adsorption experiments were conducted by changing the initial concentration (10, 20, and 30 mg/L) and temperature (30, 40, and 50°C).

Circular shaped PANI membrane coupons (0.3425 g, surface area of 14.6 cm^2) were used for the removal of Cr(VI) and it could adsorb and convert ~99 % Cr(VI) at native pH (5.8 pH) within 6 h under the atmospheric conditions. The pH of the solution changes from pH 5.8 to 4.36 after the adsorption. It indicates the presence of Cr(III) due to the reduction of Cr(VI) in the solution.

We could observe that the adsorption at 40°C and 50°C showed almost similar adsorption characteristics, and the temperature had no effect on adsorption. Adsorption will be maximum at a lower (pH<6) concentration of Cr(VI) solution. It has been noticed that the prepared PANI membranes showed faster adsorption for lower concentrated Cr(VI) irrespective of temperature. The same result can be concluded for the membrane separation

of Cr(VI) in a PMR operated under visible light irradiation. Cr(VI) reduction studies were carried out in a custom-made PMR shown in Figure 6.1.

To analyze the adsorption characteristics of a PMR, two-parameter isotherms like Langmuir, Freundlich, and Tempkin and three parameter isotherms such as Jovanovic multilayer isotherms were employed using the adsorption data.

TWO PARAMETER ISOTHERMS

6.6.1 Langmuir Isotherm

The non-linear form of Langmuir isotherm is given by,

$$\frac{Ce}{qe} = \frac{1}{qm.Ke} + \frac{Ce}{qm} \qquad \rightarrow (7.0)$$

Ce – Concentration of adsorbate at equilibrium (mg/g)

Ke – Langmuir constant (mg/g)

qm – Maximum adsorption capacity (mg/g)

6.6.2 Freundlich Isotherm

The non-linear form of Freundlich equation is given by,

$$qe = Kf.Ce^{\frac{1}{n}} \qquad \rightarrow (8.0)$$

q_e - Equilibrium sorption capacity (mg/g)

K_f , n– Freundlich constant (L/mg)

Ce – Residual equilibrium concentration (mg/L)

6.6.3 Temkin Isotherm

The non-linear equation for Tempkin isotherm is given by,

$$qe = \left(\frac{RT}{b}\right) * \ln(Kt.Ce) \qquad \rightarrow (9.0)$$

b- Tempkin constant related to heat of sorption (J/mol)

Kt- Tempkin constant (L/g)

R – Universal gas constant (8.314 J/mol.K)

T- Temperature at 298 K

THREE PARAMETER ISOTHERMS

6.6.4 Jovanovic multilayer Isotherm

The non-linear equation for Jovanovic multilayer isotherm is given by,

$$qe = qm\ (1 - e^{Kj.Ce}) \qquad\qquad \rightarrow (10.0)$$

q_e - Equilibrium sorption capacity (mg/g)

q_m – Maximum sorption capacity (mg/g)

K_J– Jovanovic isotherm constant (L/mg)

Ce – Residual equilibrium concentration (mg/L)

6.7 SORPTION STUDIES

The equilibrium adsorption isotherm modelling was evaluated using CAVS software. The isotherms like Freundlich, Langmuir, Temkin, and Jovanovic multilayer are presented in the Figure 6.9. The isotherm values obtained for the different isotherms are tabulated in Table 6.3. The correlation coefficients (R^2) are in the order of Jovanovic multilayer > Freundlich > Langmuir > Temkin. This results emphasis the fact that the Jovanovic multilayer and Freundlich adsorption isotherms are convenient to explain the adsorption of Cr(VI) on the flat sheet PANI membrane. The PANI membrane-Cr(VI) system follows a heterogenous adsorption process. This can be due to the higher surface area available for the adsorption. According to the assumptions for Freundlich adsorption, the Cr(VI) metal uptake occurs on a heterogeneous surface by multilayer adsorption with the lateral interaction between adsorbed species on the surface of the adsorbent (Babel and Kurniawan 2004).
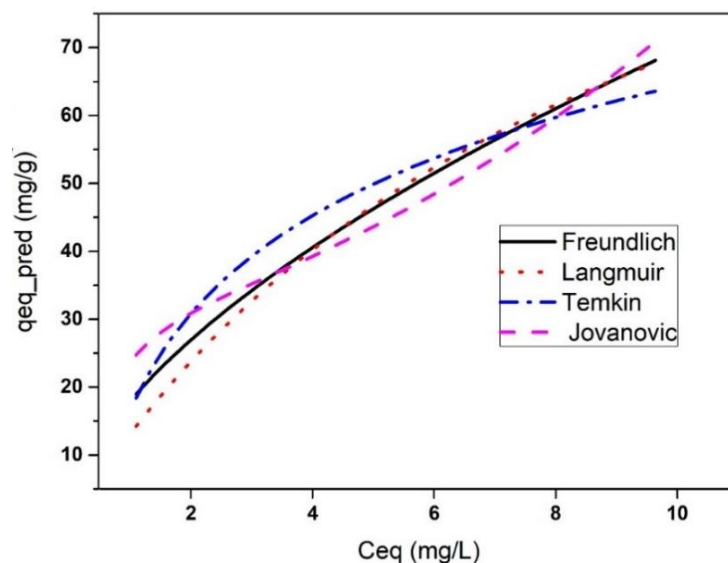
Figure 6.9 Isotherm fit curves

Table 6.3 Isotherm constants

Freundlich	Langmuir	Temkin	Jovanovic multilayer
K_{fr} (L/mg) - 17.909 n_{fr} (dimensionless) - 1.6959	Q_l (mg/g) - 131.36 K_l (L/mg) - 0.1103	b_t (J/mg) - 116.947 K_t (L/mg) - 2.1930	Q_j (mg/g) - 25.845 K_j (L/mg) - 1.740 KK_j (L/mg) - 0.1047
$R^2 = 0.944835$	$R^2 = 0.902891$	$R^2 = 0.847922$	$R^2 = 0.956247$

The isotherm studies revealed that the adsorption of Cr(VI) ions occurs either physically or chemically on the multilayer heterogeneous adsorption sites of the PANI membrane. The adsorption isotherm fits Freundlich and Jovanovic's multilayer adsorption isotherm equations. Freundlich and Jovanovic adsorption isotherms indicates favourable multilayer chemisorption and the reduction of Cr(VI) occurs on the membrane surface (Prajapati and Mondal 2021); (Wang et al. 2021). The n_{fr} value of Freundlich adsorption is around 1.6959, which indicates that the PANI membrane is capable of eliminating Cr(VI) from the aquatic environment. Jovanovic multilayer isotherm results indicate functional groups that favours the adsorption. The Tempkin model is derived from the assumption that the heat of adsorption decreases with the increase in adsorption amount (Wang et al. 2021). The positive value of b_t represents an exothermic process. The magnitude of adsorption depends

on the nature of the adsorbent, the concentration of the Cr(VI) solution, and temperature. A Tempkin parameter value of 34.145 K.cal/mol (i.e., between 20-50 K.cal/mol), and a higher value indicates the occurrence of chemisorption on the membrane surface.

The next chapter discusses the simultaneous photocatalytic reduction and membrane separation in a PMR, where the adsorption will be the slowest step, and hence it is the rate limiting step due to high operating pressure. So, the initial step of pressurisation of membranes till 30 min after dark (which allows adsorption) can be avoided in a PMR.

CHAPTER 7

FABRICATION OF VISIBLE-LIGHT ASSISTED TiO₂-WO₃-PANI MEMBRANE FOR EFFECTIVE REDUCTION OF CHROMIUM (VI) IN PHOTOCATALYTIC MEMBRANE REACTOR

7.1 INTRODUCTION

Heavy metals are renowned as the most dangerous pollutants to human health. The remediation of Chromium (VI) has gained the attention of authorities and the scientific community. Numerous methods have been employed to remove Cr(VI) which includes adsorption, ion exchange, chemical precipitation, membrane separation, electrochemical treatment, biological treatment, and photocatalysis (Fang et al. 2018; Jeffrey et al. 2014; Joshi and Shrivastava 2011; Mnif et al. 2017; Peng et al. 2019),(Li et al. 2018c). The above-listed techniques possess challenges such as high operating costs, generation of secondary pollutants (Arif et al. 2020; Mukherjee et al. 2015; Yong Ng et al. 2013), requirement of additional reagents, and formation of large amounts of sludge (Khulbe and Matsuura 2018).

Membrane separation has been widely used for the removal of inorganic pollutants in wastewater since 1960. Among membrane separations, mixed matrix membranes (MMM) have gained more importance in the past few years. The composite membranes will have enhanced properties like higher adsorption capacity, high rejection, and high permeate flux, because of the synergistic effect of polymers and inorganic additives (Arif et al. 2020; Mukherjee et al. 2015; Yong Ng et al. 2013). Among TiO₂ based MMMs, the heterojunction between TiO₂ and WO₃ can significantly yield better separation efficiency of charge carriers to be used in a photocatalytic membrane reactor (Zhao et al. 2021).

The introduction of conducting polymers (CPs) in environmental remediation has acquired significant recognition in these days (Sahu et al. 2019). The properties such as low cost, easier synthesis, suitable molecular weight cut-off (MWCO), unique doping - de-doping mechanism, easier casting capacities, tunable range of filtration, chelating, robust structure,

environmental- mechanical-chemical stability have made the CP such as PANI (an organic metal) more inevitable material (Karthik and Meenakshi 2015; Liu et al. 2019; Monjezi et al. 2018; Rohani et al. 2017a; Rosaih Rohani, Izzati Izni Yosoff 2018; Sahu et al. 2019),(Li et al. 2018c).

PANI can be tuned with various protic acids (HCl, HNO$_3$, H$_2$SO$_4$) to make it conductive, and it can be easily used to form freestanding films (Rohani et al. 2017a; Zhang et al. 2010). Undoped PANI films are utilized in gas separation and sensing applications due to their void space in the polymer matrix. PANI membranes in their doped state are more permeable to water and solvents (Sairam et al. 2006). PANI can separate mixtures of liquids (pervaporation) as a result of the hydrophobic and hydrophilic characteristics of the undoped and doped films (Tan et al. 2003). Doping helps the formation of the ES form of PANI, and the amine and imine functional groups created by this can chelate the metal ions, which helps the removal of Chromium (Bozkir et al. 2012; Macdiarmid et al. 1987),(Ding et al. 2018; Qiu et al. 2015). Few researchers have used the particulate form of PANI for the removal of heavy metals, but it has limitations like regeneration and recycling of PANI (Tan et al. 2003). The major drawbacks of the PANI membrane are its low solubility and poor mechanical strength due to the rigid-rod macro-molecular chains (Rohani et al. 2017a; Yue et al. 2017; Yusoff et al. 2019). These drawbacks can be overcome by fabricating composite membranes to improve mechanical strength as well as filtration performance.

In this work, TiO$_2$-WO$_3$ (40:1) nanoparticles were hydrothermally prepared and embedded in a Polyaniline (PANI) membrane with varying concentrations (3-7 wt%) and used in a photocatalytic membrane reactor for the removal of Cr(VI) from the aqueous solutions. 4-methyl piperidine (4-MP) was used as a gel inhibiting agent in N-methyl-2-pyrrolidone (NMP) solvent to prepare PANI-based flat-sheet membranes by the phase inversion method.

7.2 MATERIALS

Polyaniline EB (MW=100,000), 4-methyl piperidine (4-MP), N-methyl pyrrolidone (NMP), titanium isopropoxide (TTIP, 97%), and 1,5-diphenylcarbazide (DPC) were procured from Sigma Aldrich. Sodium tungstate dihydrate and acetic acid glacial (99-100%) were purchased from Emplura, India. Ethanol (99%) and potassium dichromate was procured from Fisher. Distilled water was used to make solutions throughout the experiment. All the chemicals were used as such without any purification.

7.3 METHODS

7.3.1 Membrane Preparation

The membranes were prepared using PANI emeraldine base (EB) powder (MW=100,000) dispersed in NMP solution, and 4-MP was added to arrest the gelation of PANI (15 wt%). After 30 min, the nanoparticles (TiO_2-WO_3 (40:1) of an average size of 12.61 nm were added using a spatula by giving enough mixing time to dissolve the PANI powder in the solvent to get a homogeneous solution. The casting solution was bath-sonicated for 25 min to ensure the proper incorporation of nanoparticles in the polymer solution. The mixture was stirred for 4 h at a stirring speed of 500 rpm to get a dispersion of PANI in NMP. The bare PANI membrane was prepared without adding the nanoparticles. The viscous solution was then cast over a glass plate using a finely polished glass rod. The membrane thickness was maintained at 220 µm. The glass plate was allowed to air dry for 30 s and then immersed into the coagulation bath containing deionised water for phase inversion. The entire process is shown in Figure 7.1, and a similar procedure was followed to prepare membranes with different amounts of nanomaterials. The membranes were immersed in a deionized water bath for 24 h for the complete precipitation of the membrane by removing residual solvent and then stored in the refrigerator for further use. The prepared membranes were designated as bare PANI, 3 wt% PANI, 5 wt% PANI, and 7 wt% PANI respectively.
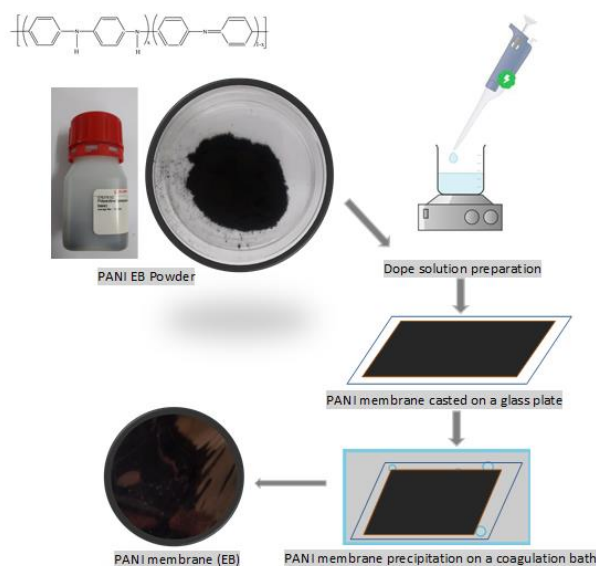
Figure 7.1 Schematic diagram for PANI membrane preparation

7.4 MEMBRANE FILTRATION

Using the prepared NF membrane, separation studies were carried out in a stainless-steel dead-end filtration cell (HP 4750, Sterlitech, USA) of 300 mL capacity and was connected to an oxygen gas cylinder and a feed tank (2 L). The transmembrane pressure (TMP) and feed flow were adjusted using valves (filtration setup is shown in Figure 7.2). The permeate was collected at every known time interval.

1. Oxygen cylinder   2. Gauges 3. Feed tank 4. Valve 5. Dead-end filtration unit
6. Membrane and mesh 7. Graduated beaker
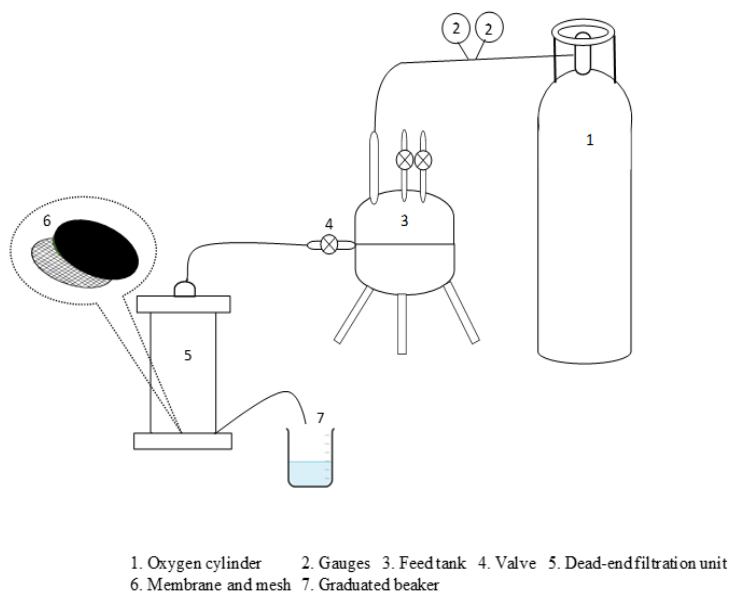
Figure 7.2 Experimental setup for membrane filtration

7.5 CHARACTERIZATION OF PANI MEMBRANES

Synthesized TiO_2-WO_3–PANI membranes were observed under a field emission scanning electron microscope (FESEM). All the samples were analysed after gold sputtering. A transmission electron microscope (TEM, JEOL JEM-2100) was used to analyse the TiO_2-WO_3 samples. X-ray diffractometer (Rigaku Miniflux 6000) equipped with monochromatized high-intensity Cu Kα radiation (λ = 1.541A°) was used to analyse the crystalline nature of the samples. The conductivity was measured using an inductance, conductance, and resistance meter (LCR) (HIOKI, Japan). The membrane and catalysts were subjected to Fourier transform infrared (FTIR) spectroscopy for analysing the functional groups. A UV–Visible spectrometer (Hitachi, U-2900) was used to analyse the Chromium (VI) concentration in the sample at a wavelength of 540 nm.

7.6 PERFORMANCE ANALYSIS OF MEMBRANES

7.6.1 Contact angle analysis, water uptake, and porosity

The contact angle measurement was carried out by the video-based sessile droplet method using the Kruss DSA 100 analyser. The membrane samples were glued onto a glass plate for analysis, and water droplets were allowed to adsorb in an average of three different places, and the contact angles were measured. The droplet volume was maintained constant at 4 μL throughout the experiments. Water uptake and porosity of the membranes were analysed gravimetrically. The percentage water uptake was calculated using the following equation,

$$\% \text{ Water uptake} = \frac{(Ww - Wd)}{Ww} * 100 \qquad \rightarrow (1.0)$$

The wet samples of a 2 cm x 2 cm sized membrane were wiped with blotting paper and the wet weight (Ww) was noted. The membrane was then placed in a hot air oven for 48 h at 75°C and dry weights were noted (Wd).

7.6.2 Pure water flux (PWF) of the membrane

The experiments to determine the pure water flux (PWF) of the membranes were carried out in an experimental setup discussed in section 7.4. Circular-shaped membrane samples with an effective surface area of 14.6 cm^2 were immersed in water and protonated using HCl before the start of every experiment. The time-dependent PWF was determined by collecting the permeate after achieving a transmembrane pressure of 0.5 MPa for 20 min, and then the permeate was collected at every 10 min intervals. The pure water flux (L/m^2.h) was calculated using the following equation,

$$Jw_1 = \frac{Q}{t.A} \qquad \rightarrow (2.0)$$

Where Jw_1 is water flux across the membrane in L/m^2.h, Q is the amount of permeate collected (L), A is the effective membrane area (m^2), and t is the time duration at which permeate was collected (h).

7.6.3 Chromium (VI) removal using TiO$_2$-WO$_3$ incorporated polyaniline membranes

Cr(VI) removal using the synthesised composite membrane was performed in a dead-end filtration cell under a constant transmembrane pressure of 0.5 MPa. The filtration was carried out for a period of two and half-hour with an initial Cr(VI) concentration of 10 ppm and at its native pH. After filtration, the permeate samples were analysed by the 1,5-

diphenylcarbazide (DPC) colorimetric method at 540 nm wavelength. The remaining concentration of Chromium was expressed by the following equation,

$$Cr(VI) \text{ remaining} = C/C_o \qquad\qquad \rightarrow (3.0)$$

Where C_o is the initial concentration of Cr(VI) and C is the concentration of Cr(VI) at time (t).

The experiments for Chromium (VI) reduction were carried out in four consecutive reduction cycles in a dead-end filtration cell to analyse the reduction capacity and reusability of the synthesised membrane.

7.6.4 Photocatalytic activity of the TiO$_2$-WO$_3$/PANI composite membrane

Photocatalytic activity of TiO$_2$-WO$_3$–PANI membranes was evaluated in batch mode using 5 wt % PANI membrane under dark and also under visible light in a dead-end membrane filtration testing cell with a quartz window on the top. Experiments were performed using 10 ppm Cr(VI) solution at its native pH, at an operating pressure of 0.5 MPa, at room temperature and the filtration cell was irradiated with a 400 W visible lamp (2600 Lux). The membrane was protonated using protonic acid before loading it in the filtration cell. The experiment was performed for 120 min, beyond which significant changes were not observed. The permeate was collected for every 30 min time interval, and the Cr(VI) concentration was analysed through the DPC colorimetric method. The remaining Chromium (VI) concentration was calculated using the equation (3.0).

7.7 RESULTS AND DISCUSSION

7.7.1 Morphological analysis of the membranes

Figure 7.3 shows the cross-sectional FESEM images of the developed PANI-based membranes. Figure 7.3 shows that the loading of nanoparticles did not alter the asymmetric structure of the membrane. The macrovoids present in the membranes are the result of the high exchange of solvents during the phase inversion process. The addition of nanoparticles did not show any aggregation or clogging of pores in the membrane structure, which indicates better compatibility of NPs with the membrane material. The FESEM image of bare PANI membrane (Figure 7.3(a)) shows an asymmetric structure with a dense top layer, a finger-like sub-layer, and a sponge region (Tao et al. 2018). Using 5 wt% and 7 wt% nanoparticles, we could obtain a typical asymmetric structure without the formation of a

sponge region. The morphological differences were due to the change in the precipitation rate during the phase inversion process (Idris et al. 2017; Strathmann and Kock 1977).
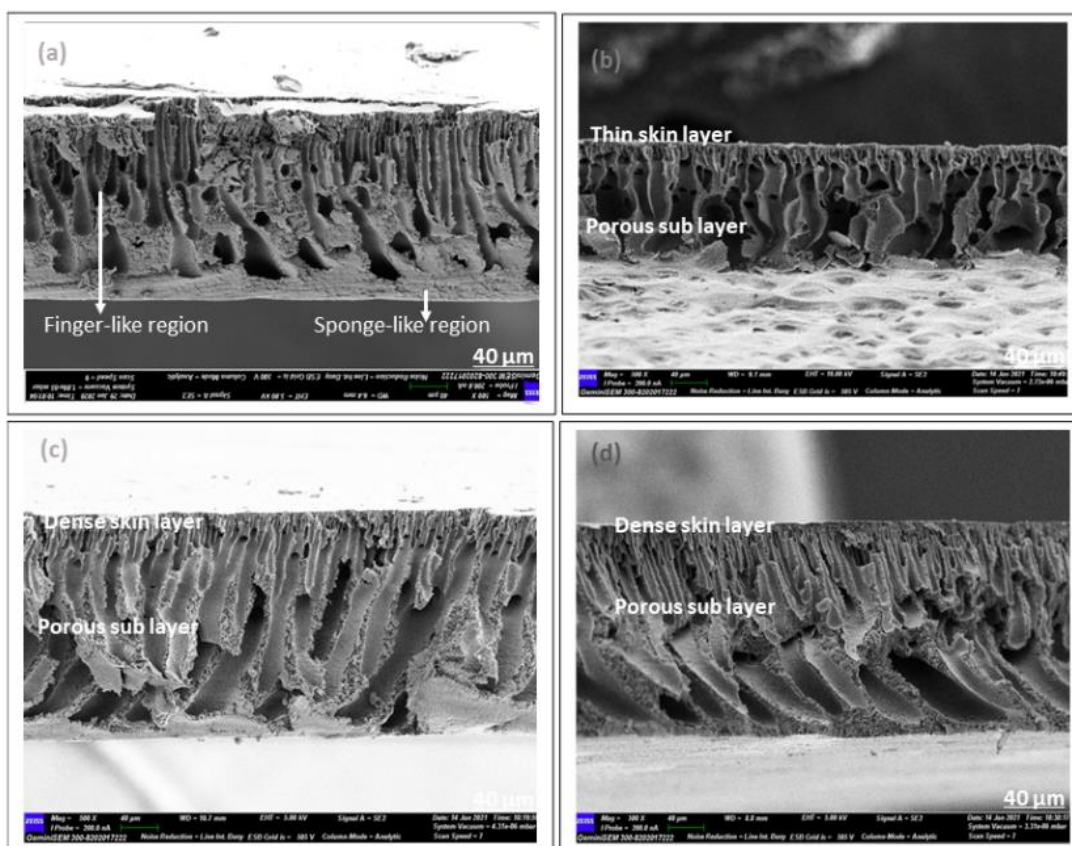
Figure 7.3 SEM images of (a). bare PANI membrane, (b). 3 wt%, (c).5 wt% and (d). 7 wt% PANI composite membrane

Theoretically, fast precipitation produces a membrane with a thin skin and fine finger-like macrovoids, whereas slow precipitation produces sponge-like pores. From the figure, it can be observed that the thickness of the top layer varies with an increase in nanoparticle loading. In the 5wt% PANI membrane (Figure 7.3(c)), we could observe a dense top layer with large macropores in the sub-layer, similar to the tortuous path. In the 7 wt% PANI membrane (Figure 7.3(d)), the thickness of the top layer is more, and finger-like microvoids were also observed. The membrane with a sponge-like morphology will have low permeability, while a finger-like morphology offers higher permeability and more resistance during filtration. The higher viscosity makes the 7 wt% PANI membranes thicker and denser compared to 3 wt% and bare PANI membranes (Choudhury et al. 2018). In the 3 wt% membrane, the thin top layer and poorly developed macrovoids were formed due to

the instantaneous demixing. Thus, membrane thickness varies with nanoparticle addition despite the same casting height. The loading of 7 wt% nanoparticles caused the formation of thicker membranes with large finger-like macro voids due to the lessened thermodynamic instability and more water-solvent exchange channels (Duong et al. 2018). The 3 wt% and 5 wt% membranes showed an excellent smooth surface like the bare PANI membrane, which indicates the proper dispersion of nanoparticles in the membrane matrix.

7.7.2 ATR-FTIR Spectroscopic analysis of membranes
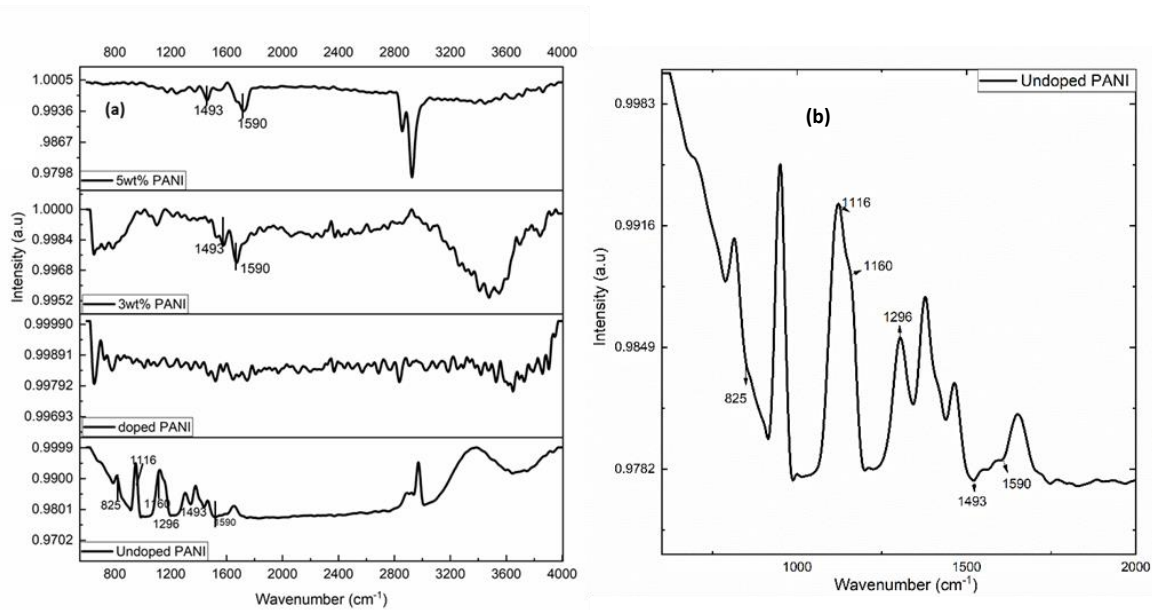
Figure 7.4 (a) FTIR spectra for undoped bare PANI membrane, doped bare PANI membrane, 3wt% membrane and 5wt% membrane (b) Enlarged portion of FTIR spectra obtained for undoped PANI membrane

Figure 7.4 shows the ATR- FTIR spectra of all the membranes. The peaks at 1590 cm^{-1} and 1493 cm^{-1} correspond to the C-C stretching of quinoid and benzenoid rings. The peak at 1296 cm^{-1} is attributed to the C-N and C=N stretching of PANI, the peak at 1116 cm^{-1} corresponds to in-plane C-H bending, and the peak at 825 cm^{-1} attributes to the out-plane C-H bending (Harijan and Chandra 2016; Khan et al. 2015; Liu et al. 2019; Yusoff et al. 2019). MacDiarmid et al. recognised a band around 1160 cm^{-1}, which corresponds to the degree of delocalization and which is considered the peak of conductivity. The characteristic bands at 790-600 cm^{-1} (Pakdel Mojdehi et al. 2019) can be attributed to PANI-TiO$_2$ (WO$_3$) nanocomposite. The functional groups of the membrane generally affect the membrane properties. In particular, functional groups in the pore wall and on the surface

of the membrane affect the rejection of the solute. According to the Donnan exclusion principle, ion transport depends on the surface charges (Muthumareeswaran et al. 2017). These observations demonstrate the presence of PANI and TiO_2-WO_3 in the composite membranes.

7.7.3 XRD patterns for membranes
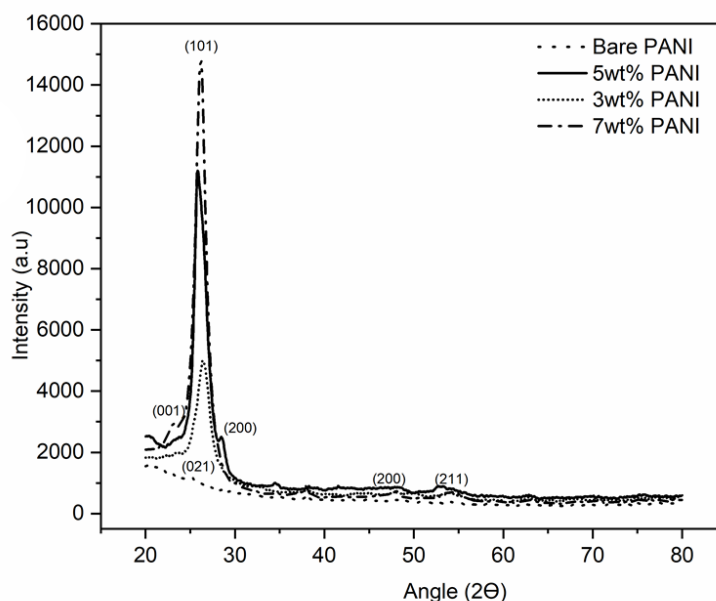
Figure 7.5 XRD patterns for bare PANI membrane, 3 wt%, 5 wt% and 7 wt% PANI composite membrane respectively

Figure 7.5 shows the XRD patterns of the prepared membranes. The peaks at $25.28°$ and $48.05°$ correspond to TiO_2 tetragonal anatase planes of (101) and (200) (ICDD 00-021-1272). The peaks observed in Figure 7.5 show the XRD patterns obtained for the membranes. The peaks at $25.28°$ and $48.05°$ correspond to TiO_2 tetragonal anatase planes of (101) and (200) (ICDD 00-021-1272). The peaks observed at $22.7°$ and $28.12°$ correspond to the (001) and (200) planes of the hexagonal structure of WO_3 (ICDD 00-033-1387). The bare PANI membrane consists of a monoclinic structure and a peak observed at $25.28°$ corresponds to the plane (021) (COD 96-715-1387). The intensity of the XRD spectra increased as the nanoparticle concentration in the membrane increased. In the 7 wt% membrane, the highest intensity at $22.7°$ was observed, which corresponds to WO_3. Further, it has been observed that the thickness of 3 wt% membrane is slightly less compared to 7 wt% membrane, which could be due to the increase in the viscosity of the

cast solution, which would have slightly increased the thickness of the different layers in the membrane. Bare PANI membranes were partially in crystalline form and, on doping the membranes with nanoparticles, they have become crystalline, whereas the amorphous films remain amorphous (Zheng et al. 1997).

7.7.4 Conductivity analysis of membranes

Table 7.1 Conductivity for bare PANI membrane, 3wt%, 5wt% and 7wt% PANI composite membrane respectively

Membrane	Conductivity (S/cm)
Bare PANI membrane	8.82×10^{-4}
3 wt% Membrane	1.43×10^{-4}
5 wt% Membrane	8.107×10^{-4}
7 wt% Membrane	12.203×10^{-4}

The conductivity of the prepared membrane did not follow either an increasing or decreasing order (shown in Figure 7.6 and Table 7.1). The conductivity of 3 wt% and 5 wt% membrane is low compared to bare PANI membrane, which could be due to the hydrolysis of the membrane, which breaks the polymeric chain at -N=C bond (Kumar et al. 2018). The higher protonation with HCl dopant leads to higher conductivity. The membrane thickness also showed a significant effect on conductivity. The 7wt% PANI membrane is thick and during protonation, conductivity is also boosted. The conductivity of these PANI membranes was discovered to be in the semiconducting range (Alam et al. 2013).
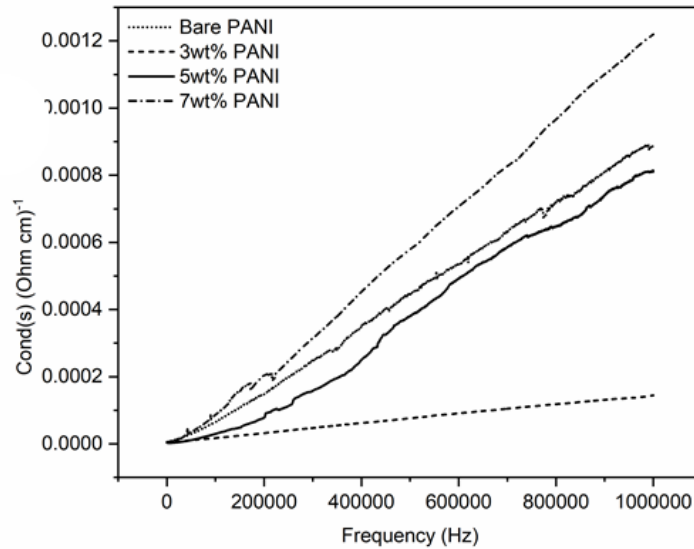
Figure 7.6 Conductivity for bare PANI membrane, 3 wt%, 5 wt% and 7 wt% PANI composite membrane respectively.

7.8 PERFORMANCE ANALYSIS OF MEMBRANES

7.8.1 Contact angle analysis, water uptake, and porosity

The sorption properties of the prepared PANI membrane depend on the hydrophilicity of the membrane. The hydrophilicity of the membranes can be evaluated using the contact angle of the membrane (Fryczkowska et al. 2017). The contact angle of the bare PANI membrane was found to be (from Figure 7.7) 78° at 60th second and blending of nanoparticles in the PANI has reduced the contact angle as follows, 72° for 3 wt% blending, 48° for 5 wt% blending and 71° for 7 wt% blending. The 5 wt% membrane showed the lowest contact angle, which indicates that the membrane has high porosity compared to other membranes. Higher hydrophilicity is due to the existence of amine and hydroxyl hydrophilic functional groups on the membrane surface. The non-uniform dispersion, cluster formation, and agglomeration of nanoparticles might have affected the contact angle values of other samples (Etemadi et al. 2017; Moradi et al. 2020).

The water uptake value of the membranes quantifies the pore volume of the membrane. The water uptake values of different membranes are as follows; 74.38 % for bare PANI, 76.43 % for 3 wt%, 80.96 % for 5 wt%, and 71.76 % for 7 wt% (Pereira et al. 2015). The increasing trend of water uptake starting from 5 wt% could be due to the increase in the viscosity of the casting solution and thereby accelerating the demixing of the solvents during the phase inversion process, which has led to more finger-like pores (Moradi et al.

2020). In the 7 wt% sample, the water uptake value is less due to the agglomeration of nanoparticles.
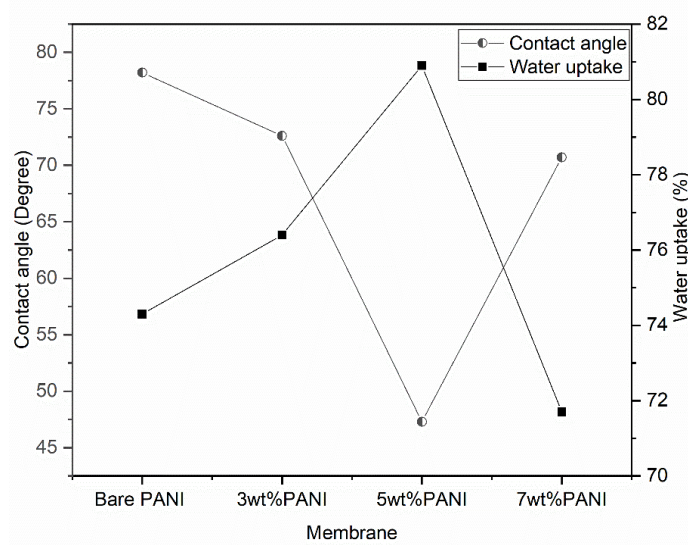
Figure 7.7 Contact angle and water up-take for PANI membrane, 3wt%, 5wt% and 7wt% PANI composite membranes, respectively.

7.8.2 Pure water flux (PWF) of the membrane

The membrane permeability was investigated by measuring the pure water flux in a membrane filtration testing cell. The pure water flux obtained at 120 min (shown in Figure 7.8) using all the synthesised membranes is as follows; 45.317 L/m^2.h for bare PANI, 60.422 L/m^2.h for 3 wt %, 143.5 L/m^2.h for 5 wt% and 37.76 L/m^2.h for 7 wt% membrane. The membranes with 5 wt% loading showed the highest pure water flux compared to other membrane samples, and those with 7 wt% showed the lowest value. This could be due to the hydrophilicity and porosity of the membrane. Nanoparticle addition has increased the number of pores by eliminating sponge-like regions in the bottom of the membrane, and the addition of 7 wt% of nanoparticles might have affected the density and hydrophobicity of the membrane. The water uptake and permeability values were low for the 7 wt% membrane due to its denser top layer. A higher concentration of nanoparticles above the optimal value results in poor membrane performance due to nanoparticle aggregation (Wen et al. 2019).
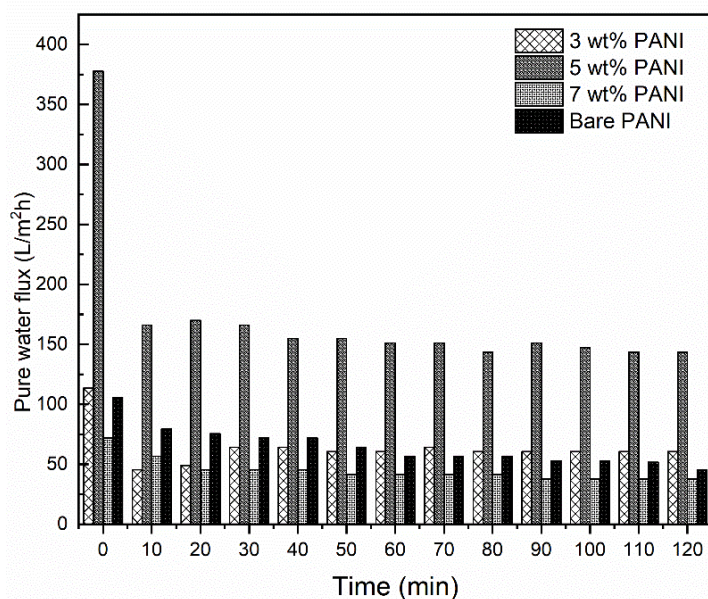
Figure 7.8 Pure water flux for bare PANI membrane, 3 wt%, 5 wt%, and 7 wt% PANI composite membranes, respectively.

7.8.3 Chromium (VI) removal using TiO$_2$-WO$_3$ incorporated Polyaniline membranes

The fabricated membranes were tested in a dead-end filtration cell for Chromium (VI) removal in batch mode. The schematic diagram of the setup for Cr(VI) filtration using TiO$_2$-WO$_3$ incorporated nanofiltration membranes is shown in Figure 7.2. 10-ppm Chromium (VI) solution at its native pH (pH -5.80) was used for the reduction studies with different membranes (bare PANI, 3 wt% PANI, 5 wt% PANI, and 7 wt% PANI). As the pH of the native Chromium solution is less than 6.5, Cr(VI) majorly exists as HCrO$_4^-$ and Cr$_2$O$_7^{2-}$ (Jahan et al. 2018). The PANI in its protonated form consists of amines and imines, and the anionic species of Cr(VI) ions will be attracted towards the positively charged membranes (Li et al. 2020). The membrane separation and Cr(VI) removal occur in three major steps, adsorption of Cr(VI), reduction of Cr(VI) to Cr(III) and desorption of Cr(III). PANI has a reactive -NH- group in the polymer chain which imparts a very strong chemical flexibility and hence undergoes protonation and deprotonation through nitrogen-containing amine and imine groups in its polymer backbone (Eisazadeh 2007). Due to the high operating pressure, the adsorption will be the slowest step in the membrane separation process. In this study, within 60 min of separation, 98.50% reduction was observed and Cr(VI) was absent in the permeate. From this, we can conclude that Cr(VI) is converted to Cr(III) on the membrane surface and leaves the reaction interface quickly (Deng et al. 2019).

115

Membrane performance was assessed under both dark and visible light, which is shown in Figure 7.9. Under dark conditions, the capacity of the membrane to adsorb Chromium was assessed, and similarly, under visible light, the capacity of the membrane to adsorb and reduce Chromium was assessed. Under the dark conditions, Chromium adsorption was very fast and we were able to observe 55% Chromium removal. Under visible light conditions, a maximum of 67.32% Chromium removal was observed. From this, we were able to conclude that nanoparticle incorporated membranes under visible light can adsorb Chromium (VI) and further reduce it to Chromium (III) through photocatalytic reduction. This proves that the composite membrane can eliminate Chromium (VI) through adsorption, filtration, and photocatalytic reduction. The membranes were tested for the adsorption of Chromium under dark conditions. A reduction of 55 % was observed in the initial stage, and then a constant value was observed, which shows that the adsorption is the fastest step rather than reduction. The membranes were used for filtration under visible light. The reaction was faster under visible light, and a 67.32 % reduction of Cr(VI) was observed.

In general, at lower pH (i.e. <7), Chromium (III) can be easily desorbed from the adsorbed PANI membrane. During the reduction studies, the pH of the solution reduced from 5.89 to 3.70 and this is an indication that the reduced Chromium (III) has desorbed and is present in the final solution. Further, it has been observed that the 3 wt% PANI membrane is mechanically weak and brittle on exposure to the Chromium solution when compared to other membranes. The 7 wt% membranes had more mechanical strength and surface roughness, but it took time to protonate them in the presence of protic acid. Even though the removal of Cr(VI) was slightly high in 7 wt% membranes, the Cr(VI) removal flux was very less in comparison with other membranes. The 5 wt% membranes showed higher flux, higher removal percentage and higher hydrophilicity during Cr(VI) reduction.

At lower pH (1-6), the membrane surface favours Cr(VI) adsorption due to electrostatic attraction between iminium ions and oxyanions. The emeraldine salt form of PANI gets oxidized to convert to the pernigraniline form of PANI (Samani et al. 2016),(Dognani et al. 2019). The shrinkage of the membrane in Cr(VI) solution was observed due to the super oxidation and led to the lowering of crystallinity, shrinkage of pores, and flux reduction. According to Dognani et al., the morphological change of a membrane will not affect the integrity of the membrane. Polyaniline is a highly effective material for the removal of Cr(VI) due to its reductive adsorption nature. PANI provides electrons for the reduction of

Cr(VI) to Cr(III) and also provides an active site to adsorb Cr(III) (Harijan and Chandra 2016), (Li et al. 2020). In the reusability studies, 98.50 % reduction was observed in the first rejection cycle, and the efficiency remained the same even after 4 cycles (in Figure 7.10(d)).

7.8.4 Photocatalytic activity of the TiO_2-WO_3/PANI composite membrane
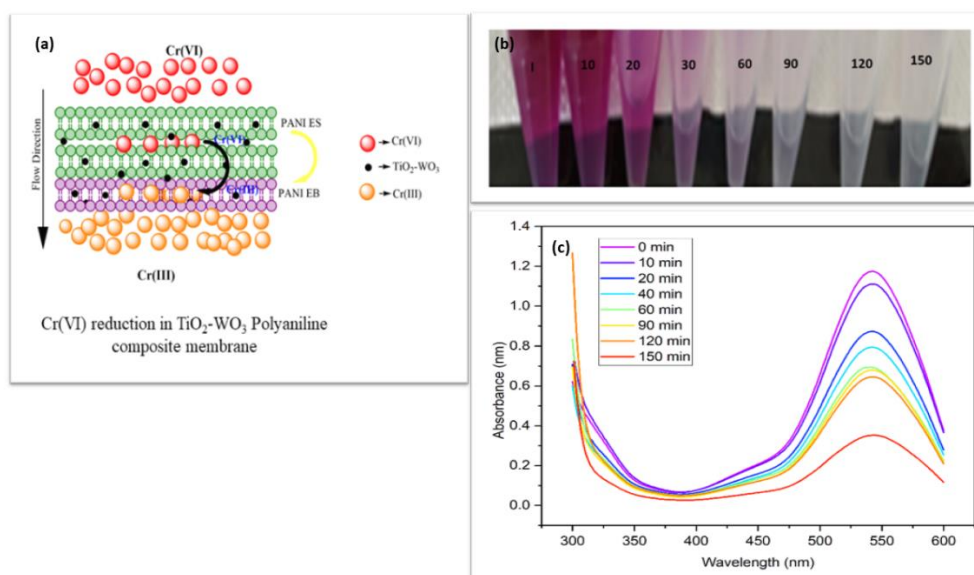
Figure 7.9(a). Schematic diagram for the Cr(VI) reduction in a TiO_2-WO_3-PANI composite membrane, (b) The colour change appeared in the DPC colorimetric method and (c). UV-Visible spectra showing the decrease in the absorbance of Cr(VI) during reduction process (for representation)

In Figure 7.9(a), the typical schematic representation of Cr(VI) reduction via separation using TiO_2-WO_3 blended PANI composite membrane is shown. Cr(VI) feed passes across the membrane fitted in a dead end filtration cell operated at a high pressure. During the separation process, adsorption of Cr(VI) anions occurred on the protonated membrane surface and during separation through nanofiltration membrane, the reduction of Cr(VI) to Cr(III) occurs. For a 15 ppm Cr(VI) sample at native pH, 98.5% Cr(VI) reduction/removal occurred within 60 min. The colour change occurred in the DPC method, which is shown in Figure 7.9(b). The purple color start to disappear as the concentration of Cr(VI) decreased in the permeate concentration from 60th min. Figure 7.9(c) depicts the uv-visible spectra of permeate in DPC method at 540 nm. The absorption of Cr(VI) decreases as the time progresses from 0 to 150 min.
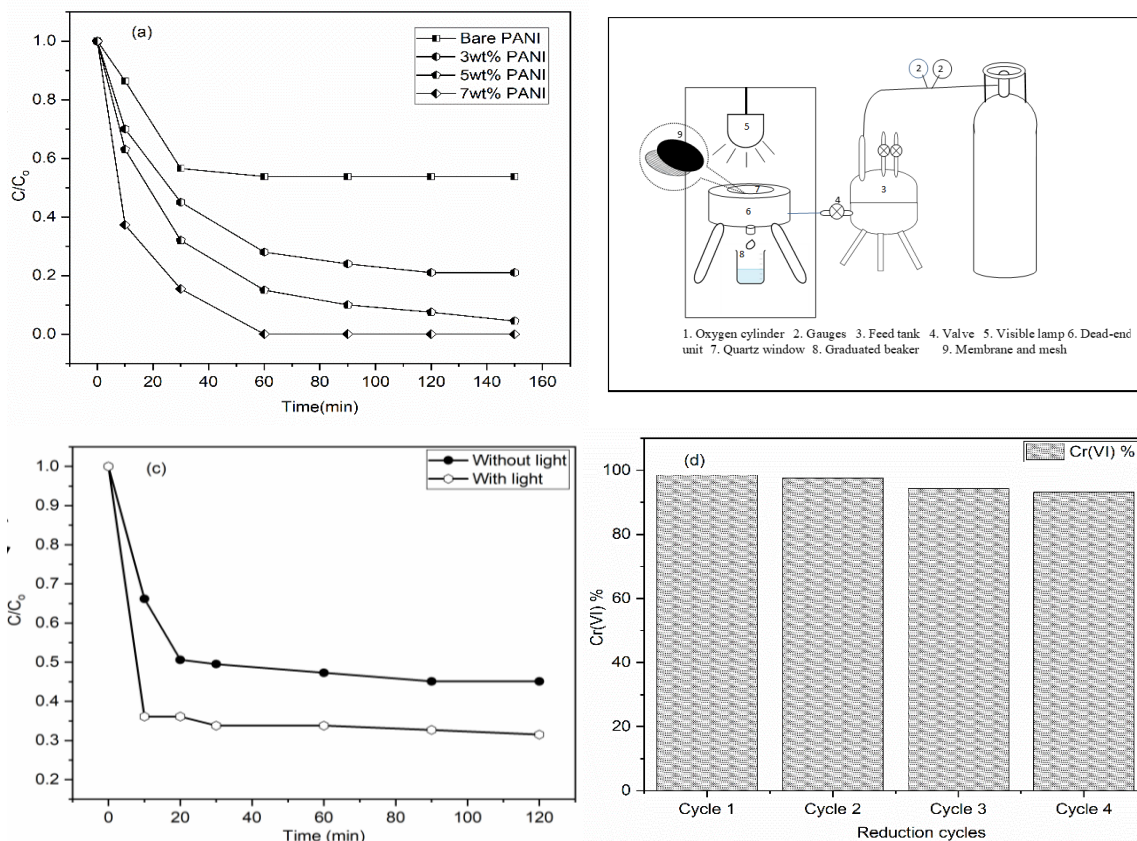
Figure 7.10 (a). Cr(VI) reduction studies using bare PANI membrane, PANI composite membrane 3 wt%, 5 wt% and 7 wt% respectively, (b). Experimental setup for photocatalytic membrane filtration (c). Cr(VI) reduction under dark and visible light using 5 wt% PANI membrane (d). Cr(VI) reduction cycles for 5 wt% PANI membrane

The removal study results and photocatalytic membrane reactor setup are shown in Figure 7.10. The batch removal results shows that, on filtration of Cr(VI) solution under dark conditions, we could able to observe 55 % Chromium removal and under visible light condition a maximum of 67.32% Chromium removal, which designates the effect of photocatalytic nanoparticles on the reduction of Cr(VI). The rapid decrease in Chromium (VI) up to the first 10 min is due to rapid absorption on the protonated surface of the membrane. It can be affirmed that each nanoparticle, which is incorporated into the membrane will act as an integrated system consists of PANI layer coated TiO_2-WO_3 core-shell typed nanocomposite, where PANI serves as a good electron acceptor and emeraldine PANI has stronger H^+ storage ability (Li et al. 2020). Similarly, TiO_2-WO_3 can provide oxygen and could play a major role in the rejection of heavy metal ions (Sunil et al. 2018).

CHAPTER 8

HIERARCHICAL PHOTOCATALYTIC MEMBRANE FOR EFFICIENT REMOVAL OF CHROMIUM IN A PHOTOCATALYTIC MEMBRANE REACTOR

8.1 INTRODUCTION

A great deal of heavy metal polluted water is produced from the different industries such as tanneries, metal plating industries, textile industries, wood industries, paint and pigment industries, fertilizers, and other chemical industries. Chromium is a notorious heavy metal and dangerous carcinogen among other heavy metals. Chromium exists majorly in two oxidation states, highly toxic hexavalent Cr(VI) and less toxic trivalent Cr(III) (Ali et al. 2016a),(Oliveira 2012),(Mavinakere Ramesh and Shivanna 2018),(Wu et al. 2013). The excess concentration of Cr(VI) in water and soil causes skin rashes, nose bleeding, respiratory tract infection, and lung cancer in humans. According to the central pollution control board of India, the maximum allowable concentration of Cr(VI) in the drinking water is 0.5 mg/L (Muthumareeswaran et al. 2017). The Cr(III) is less toxic and is essential for human metabolic activities and plant growth. The conversion of toxic Cr(VI) to Cr(III) is a helpful remedy to mitigate Cr(VI) pollution from the water bodies. The major conventional techniques used for the remediation of Cr(VI) includes ultrasonic separation, coagulation, air floatation, gravity settling, membrane filtration, and advanced oxidation techniques such as photocatalysis (Golshenas et al. 2020). These methods are economically not viable due to their high operating cost, wide footprints, and production of large amounts of sludge and secondary pollutants (Nair and Jagadeesh 2017),(Bai et al. 2010). However, among all accessible techniques, the advanced oxidation process (AOP) got the attention of researchers due to its capability to eliminate a wide range of organic and inorganic pollutants. To endorse the efficacy of hazardous wastewater treatment, photocatalysis can be coupled with the membrane filtration process as a single unit which is called as photocatalytic membrane reactor (PMR) (Golshenas et al. 2020),(Kuvarega and Mamba

2016),(Horovitz et al. 2016),(Dzinun et al. 2016),(Luo et al. 2020). Among many membrane designs, a hierarchical membrane with nanoparticles coating is an alternative for multifunctional membranes (Bai et al. 2010).

Nair et al. prepared TiO_2-graphene oxide nanosheet coated hierarchical membranes for the simultaneous photodegradation and filtration of Congo red dye under photocatalytic irradiation. The major drawback reported by them is the weakening of catalyst activity due to the fouling of the membrane due to dye adsorption on the membrane (Nair and Jagadeesh 2017). In the literature, various TiO_2 structures such as nanoparticles, nanowires, nanofibers, nano-thorns, and microspheres have been considered as compatible materials for the fabrication of hierarchical membranes (Bai et al. 2010; Nair and Jagadeesh 2017). Dzinun et al. reported immobilization of hybrid TiO_2/clinoptilolite (TCP) photocatalyst at the outer layer of the double-layer hollow fiber (DLHF) PVDF membranes. TiO_2/CP photocatalysts were synthesized by the solid-state dispersion method. TiO_2 (10 wt%)/CP (90 wt%) could yield 95% demineralization of Reactive Black 5 (RB5) in the photocatalytic membrane reactor under UV illumination (Dzinun et al. 2019).

TiO_2 is a widely used semiconductor in photocatalysis for different applications where the wide bandgap and faster charge recombination of TiO_2 limit its use. Yang et al. introduced facet-dependent heterogeneous catalysis by producing anatase TiO_2 with dominant (001) facets having high surface energy, and it can narrow down the bandgap of traditional anatase TiO_2 (Yang et al. 2008). The anatase TiO_2 crystal structure consists of three types of facets, such as (101), (100), and (001). In (101), there are two types of exposed Ti-O coordination structures, one has 3 oxygen atoms coordinated to 6 Ti atoms and the other has 2 oxygen atoms coordinated to 5 Ti atoms. All (001) facets exist as 2 oxygen atoms coordinated to 5 Ti atoms (Zhao et al. 2015). The (001) facets of anatase TiO_2 have high photocatalytic activity because of their high surface energy (0.9 J/m^2) and 100 % unsaturated Ti5C atoms (Sajan et al. 2016). Han et al. have reported the (001) preparation using tertbutyl titanate $(Ti(C_4H_9O)_4$ as a precursor and HF as a capping agent under hydrothermal conditions, and it is capable of producing TiO_2 nanosheets which can be used as photocatalysts.

Polyaniline (PANI) is one of the most investigated conductive polymers to fabricate membranes due to its excellent membrane forming capability, intrinsic transport properties, environmental stability, and tunable properties (Rohani et al. 2017a);(Wang et al. 2019).

Literature has proven that PANI in different morphologies can be used as a super adsorbent material for the removal of Cr(VI) (Zare et al. 2018). In this work, we have fabricated a hierarchical PANI membrane using hydrothermally prepared TiO_2-WO_3 nanoparticles, for the removal of Cr(VI) under visible light irradiation in a photocatalytic membrane reactor (PMR). The nanoparticle synthesis process is optimized to achieve the desired particle characteristics and the prepared catalyst is used in the preparation of the hierarchical membrane for Chromium reduction and separation.

8.2 MATERIALS

Polyaniline EB (MW = 100,000), 4-methyl piperidine (4-MP), N-methyl pyrrolidone (NMP), 1,5-diphenylcarbazide (DPC), Titanium butoxide 97% reagent grade and Sodium tungstate dihydrate was procured from Sigma Aldrich and hydrofluoric acid (HF), 48 % was purchased from Merk, India. Potassium dichromate ($K_2Cr_2O_7$) was procured from Fisher Scientific. Throughout the experiment, distilled water was used for preparing solutions. All the chemicals were used without any purification.

8.3 METHODS

8.3.1 Synthesis of nanoparticles

The nanoparticles were prepared by the hydrothermal method using titanium (IV) butoxide ($(Ti(OBu)_4$) and sodium tungstate dihydrate as precursors in HF solution. 5 mL of titanium (IV) butoxide was added to the known quantity of HF and stirred for 30 min. A pre-calculated amount of sodium tungstate dihydrate was added to the reaction mixture and stirred for 1 hour at 300 rpm using a magnetic stirrer. The reaction mixture is then transferred to a 100 mL Teflon-lined autoclave and heated at 200°C for 24 h. The prepared sample was cleaned by centrifugation using surplus amounts of water and ethanol. Obtained blue-colored nanoparticles were dried overnight at 60°C in an electric oven. The same procedure was followed for synthesizing TiO_2 nanosheet without the addition of a tungsten precursor. The prepared nanoparticles were then ground and stored at room temperature for further use.

8.3.2 Preparation of Polyaniline membrane

The membranes were prepared using PANI EB (MW=100,000) salt, dispersed in NMP solution, and 4-MP was used to arrest the gelation of PANI. The mixture was stirred for 4

h at a stirring speed of 500 rpm to get a dispersion of PANI. The pure PANI membrane was prepared without adding the nanoparticles. The viscous solution was then cast over a glass plate using a finely polished glass rod and the membrane thickness was maintained at 200 µm. The glass plate was allowed to dry for 30 s and then immersed in a coagulation bath containing deionized water for phase inversion. The membranes were immersed in the deionized water bath for 24 h for the complete precipitation of the membrane by removing residual solvent and then stored in the refrigerator for further use.

8.3.3 Fabrication of TiO₂-WO₃ nanosheet coated hierarchical membranes

The hierarchical membranes were prepared by coating TiO_2-WO_3 nanocubes on the protonated bare Polyaniline membranes. The nanoparticles were dispersed in 100 mL water and sonicated for a known time interval. The suspension was separated in a dead-end filtration cell (HP 4750, Sterlitech, USA) at an operating pressure of 0.5 MPa for 1 hour (Rathna et al. 2021). During filtration, nanoparticles were coated uniformly on the bare Polyaniline membrane and the hierarchical membranes were designated according to the amount of nanoparticle coated, as M0 (0 mg), M1 (50 mg), M2 (75 mg), and M3 (100 mg) respectively.

8.4 MEMBRANE PERMEABILITY AND Cr(VI) REDUCTION IN THE PHOTOCATALYTIC MEMBRANE REACTOR

8.4.1 Performance study of the hierarchical membranes: Permeability

The permeation properties like pure water flux of the pure and coated membranes were studied in a lab-scale dead-end filtration set-up with a quartz glass window on the top, which enables visible light irradiation. The pure water flux analysis was carried out for all the prepared membranes at a transmembrane pressure of 0.3 MPa with an active surface area of 14.60 cm^2. The dead-end cell was connected to a feed tank of 2 L capacity and pressurized using an oxygen cylinder (shown in Figure 8.1). The permeate flux was calculated using the following equation,

$$J= \frac{Q}{A.\Delta t} \qquad \rightarrow (1.0)$$

Where Q is the volume of the permeate collected at a time, t (Liters), A is the active surface area of the membrane (m^2), Δt is the time interval at which the permeate was collected (h). The flux (J) is expressed in L/m^2.h.
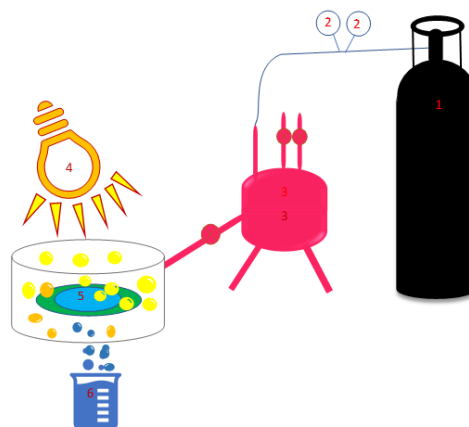
1. Oxygen cylinder 2. Gauges 3. Feed tank 4. Visible light source
5. PMR containing hierarchical PANI membrane 6. Graduated beaker

Figure 8.1 Photocatalytic membrane reactor setup

8.4.2 Performance study of the hierarchical membranes: Cr(VI) reduction

The prepared membranes were used for the removal of Cr(VI) under visible light. 300 W ultra Vitalux Osram sun lamp (2600 Lux) was used to irradiate the membrane cell. The residual Chromium (VI) in the permeate was calculated using the Diphenyl carbazide (DPC) colorimetric method at a wavelength of 540 nm. The total chromium in the solution was obtained by the ICP-OES method. The Cr(VI) remaining in the permeate was calculated by the following equation,

$$\text{Remaining Cr(VI)} = C/C_o \qquad\qquad \rightarrow (2.0)$$

Where C is the concentration of Cr(VI) in the permeate at time 't' and C_o is the initial concentration of Cr(VI) in the feed solution.

8.5 CHARACTERIZATION OF NANOPARTICLES AND HIERARCHICAL MEMBRANES

Prepared nanoparticles were characterized using Transmission Electron Microscopy (TEM, JEOL JEM-2100, 200 kV, LaB_6 electron gun) and an X-ray diffractometer (Malvern Panalytical 3rd Gen Empyrean diffractometer, operated at 40 kV and 40 mA using CuKα radiation). Diffuse reflectance spectra of the prepared samples were obtained using a Shimadzu, UV-2600 UV-Visible spectrophotometer. The surface area and pore volume of the prepared nanoparticles were analyzed by the BET (Brunauer-Emmett-Teller) method in an Anton Paar Quantachrome instrument operated at 77 K. Membrane coupons were dipped in liquid nitrogen and then broken to pieces to get a well-defined cross-section and

sputtered with gold to impart electrical conductivity. The morphology of the membrane samples was analyzed under a Scanning Electron Microscope (SEM, Jeol 6390 LA, operated at 0.5-30 kV accelerating voltage). Total Chromium in the solution was calculated by inductively coupled plasma analysis (ICP-OES, Agilent Technologies 5100).

8.6 RESULT AND DISCUSSION

8.6.1 Characterization of TiO_2-WO_3 nanoparticles

8.6.1 TEM and FE-SEM analysis for the TiO_2-WO_3 nanoparticles
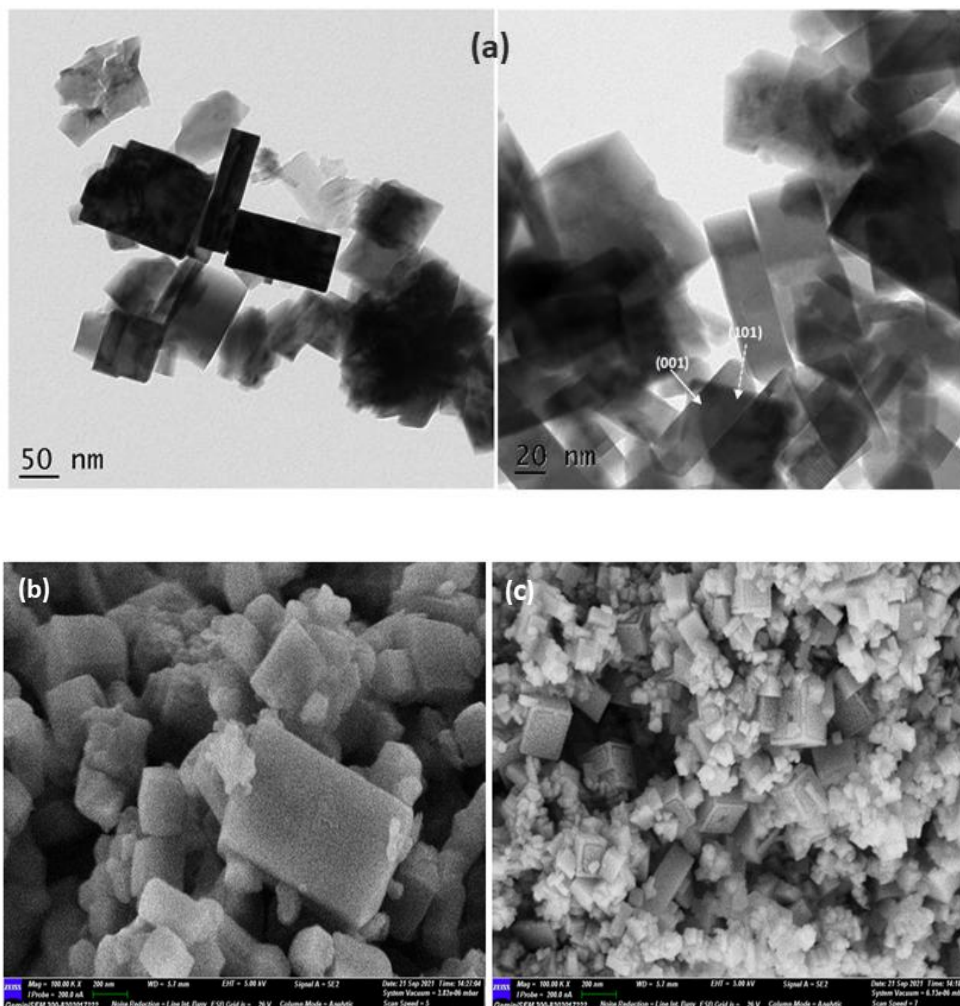
Figure 8.2(a) TEM images of TiO_2, FE-SEM images of (b). TiO_2 and (c). TiO_2-WO_3 nanocubes.

The morphology of the prepared TiO_2 and TiO_2-WO_3 nanocubes were shown in Figure 8.2. The agglomerated particles having cube-like structures of size between 33-60 nm were observed in the image. TiO_2-WO_3 nano polyhedral structure (typical truncated bipyramidal or decahedra) consists of two flat and one square (001) surfaces and eight hexagonal (101) facets (fig.2(c)) (Liu et al. 2010) were observed in the image. The unsaturated Ti5C in the nanostructure is responsible for the stability, adsorptive ability, and catalytic activity of the photocatalyst with (001) facets. It was suggested by Liu et al. that, Fluoride ions can strongly interact with (001) facets, which can reduce the surface energy and can kinetically inhibit the crystal growth. These factors favor the formation of (001) facets during the hydrothermal process. The lattice fringes corresponding to 0.34 nm of (101) plane of TiO_2 were observed from the TEM analysis which confirmed the presence of TiO_2 in the nanocubes.

8.6.2 XRD pattern for TiO_2 and TiO_2-WO_3 nanocubes
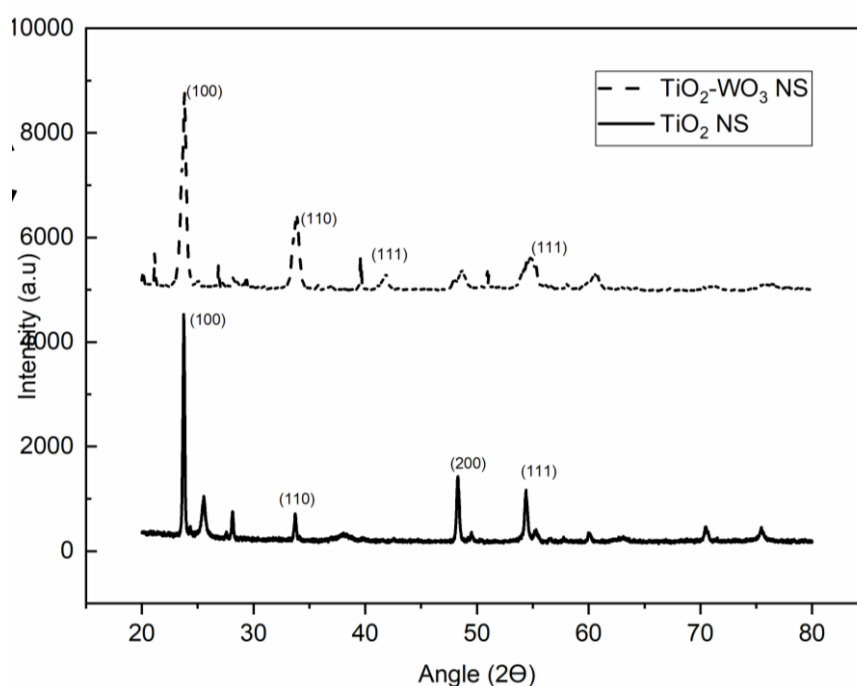
Figure 8.3. XRD patterns for TiO_2 and TiO_2-WO_3 (40:1) nanocubes

Figure 8.3 shows the XRD pattern of pure TiO_2 and TiO_2-WO_3 (40:1) nanocubes. The peak corresponds to 25.19^o and 47.81^o represents the crystal plane (101) and (200) of TiO_2 anatase (ICDD 01-083-5916). A prominent peak at 23.40^o attributed to (100) plane of titanium fluoride (ICDD 01-077-0132). The peak at 33.33^o corresponds to the plane (110) of $TiOF_2$ (ICDD 01-077-0132) and also confirmed by the TEM analysis at a fringe spacing

of 0.32 nm. The peak at 41.54° and 54.83° are corresponding to the plane (111) and (102) of tungsten hydrogen oxide (ICDD 00-023-1449), and the peak at 54° represents the (111) plane of TiO_2 (Mugunthan et al. 2018a). No distinct peaks of tungsten oxide (WO_3) were found, which may result from the meagre crystallization and low tungsten content in the composite system (Liu et al. 2014a).

8.6.3 Bandgap estimation of TiO_2 and TiO_2-WO_3 nanocubes
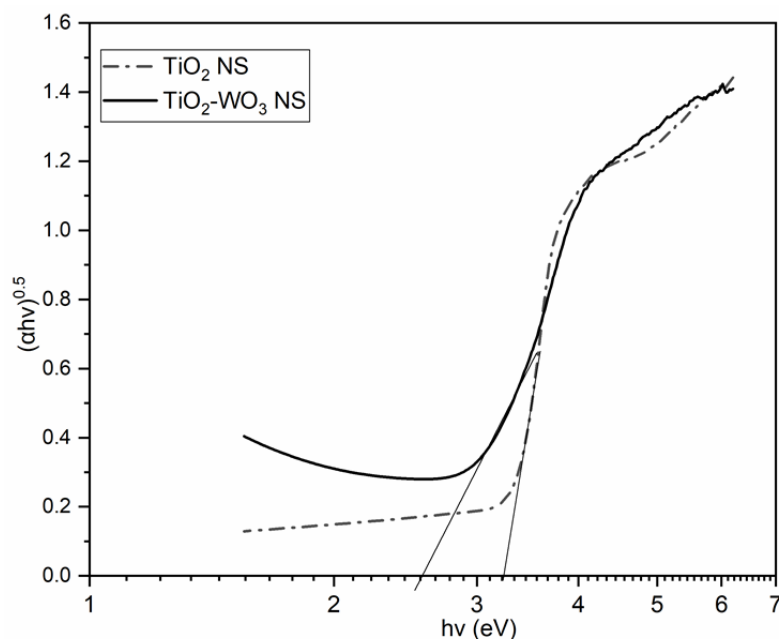
Figure 8.4. The Tauc plots for bandgap estimation of pure TiO_2 and TiO_2-WO_3 (40:1) nanostructures.

The Tauc plot indicates the reduction in the bandgap from 3.2 eV to 2.6 eV (in Figure 8.4) when WO_3 content was added to the TiO_2 (Hu et al. 2018b). The bandgap of WO_3 is reported in the range of 2.4-2.8 eV (Mugunthan et al. 2018b). TiO_2-WO_3 visible light catalyst by the simplest hydrothermal method was synthesized and utilized for the reduction of Chromium (VI) in aqueous solutions. The BET analysis results of TiO_2-WO_3 (40:1) nanocubes showed a surface area of 6.864 m^2/g, pore volume of 2.29 cc/g, and a pore radius of 6.665 nm. The BET results suggest that the produced TiO_2-WO_3 complex can be a potential photocatalyst.

8.6.4 Hierarchical PANI membrane characterization

Hydrothermally obtained TiO_2, TiO_2-WO_3 (40:1) nanocubes, PANI EB, protonated PANI ES membrane, and TiO_2-WO_3 coated hierarchical membranes are shown in Figure 8.5. The

prepared bare PANI membranes were in PANI EB form with a bronze shining lustre on the surface. The membranes were protonated using HCl before coating the nanocatalyst and the coated TiO_2-WO_3 could anchorage efficiently to produce a stable coating on the hierarchical membrane. The stability of the coating was analyzed by dipping the coated membrane in an aqueous solution multiple times. The coated membrane showed better stability, which was concluded based on the analysis of TiO_2-WO_3 in the dipping solution.
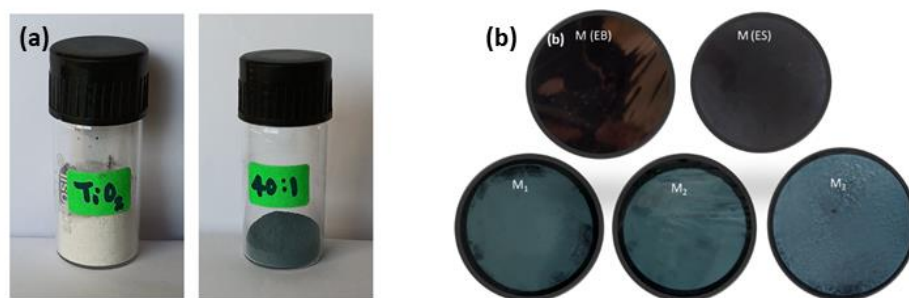
Figure 8.5 (a).TiO_2 nanocubes, TiO_2-WO_3 (40:1) nanocubes, (b).Bare Polyaniline membranes are deprotonated (EB), protonated (ES), and TiO_2-WO_3 nanoparticle coated hierarchical membranes M1, M2, and M3 (50 mg, 75 mg, and 100 mg respectively).

8.6.5 SEM Analysis
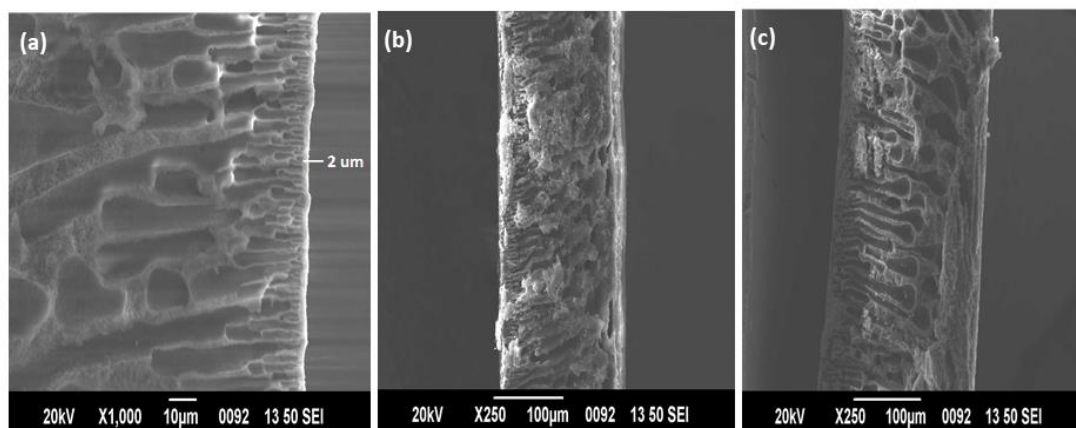
Figure 8.6 SEM image of TiO_2-WO_3 coated M1, M2, and M3 membrane cross-section

The SEM images of the cross-section of TiO_2-WO_3 coated asymmetric membranes, M1, M2 and M3 are shown in Figure 8.6. From figure 8.6(a), it is evident that the PANI M1 membrane was coated with stable TiO_2-WO_3 (50 mg) nanocubes having 2 um thickness. A few nanocubes placed on the surface of the membrane might have gone inside the

membrane and could clog the membrane. This can be indirectly confirmed using a change in the water flux. In M2 and M3 membranes, the clogging by nanosheet is obvious compared to M0 and M1. The pure PANI membranes were observed to be under the category of nanofiltration and the clogging of pores has pushed the hierarchical membranes, particularly M2 and M3 under the ultrafiltration range.

8.6.6 Pure water flux (PWF) analysis of hierarchical PANI membranes
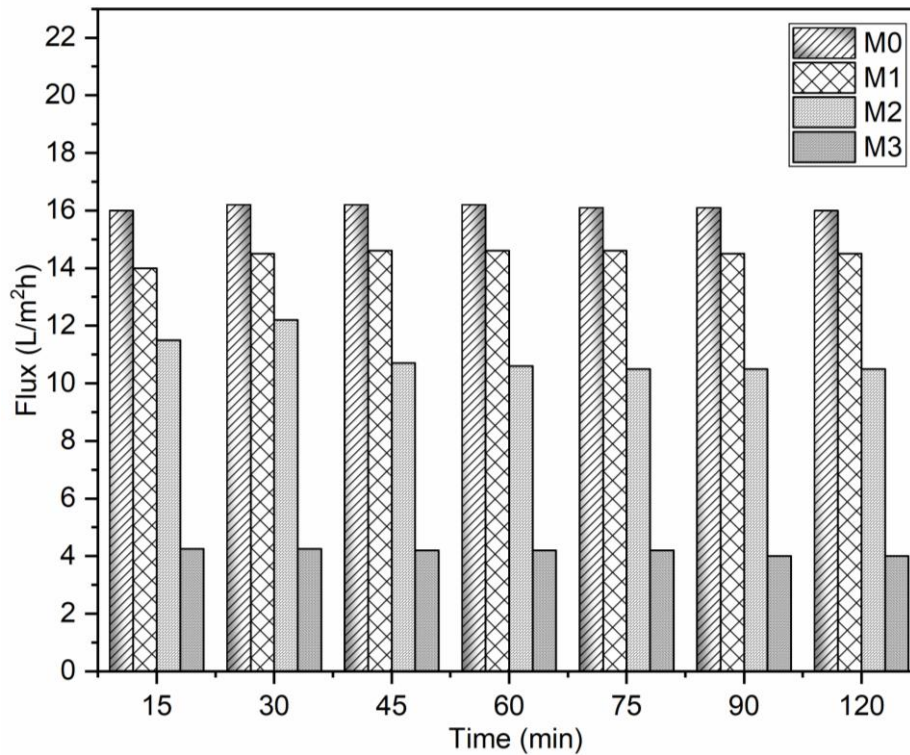
Figure 8.7 Pure water flux of bare PANI (M0) and TiO_2-WO_3 coated PANI (M1, M2, and M3) hierarchical membranes

Figure 8.7 shows the pure water flux of M0, M1, M2, and M3 PANI hierarchical membranes. The pure water flux obtained for the bare PANI membrane and hierarchical membranes was 14.5, 12, 10.5, and 4 L/m^2.h (M0, M1, M2, and M3) respectively. The bare PANI membrane flux appears to be higher than the other membranes. The M1 membrane showed higher flux due to unplugged open channels for water transport compared to other TiO_2-WO_3 coated membranes. The permeation characteristics of various hierarchical membranes are given in Figure 8.7. The addition of TWNS on the membrane surface blocks the pores and results in the reduction of permeate flux (Nair and Jagadeesh 2017; Syafei et al. 2008). A gradual decrease in the flux was observed as the TWNS concentration on the

128

membrane increased, but the reduction also gradually increased due to the prolonged exposure due to lower flux.

8.6.7 Performance study on Chromium (VI) removal

Cr(VI) reduction/removal capacity of hierarchical membranes prepared with TiO_2 and TiO_2-WO_3 nanoparticles was analysed using a 15 ppm Cr(VI) solution at its native pH (pH 5.80) in a customized photocatalytic membrane reactor. Pure filtration experiments were performed under visible light irradiation in a customized experimental setup as shown in section 8.4.1. To check the adsorption capacity of the hierarchical membrane, pure adsorption experiments were performed under dark conditions using an M1 membrane. During the absorption study, the concentration of Cr(VI) dropped due to the adsorption capacity of PANI at its emeraldine salt (ES) state (Li et al. 2018a). A maximum Chromium removal of about 51.70 % was achieved using M1 membrane under dark. The M1 membrane surface turned yellow due to the retention of Cr(VI) on the membrane after the completion of the adsorption experiment. Filtration under darkness can be avoided if photocatalytic reduction is the major goal. Further, M1 membrane showed a maximum Chromium reduction of about 72.1% at 30 min, during photocatalytic filtration experiment under light irradiation.

In general, depending on the Cr(VI) solution pH, Cr(VI) exists in different forms such as chromate (CrO_4^-), hydro chromate ($HCrO_4^-$), and, dichromate ($Cr_2O_7^{2-}$) (Ali et al. 2016a). The ES form of PANI will be rich in amine and imine functional groups and the amines can chelate the metal ions, which helps in the adsorption and reduction of Cr(VI) anions (Bozkir et al. 2012; Ding et al. 2018; Macdiarmid et al. 1987). When visible light strikes the membrane, the photocatalytic reduction of Cr(VI) on TiO_2-WO_3 catalysts takes place. But, when the thickness of the catalyst layer increases on the membrane surface, Cr(VI) degradation reduces due to the lower penetration of light to the entire thickness, whereas, lesser thickness offers a rapid photocatalytic reduction. Hence the thickness of the hierarchical membrane should be such that it photo reduces a maximum amount of Cr(VI) and simultaneously offer minimal flux drop (Nair and Jagadeesh 2017).

The M1 membrane showed the highest reduction-separation of Cr(VI) of about 79.30 % under visible light irradiation in the PMR. Other membranes could yield Cr(VI) removal of 28.95 % (M0), 36.80 % (M2), and 71.75 % (M3) at 120th min (shown in Figure 8.8). The reduction efficiency of the M1 membrane (79.30 %) can be further improved by designing

an augmented membrane reactor to utilize the complete light irradiation and reduced temperature effects. PANI has the prominent merit of having a high absorption coefficient in the visible light region (Li et al. 2018a). Further, it was observed that the rise in the temperature due to continued light exposure did not affect the performance of hierarchical membranes in reducing Chromium (VI) even beyond 30 min.
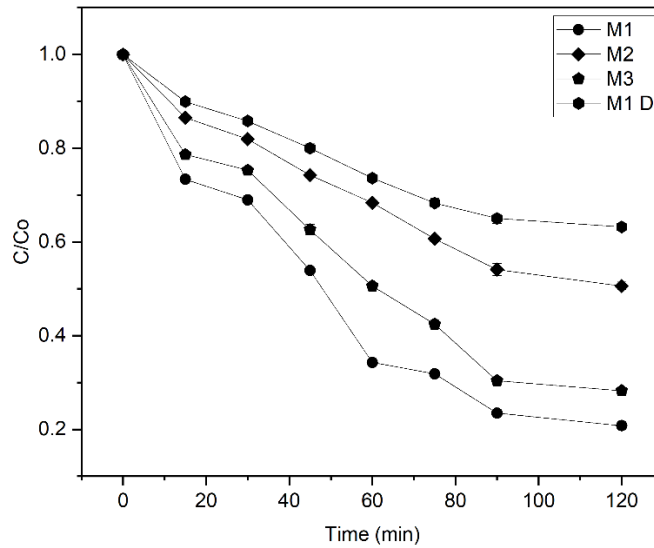
Figure 8.8 Chromium (VI) reduction in the photocatalytic membrane reactor using different membranes

8.6.8 Shelf life and reusability of the membrane
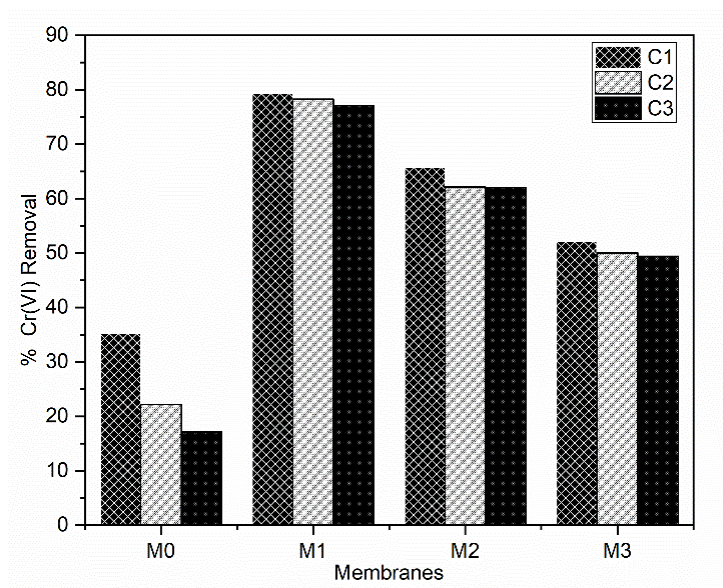
Figure 8.9 Reusability studies for M0, M1, M2, and M3 membranes.

The membranes were reused in three cycles (shown in Figure 8.9) and it has been observed that the efficiency of the M1 membrane did not decrease even after the 3rd cycle. Hierarchically modified membranes exhibited stable and excellent photocatalytic performance in PMR. Whereas, the bare PANI membrane (M0) showed fouling due to Cr(VI) deposition on the membrane. This led to the deprotonation of the membrane and flux reduction. It was observed that the catalyst-coated hierarchical membranes showed negligible fouling and deprotonation during Cr(VI) membrane separation under visible light irradiation (in PMR). This indicates the high availability of the TiO_2-WO_3 catalyst for the adsorption and reduction of the Cr(VI) in the PMR. This helped the Cr(VI) reduction on the catalyst layer itself and prevented it from direct contact with the PANI membrane. The degree of deprotonation was minimal with regard to the hierarchical assembly of the membranes. The photocatalytic activity of the membrane was highly reproducible and the results were consistent until the third cycle of the membrane. The concentration of the catalyst on the surface of the membrane will affect the water flux and separation performance of the membrane. This demonstrates that the membrane can alleviate the fouling. This supports visible light irradiation as a new method for membrane cleaning in the case of hierarchical membranes.

8.6.9 Comparison of our work with other works

Table 8.1 Comparison of our work with the other literature

Nanoparticle used	Polymer used	Light source	Application	Efficiency	References
TiO_2 nanothorn spheres (Hydrothermal method)	Cellulose acetate	UV light	Humic acid and Methyl Blue degradation	100 %	(Bai et al. 2010)
$SrTiO_3$/TiO_2 nanofibers	Cellulose acetate	UV light	Acid Orange 7	100 %	(Bai et al. 2015)
GO-TiO_2 nanospheres	Cellulose acetate	UV light	RhB and AO7	100%	(Gao et al. 2013a)
TiO_2-V_2O_5	Cellulose acetate	UV light	RhB dye degradation	95 %	(Gao et al. 2013b)

TiO$_2$-SnO$_2$ hollow nanofiber	TiO$_2$-SnO$_2$ hollow nanofiber	Under UV light	RB5, RhB degradation	100 %	(Ahn et al. 2016)
GO/PVDF and GO/C$_3$N$_4$/PVDF	Polyvinylidene fluoride	Under visible light	Oil-in-water separation	98 %	(Shi et al. 2019)
CuO/ZnO	Glass fiber membrane	Under UV light	Methyl blue, RhB and AO7 degradation	100 %	(Liu et al. 2012)
TiO$_2$ nanosheet-GO	Cellulose acetate	Under UV light	Congo red dye	100 %	(Nair and Jagadeesh 2017)
TiO$_2$-WO$_3$ nanocubes	Polyaniline membrane	Visible light	Chromium (VI)	79.30 %	Our work

Hierarchically organized membranes with multiscaled structures enhance light reflection and adsorption. The improved visible light utilization rate and photocatalytic activity due to enlarged surface area reduced photo corrosion. These multifunctional membranes allow easy recovery of the nanoparticles and their reuse. The comparison of our work with the other literature is given in Table 8.1. Highly reactive TiO$_2$-WO$_3$ nanoparticles on the membrane make the hierarchical membrane more photocatalytic active, avoid deprotonation, and help to maintain the PANI membrane's filtration efficiency.

CHAPTER 9

SUMMARY AND CONCLUSION

9.1 SUMMARY

In the present work, coupled mixed metal oxide catalysts such as TiO_2-WO_3 and TiO_2-SnO_2 were successfully synthesised through the low-cost hydrothermal method. The catalysts have been used for the degradation of hexavalent Chromium from an aqueous solution under visible light. TiO_2-WO_3 (40:1) in the suspension mode showed the highest photocatalytic activity within 120 min under visible light without any hole scavengers. The disadvantages like faster recombination, recovery of catalyst, and agglomeration of nanoparticles in the suspension mode can be avoided by immobilizing the nanoparticle on a polymer membrane. In this work, we discuss the scope of combining the processes of membrane filtration and photocatalysis into a single smart unit called a photocatalytic membrane reactor (PMR). Here, we develop photocatalyst blended composite membranes and photocatalyst coated hierarchical membranes. Reduced fouling, increased hydrophilicity of the membrane, easy recovery of the photocatalyst, and extended shelf life could be offered by these multifunctional photocatalytic membranes. In this study, the membrane material used is the conjugated polymer Polyaniline (PANI) due to its properties like ease of preparation, economic viability, environmental stability, higher conductivity, excellent tuneable properties, and redox behaviour. Using TiO_2-Polyaniline based membranes, we were able to successfully remove and reduce the highly toxic Cr(VI) to its less toxic Cr(III) in a photocatalytic membrane reactor. We believe that this strategy can broaden the potential application of these multifunctional membranes (composite and hierarchical) for the next-generation membrane separation process.

9.2 CONCLUSIONS

Hereunder are a few key findings from the ongoing research that are thought to fill in some knowledge gaps regarding creating a photocatalytic membrane reactor based on a

Polyaniline membrane for the simultaneous removal and reduction of hexavalent Chromium to trivalent Chromium.

❖ The hydrothermal method was used to produce TiO_2-WO_3 coupled metal oxide catalysts. TiO_2-WO_3 (40:1) showed the highest photocatalytic activity within 120 min under visible light, which is on par with the literature reported values. The statistical analysis using Response Surface Methodology (RSM) based Box-Behnken method was used to develop a quadratic polynomial model to predict the optimized condition to reduce Chromium (VI).

❖ The reduction results showed a maximum Chromium reduction of 97.91% under the following conditions: an initial pH-1, catalyst loading-0.4 g/L and initial concentration- 10 ppm. According to the analysis of variance (ANOVA), the obtained R^2 value was 0.9996.

❖ TiO_2-SnO_2 metal oxide catalysts using different molar ratios (10:1, 20:1, 30:1, and 40:1) were synthesized using the hydrothermal method. The average particle size of the catalysts ranged from 11-16 nm.

❖ TiO_2-SnO_2 metal oxide catalysts are successfully used to reduce highly toxic hexavalent Chromium to a less harmful form of Chromium i.e. Cr(III) under visible light in the presence of citric acid. Among the prepared catalysts, TS40 showed the highest photocatalytic activity. The complete reduction of 15 mg/L Cr(VI) was observed at a catalyst dosage of 0.6 g/L, pH 3.0, and at 0.8 g/L citric acid.

❖ We were able to conclude that the addition of citric acid in the reaction mixture completely inhibits the reoxidation of Cr(III) to Cr(VI)

❖ After three consecutive cycles, the unsonicated catalyst showed a reduction efficiency of around 17.21 % and the sonicated catalyst showed a reduction efficiency of around 100%.

❖ PANI/TiO_2 nanocomposites prepared by in-situ chemical polymerization were used for the reduction of Cr(VI) under visible light. The prepared nanocomposites PT1, PT5, PT10 and PT15 were mesoporous, with a wider pore size distribution.

❖ The PANI shell on the TiO_2 core structure could enhance photocatalytic efficiency, metal anion adsorption, reductive adsorption of Cr(VI) and desorption of Cr(III) on the surface of nanocomposites.

❖ The higher oxidative stability, moderate surface area and hydrophilic functionalities on the surface of the nanocomposites are often contributed to higher Cr(VI) reduction. The photocatalytic activity was comprehensively affected by the ratios of PANI/TiO_2.

- The PT15 catalyst with 15% PANI content appeared to be the best photocatalyst under visible light in the reduction of Cr(VI). The complete reduction was observed under pH 3.0 of 15 ppm Cr(VI) solution for an irradiation time of 90 min at 1g/L catalyst dosage.

- The PANI ES has a very good adsorption capacity and adsorbs Cr(VI) completely, but PANI/TiO$_2$ is able to adsorb Cr(VI) adsorption as well as gradual reduction to Cr(III). The results prove that the acidic pH and the higher PANI content favour the Cr(VI) reduction.

- The Polyaniline membranes were prepared in different PANI weight percentages from 10,12.5, 15 to 17.5%, and among them, 15 and 17.5% appeared mechanically stable.

- It has been already revealed that at lower pH, PANI is capable of adsorbing Cr(VI) completely and we had studied the adsorption behaviour of the membranes.

- The adsorption isotherm studies revealed that the adsorption of Cr(VI) ions occurs either physically or chemically on the multilayer heterogeneous adsorption sites of the PANI membrane.

- The adsorption isotherm fits Freundlich and Jovanovic's multilayer adsorption isotherm equations. Freundlich and Jovanovic's adsorption isotherms indicate favourable multilayer chemisorption and reduction of Cr(VI) occurs on the membrane surface.

- The hydrothermally synthesized TiO$_2$-WO$_3$ nanoparticles were effectively incorporated into the PANI polymer matrix to improve its properties. The prepared TiO$_2$-WO$_3$ (Ti:W = 40:1) was mesoporous nanoparticles with a high surface area (173.57 m^2/g) and the optimum concentration of WO$_3$ provides higher stability, improved visible light activity, electron acceptance, and charge separation efficiency.

- The composite membrane with 5 wt% nanoparticles has enhanced the properties of the membranes like hydrophilicity, permeance, high-quality permeate, and Cr(VI) reduction capacity by improving the membrane quality and adsorption sites.

- The fluxes of composite PANI membranes were in the range of 37.76 to 143.5 L/m^2.h. The nanoparticle incorporation improves degradation by both filtration and photocatalysis.

- The enhanced membrane materials could act as a single photocatalytic membrane reactor in which the remediation of other inorganic-organic pollutants is possible.

- The maximum removal time for Cr(VI) to get 98.50 % separation in 60 min. The reusability remained stable even after four rejection cycles. The results show that nanoparticle-incorporated membranes are capable of reducing Cr(VI) under visible light.

- TiO$_2$ based nanosheets, nanotubes, and nano-thorns have shown higher surface adhesion capacities. We could successfully prepare TiO$_2$-WO$_3$ nanocubes coated hierarchical PANI

membranes for the photocatalytic membrane reactor applications. TiO_2-WO_3 nanocubes were successfully synthesized using the particle range of 33-60 nm.

❖ The hierarchical membranes were prepared by depositing TiO_2-WO_3 nanocubes on the bare PANI membranes by a membrane filtration process at 0.5 MPa pressure in a UF membrane testing cell. These multifunctional membranes showed higher water affinity, enhanced water flux, extremely good Cr(VI) reduction, reduced fouling, and self-cleaning abilities.

❖ At higher catalyst loading, the permeate flux is reduced due to the cake resistance offered by the catalyst coating. M1 and M2 membranes, they showed better photocatalytic efficiencies of 79.30 % and 71.75 %, respectively. The reuse cycle showed a negligible amount of unreacted Cr(VI) on the membrane surface during EDS analysis.

❖ The nanoparticle coating under visible light helps to degrade the adsorbed Cr(VI) anions on the surface and, hence, resists the PANI material from super oxidation under extremely high Cr(VI) conditions.

❖ Thus, the PANI based photocatalytic membrane reactor will be capable of treating heavy metals and textile dyes under visible light. The nanoparticles shield the PANI membrane and offer additional adsorption sites for more Cr(VI) ions.

9.3 FUTURE SCOPE

❖ Photocatalytic reduction of Cr(VI) under solar irradiation.

❖ Reduction of real time Cr(VI) samples with PANI based PMR

❖ Development of other TiO_2 based metal oxide catalysts using ZnO, CeO_2, $AgNO_3$ etc.

❖ Application of PANI membrane-based PMR for the remediation of different pollutants like textile dyes, pharmaceutical compounds, oil in water, etc.

❖ Future research can be carried out upon embedding other photocatalysts on the PANI membrane surface.

REFERENCES

Acharya, R., Naik, B., and Parida, K. (2018). "Cr(VI) remediation from aqueous environment through modified-TiO$_2$-mediated photocatalytic reduction." Beilstein Journal of Nanotechnology, 9(1), 1448–1470.

Ahn, K., Pham-Cong, D., Choi, H. S., Jeong, S. Y., Cho, J. H., Kim, J., Kim, J. P., Bae, J. S., and Cho, C. R. (2016). "Bandgap-designed TiO$_2$/SnO$_2$ hollow hierarchical nanofibers: Synthesis, properties, and their photocatalytic mechanism." Current Applied Physics, 16(3), 251–260.

Alam, M., Ansari, A. A., Shaik, M. R., and Alandis, N. M. (2013). "Optical and electrical conducting properties of Polyaniline/Tin oxide nanocomposite." Arabian Journal of Chemistry, 6(3), 341–345.

Alcaraz-Espinoza, J. J., Chávez-Guajardo, A. E., Medina-Llamas, J. C., Andrade, C. A. S., and Melo, C. P. De. (2015). "Hierarchical composite polyaniline-(Electrospun Polystyrene) fibers applied to heavy metal remediation." ACS Applied Materials and Interfaces, 7(13), 7231–7240.

Alhweij, H., Emanuelsson, E. A. C., Shahid, S., and Wenk, J. (2021). "Simplified in-situ tailoring of cross-linked self-doped sulfonated polyaniline (S-PANI) membranes for nanofiltration applications." Journal of Membrane Science, 637(March), 119654.

Ali, A., Saeed, K., and Mabood, F. (2016a). "Removal of chromium (VI) from aqueous medium using chemically modified banana peels as efficient low-cost adsorbent." Alexandria Engineering Journal, 55(3), 2933–2942.

Alias, S. S., Harun, Z., and Latif, I. S. A. (2018). "Characterization and performance of porous photocatalytic ceramic membranes coated with TiO$_2$ via different dip-coating routes." Journal of Materials Science, 53(16), 11534–11552.

Amado, F. D. R., Rodrigues, L. F., Rodrigues, M. A. S., Bernardes, A. M., Ferreira, J. Z., and Ferreira, C. A. (2005). "Development of polyurethane/polyaniline membranes for zinc recovery through electrodialysis." Desalination, 186(1–3), 199–206.

Anandan, S., Sivasankar, T., and Lana-Villarreal, T. (2014). "Synthesis of TiO_2/WO_3 nanoparticles via sonochemical approach for the photocatalytic degradation of methylene blue under visible light illumination." Ultrasonics Sonochemistry, 21(6), 1964–1968.

Argurio, P., Fontananova, E., Molinari, R., and Drioli, E. (2018). "Photocatalytic membranes in photocatalytic membrane reactors." Processes, 6(9).

Arif, Z., Sethy, N. K., Mishra, P. K., and Verma, B. (2020). "Development of eco-friendly, self-cleaning, antibacterial membrane for the elimination of chromium (VI) from tannery wastewater." International Journal of Environmental Science and Technology, 17(10), 4265–4280.

Arora, R., Saxena, A., Noori, M. Q., and Singh, A. (2014). PANI-SnO 2 Based Composite Materials & Their Application.

Asha, R. C., and Kumar, M. (2015a). "Sulfamethoxazole in poultry wastewater: Identification, treatability and degradation pathway determination in a membrane-photocatalytic slurry reactor." Journal of Environmental Science and Health - Part A Toxic/Hazardous Substances and Environmental Engineering, 50(10), 1011–1019.

Assadullah, I., Bhat, A. A., Malik, J. H., Malik, K. A., Tomar, R., and Khandy, S. A. (2022). "Electronic structure, optical, photocatalytic and charge storage performance of WO_3 nanostructures." Journal of Physics and Chemistry of Solids, 165(February), 110649.

Babel, S., and Kurniawan, T. A. (2004). "Cr(VI) removal from synthetic wastewater using coconut shell charcoal and commercial activated carbon modified with oxidizing agents and/or chitosan." Chemosphere, 54(7), 951–967.

Bai, H., Liu, Z., and Sun, D. D. (2010). "Hierarchically multifunctional TiO_2 nano-thorn membrane for water purification." Chemical Communications, 46(35), 6542–6544.

Bai, H., Zan, X., Juay, J., and Sun, D. D. (2015). "Hierarchical heteroarchitectures functionalized membrane for high efficient water purification." Journal of Membrane Science, 475, 245–251.

Baloyi, J., Seadira, T., Raphulu, M., and Ochieng, A. (2014a). "Simultaneous photocatalytic reduction of Cr(VI) and oxidation of citric acid in aqueous solutions." Intl' Conf. on Chemical, Integrated Waste Management & Environmental Engineering (ICCIWEE'2014) April 15-16, 2014 Johannesburg, (August 2018).

Barakat, M. A. (2011). "New trends in removing heavy metals from industrial wastewater." Arabian Journal of Chemistry, 4(4), 361–377.

Ben, S. H., Lahmar, H., Rekhila, G., Bouhala, A., Trari, M., and Benamira, M. (2022). "Journal of Photochemistry & Photobiology , A : Chemistry A novel $MgCr_2O_4/WO_3$ hetero-junction photocatalyst for solar photo reduction of hexavalent chromium Cr (VI)." Journal of Photochemistry & Photobiology, A: Chemistry, 430(November 2021), 113986.

Biesinger, M. C., Payne, B. P., Grosvenor, A. P., Lau, L. W. M., Gerson, A. R., and Smart, R. S. C. (2011). "Resolving surface chemical states in XPS analysis of first row transition metals, oxides and hydroxides: Cr, Mn, Fe, Co and Ni." Applied Surface Science, 257(7), 2717–2730.

Boeva, Z. A., and Sergeyev, V. G. (2014). "Polyaniline: Synthesis, properties, and application." Polymer Science - Series C, 56(1), 144–153.

Boga, B., Pap, Z., Baia, L., and Baia, M. (2018). "Detailed Spectroscopic and Structural Analysis of TiO_2/WO_3 ´ n Sz ´." 2018.

Bolagam, R., Boddula, R., and Srinivasan, P. (2017). "Hybrid Material of PANI with TiO_2-SnO_2: Pseudocapacitor electrode for higher performance supercapacitors." ChemistrySelect, 2(1), 65–73.

Bozkir, S., Sankir, M., Semiz, L., Sankir, N. D., and Usanmaz, A. (2012). "High performance Chromium (VI) removal from water by Polyacrylonitrile-co-Poly (2-ethyl hexylacrylate) and Polyaniline nanoporous membranes." Polymer Engineering and Science, 52(8), 1613–1620.

Chang, K. C., Hsu, C. H., Peng, C. W., Huang, Y. Y., Yeh, J. M., Wan, H. P., and Hung, W. C. (2014). "Preparation and comparative properties of membranes based on PANI and three inorganic fillers." 8(3), 207–218.

Chapman, P., Loh, X. X., Livingston, A. G., Li, K., and Oliveira, T. A. C. (2008). "Polyaniline membranes for the dehydration of tetrahydrofuran by pervaporation." Journal of Membrane Science, 309(1–2), 102–111.

Cheng, Q., Wang, C., Doudrick, K., and Chan, C. K. (2015). "Hexavalent chromium removal using metal oxide photocatalysts." Applied Catalysis B: Environmental, 176–177, 740–748.

Chin, S. S., Chiang, K., and Fane, A. G. (2006). "The stability of polymeric membranes in a TiO$_2$ photocatalysis process." Journal of Membrane Science, 275(1–2), 202–211.

Choudhury, P., Mondal, P., Majumdar, S., Saha, S., and Sahoo, G. C. (2018). "Preparation of ceramic ultrafiltration membrane using green synthesized CuO nanoparticles for chromium (VI) removal and optimization by response surface methodology." Journal of Cleaner Production, 203, 511–520.

Deng, X., Chen, Y., Wen, J., Xu, Y., Zhu, J., and Bian, Z. (2019). "Polyaniline-TiO$_2$ composite photocatalysts for light-driven hexavalent chromium ions reduction." Science Bulletin, (xxxx).

Díaz-Reyes, J., and Balderas-López, J. A. (2008). Obtaining of films of tungsten trioxide (WO$_3$) by resistive heating of a tungsten filament. Superficies y Vacío.

Ding, J., Pu, L., Wang, Y., Wu, B., Yu, A., Zhang, X., Pan, B., Zhang, Q., and Gao, G. (2018). "Adsorption and reduction of Cr(VI) together with Cr(III) sequestration by Polyaniline confined in pores of Polystyrene beads." Environmental Science and Technology, 52(21), 12602–12611.

Djellabi, R., Ghorab, F. M., Nouacer, S., Smara, A., and Khireddine, O. (2016). "Cr(VI) photocatalytic reduction under sunlight followed by Cr(III) extraction from TiO$_2$ surface." Materials Letters, 176, 106–109.

Djellabi, R., Zhao, X., Bianchi, C. L., Su, P., Ali, J., and Yang, B. (2020). "Visible light responsive photoactive polymer supported on carbonaceous biomass for photocatalytic water remediation." Journal of Cleaner Production, 269, 122286.

Djellabi, R., Zhao, X., Ordonez, M. F., Falletta, E., and Bianchi, C. L. (2021). "Comparison of the photoactivity of several semiconductor oxides in floating aerogel and suspension systems towards the reduction of Cr(VI) under visible light." Chemosphere, 281(May), 130839.

Dognani, G., Hadi, P., Ma, H., Cabrera, F. C., Job, A. E., Agostini, D. L. S., and Hsiao, B. S. (2019). "Effective chromium removal from water by polyaniline-coated electrospun adsorbent membrane." Chemical Engineering Journal, 372(April), 341–351.

Domenzain-Gonzalez, J., Castro-Arellano, J. J., Galicia-Luna, L. A., Rodriguez-Cruz, M., Hernandez-Lopez, R. T., and Lartundo-Rojas, L. (2021). "Photocatalytic membrane reactor

based on Mexican Natural Zeolite: RB5 dye removal by photo-Fenton process." Journal of Environmental Chemical Engineering, 9(4).

Dozzi, M. V., Marzorati, S., Longhi, M., Coduri, M., Artiglia, L., and Selli, E. (2016). "Photocatalytic activity of TiO_2-WO_3 mixed oxides in relation to electron transfer efficiency." Applied Catalysis B: Environmental, 186, 157–165.

Duan, W., Chen, G., Chen, C., Sanghvi, R., Iddya, A., and Walker, S. (2017). "Electrochemical removal of hexavalent chromium using electrically conducting carbon nanotube / polymer composite ultra fi ltration membranes." Journal of Membrane Science, 531(March), 160–171.

Dubey, S. P., Sillanpaa, M., and Varma, R. S. (2017). "Reduction of hexavalent chromium using Sorbaria sorbifolia aqueous leaf extract." Applied Sciences (Switzerland), 7(7).

Duong, P. H. H., Kuehl, V. A., Mastorovich, B., Hoberg, J. O., Parkinson, B. A., and Li-Oakey, K. D. (2018). "Carboxyl-functionalized covalent organic framework as a two-dimensional nanofiller for mixed-matrix ultrafiltration membranes." Journal of Membrane Science, 574(October 2018), 338–348.

Dzinun, H., Othman, M. H. D., and Ismail, A. F. (2019). "Photocatalytic performance of TiO_2/Clinoptilolite: Comparison study in suspension and hybrid photocatalytic membrane reactor." Chemosphere, 228, 241–248.

Dzinun, H., Othman, M. H. D., Ismail, A. F., Puteh, M. H., Rahman, M. A., and Jaafar, J. (2016). "Photocatalytic degradation of nonylphenol using co-extruded dual-layer hollow fibre membranes incorporated with a different ratio of TiO_2/PVDF." Reactive and Functional Polymers, 99, 80–87.

Eisazadeh, H. (2007). "Removal of Chromium from waste water using Polyaniline." Journal of Applied Polymer Science, 104(3), 1964–1967.

Ekramul Mahmud, H. N. M., Obidul Huq, A. K., and Yahya, R. B. (2016). "The removal of heavy metal ions from wastewater/aqueous solution using polypyrrole-based adsorbents: A review." RSC Advances, Royal Society of Chemistry.

Elakkiya, S., Arthanareeswaran, G., Ismail, A. F., Das, D. B., and Suganya, R. (2018). "Polyaniline coated sulfonated TiO_2 nanoparticles for effective application in proton conductive polymer membrane fuel cell." European Polymer Journal, (October), 0–1.

Elakkiya, S., Arthanareeswaran, G., Ismail, A. F., Das, D. B., and Suganya, R. (2019). "Polyaniline coated sulfonated TiO_2 nanoparticles for effective application in proton conductive polymer membrane fuel cell." European Polymer Journal, 112, 696–703.

Espíndola, J. C., Cristóvão, R. O., Mendes, A., Boaventura, R. A. R., and Vilar, V. J. P. (2019). "Photocatalytic membrane reactor performance towards oxytetracycline removal from synthetic and real matrices: Suspended vs immobilized TiO_2-P25." Chemical Engineering Journal, 378(April), 122114.

Etemadi, H., Yegani, R., and Seyfollahi, M. (2017). "The effect of amino functionalized and polyethylene glycol grafted nanodiamond on anti-biofouling properties of cellulose acetate membrane in membrane bioreactor systems." Separation and Purification Technology, 177, 350–362.

Fang, L.-F., Zhou, M.-Y., Cheng, L., Zhu, B.-K., Matsuyama, H., and Zhao, S. (2018). "Positively charged nanofiltration membrane based on cross-linked polyvinyl chloride copolymer." Journal of Membrane Science.

Feizpoor, S., Habibi-Yangjeh, A., and Yubuta, K. (2018). "Integration of carbon dots and polyaniline with TiO_2 nanoparticles: Substantially enhanced photocatalytic activity to removal various pollutants under visible light." Journal of Photochemistry and Photobiology A: Chemistry, 367, 94–104.

Fenga, Y., and , Shumin Yanga, Liu Xiae, Zhongwei Wangc, Ning Suoa, Hao Chena, Yingying Longa, Bo Zhoud, Y. Y. (2019). "In-situ ion exchange electrocatalysis biological coupling (I-IEEBC) for simultaneously enhanced degradation of organic pollutants and heavy metals in electroplating wastewater." Journal of Hazardous Materials, 364, 562–570.

Fryczkowska, B., Piprek, Z., Sieradzka, M., Fryczkowski, R., and Janicki, J. (2017). "Preparation and properties of composite PAN/PANI membranes." International Journal of Polymer Science, 2017.

Gao, P., Liu, Z., Tai, M., Sun, D. D., and Ng, W. (2013a). "Multifunctional graphene oxide-TiO_2 microsphere hierarchical membrane for clean water production." Applied Catalysis B: Environmental, 138–139, 17–25.

Gao, P., Tai, M. H., and Sun, D. D. (2013b). "Hierarchical TiO_2/V_2O_5 Multifunctional membrane for water purification." ChemPlusChem, 78(12), 1475–1482.

Gautam, R. K., Sharma, S. K., Mahiya, S., and Chattopadhyaya, M. C. (2014). "CHAPTER 1. Contamination of heavy metals in aquatic media: Transport, toxicity and technologies for remediation." Heavy Metals In Water, (October), 1–24.

Geng, Y., Li, J., Jing, X., and Wang, F. (1997). "Interaction of N-methylpyrrolidone with doped polyaniline." Synthetic Metals, 84(1–3), 97–98.

Golder, A. K., Chanda, A. K., Samanta, A. N., and Ray, S. (2011). "Removal of hexavalent chromium by electrochemical reduction-precipitation: Investigation of process performance and reaction stoichiometry." Separation and Purification Technology, 76(3), 345–350.

Golshenas, A., Sadeghian, Z., and Ashrafizadeh, S. N. (2020). "Performance evaluation of a ceramic-based photocatalytic membrane reactor for treatment of oily wastewater." Journal of Water Process Engineering, 36(September 2019).

Gu, L., Wang, J., Qi, R., Wang, X., Xu, P., and Han, X. (2012). "A novel incorporating style of polyaniline/TiO_2 composites as effective visible photocatalysts." Journal of Molecular Catalysis A: Chemical, 357, 19–25.

Harijan, D. K. L., and Chandra, V. (2016). "Polyaniline functionalized graphene sheets for treatment of toxic hexavalent chromium." Journal of Environmental Chemical Engineering, 4(3), 3006–3012.

Hassan, S. M., Ahmed, A. I., and Mannaa, M. A. (2019a). "Preparation and characterization of SnO_2 doped TiO_2 nanoparticles: Effect of phase changes on the photocatalytic and catalytic activity." Journal of Science: Advanced Materials and Devices, 4(3), 400–412.

He, Y., Ford, M. E., Zhu, M., Liu, Q., Wu, Z., and Wachs, I. E. (2016). "Selective catalytic reduction of NO by NH_3 with WO_3-TiO_2 catalysts: Influence of catalyst synthesis method." Applied Catalysis B: Environmental, 188, 123–133.

Horovitz, I., Avisar, D., Baker, M. A., Grilli, R., Lozzi, L., Camillo, D. Di, and Mamane, H. (2016). "Carbamazepine degradation using a N-doped TiO_2 coated photocatalytic membrane reactor: Influence of physical parameters." Journal of Hazardous Materials, 310, 98–107.

Hu, D., Li, R., Li, M., Pei, J., Guo, F., and Zhang, S. (2018a). "Photocatalytic efficiencies of WO_3/TiO_2 nanoparticles for exhaust decomposition under UV and visible light irradiation." Mater. Res. Express, 5, 95029.

Huang, M., Yu, J., Li, B., Deng, C., Wang, L., Wu, W., Dong, L., Zhang, F., and Fan, M. (2015a). "Intergrowth and coexistence effects of TiO_2-SnO_2 nanocomposite with excellent photocatalytic activity." Journal of Alloys and Compounds, 629, 55–61.

Huang, S., Ball, I. J., and Kaner, R. B. (1998). "Polyaniline Membranes for Pervaporation of Carboxylic Acids and Water." 9297(97), 5456–5464.

Huang, X., Mcverry, B. T., Marambio-jones, C., and Wong, M. C. Y. (2015b). "Novel chlorine resistant low-fouling ultra fi ltration membrane based on a hydrophilic polyaniline." 8725–8733.

Idris, A., Man, Z., Maulud, A. S., and Khan, M. S. (2017). "Effects of phase separation behavior on morphology and performance of polycarbonate membranes." Membranes, 7(2).

Ingole, N. W., and Dharpal, S. V. (2012). "State of art of biosorption technique for treatment of heavy metals bearing wastes." International Journal of Advanced Engineering Technology.

Jahan, K., Kumar, N., and Verma, V. (2018). "Environmental Science Water Research & Technology. Removal of hexavalent chromium from potable drinking using a polyaniline-coated bacterial cellulose mat ." Cite this: Environ. Sci.: Water Res. Technol, 4, 1589.

Jeffrey, S., Mintek, B., and Ochieng, A. (2014). Simultaneous photocatalytic reduction of Cr(VI) and oxidation of citric acid in aqueous solutions Simulation and modelling View project Photocatalysis View project.

Jentoft, F. C., Schmelz, H., and Knözinger, H. (1997). "Preparation of selective catalytic reduction catalysts via milling and thermal spreading." Applied Catalysis A: General, 161(1–2), 167–182.

Joshi, K. M., and Shrivastava, V. S. (2011). "Photocatalytic degradation of Chromium (VI) from wastewater using nanomaterials like TiO_2, ZnO, and CdS." Applied Nanoscience, 1(3), 147–155.

Jyothi, M. S., Nayak, V., Padaki, M., Geetha Balakrishna, R., and Soontarapa, K. (2016). "Aminated polysulfone/TiO$_2$ composite membranes for an effective removal of Cr(VI)." Chemical Engineering Journal, 283, 1494–1505.

Jyothi, M. S., Padaki, M., Geetha Balakrishna, R., and Krishna Pai, R. (2014). "Synthesis and design of PSf/TiO$_2$ composite membranes for reduction of chromium (VI): Stability and reuse of the product and the process." Journal of Materials Research, 29(14), 1537–1545.

Kabra, K., Chaudhary, R., and Sawhney, R. L. (2008). "Solar photocatalytic removal of metal ions from industrial wastewater." Environmental Progress, 27(4), 487–495.

Kang, S. Y., Lee, J. U., Moon, S. H., and Kim, K. W. (2004). "Competitive adsorption characteristics of Co^{2+}, Ni^{2+}, and Cr^{3+} by IRN-77 cation exchange resin in synthesized wastewater." Chemosphere, 56(2), 141–147.

Karthik, R., and Meenakshi, S. (2015). "Adsorption study on removal of Cr(VI) ions by polyaniline composite." Desalination and Water Treatment, 54(11), 3083–3093.

Kazemi, M., Peyravi, M., and Jahanshahi, M. (2020). "Multilayer UF membrane assisted by photocatalytic NZVI@TiO$_2$ nanoparticle for removal and reduction of hexavalent chromium." Journal of Water Process Engineering, 37(February), 101183.

Kertèsz, S., Cakl, J., and Jiránková, H. (2014). "Submerged hollow fiber microfiltration as a part of hybrid photocatalytic process for dye wastewater treatment." Desalination, 343, 106–112.

Khaki, M. R. D., Shafeeyan, M. S., Raman, A. A. A., and Daud, W. M. A. W. (2017). "Application of doped photocatalysts for organic pollutant degradation - A review." Journal of Environmental Management, Academic Press.

Khan, A., Khan, A. A. P., Rahman, M. M., Asiri, A. M., and Alamry, K. A. (2015). "Preparation of polyaniline grafted graphene oxide-WO$_3$ nanocomposite and its application as a chromium(III) chemi-sensor." RSC Advances, 5(127), 105169–105178.

Khulbe, K. C., and Matsuura, T. (2018). "Removal of heavy metals and pollutants by membrane adsorption techniques." Applied Water Science, 8(1).

Kononova, O. N., Bryuzgina, G. L., Apchitaeva, O. V., and Kononov, Y. S. (2019). "Ion exchange recovery of chromium (VI) and manganese (II) from aqueous solutions." Arabian Journal of Chemistry, 12(8), 2713–2720.

Kumar, A., Kumar, V., Sain, P. K., Kumar, M., and Awasthi, K. (2018). "Synthesis and characterization of polyaniline membranes with – secondary amine additive containing N,N″-dimethyl propylene urea for fuel cell application." International Journal of Hydrogen Energy, 21715–21723.

Kumar, R., and Yadav, B. C. (2016). "Fabrication of Polyaniline (PANI)-Tungsten oxide (WO$_3$) composite for humidity sensing application." Journal of Inorganic and Organometallic Polymers and Materials, 26(6), 1421–1427.

Kumari, P., Bahadur, N., and Dumée, L. F. (2020). "Photo-catalytic membrane reactors for the remediation of persistent organic pollutants – A review." Separation and Purification Technology, 230(May 2019), 115878.

Kurada, K. V., and De, S. (2018). "Polyaniline doped ultrafiltration membranes: Mechanism of membrane formation and pH response characteristics." Polymer, 153, 201–213.

Kuvarega, A. T., and Mamba, B. B. (2016). "Photocatalytic membranes for efficient water treatment." Semiconductor Photocatalysis - Materials, Mechanisms and Applications.

Lee, M. S., and Nicol, M. J. (2007). "Removal of iron from cobalt sulfate solutions by ion exchange with Diphonix resin and enhancement of iron elution with titanium(III)." Hydrometallurgy, 86(1–2), 6–12.

Li, J., Li, M., Wang, S., Yang, X., Liu, F., and Liu, X. (2020). "Key role of pore size in Cr(VI) removal by the composites of 3-dimentional mesoporous silica nanospheres wrapped with polyaniline." Science of the Total Environment, 729, 139009.

Li, J., Peng, T., Zhang, Y., Zhou, C., and Zhu, A. (2018a). "Polyaniline modified SnO$_2$ nanoparticles for efficient photocatalytic reduction of aqueous Cr(VI) under visible light." Separation and Purification Technology, 201(March), 120–129.

Li, Q., Liu, Q., Zhao, J., Hua, Y., Sun, J., Duan, J., and Jin, W. (2017). "High efficient water/ethanol separation by a mixed matrix membrane incorporating MOF filler with high water adsorption capacity." Journal of Membrane Science, 544(September), 68–78.

Li, Y., Yu, Y., Wu, L., and Zhi, J. (2013). "Processable polyaniline/titania nanocomposites with good photocatalytic and conductivity properties prepared via peroxo-titanium complex catalyzed emulsion polymerization approach." Applied Surface Science, 273, 135–143.

Liu, L., Xu, Y., Wang, K., Li, K., Xu, L., Wang, J., and Wang, J. (2019). "Fabrication of a novel conductive ultrafiltration membrane and its application for electrochemical removal of hexavalent chromium." Journal of Membrane Science, 584, 191–201.

Liu, M., Li, J., and Guo, Z. (2016). "Polyaniline coated membranes for effective separation of oil-in-water emulsions." Journal of Colloid and Interface Science, 467, 261–270.

Liu, S., Huang, J., Cao, L., Li, J., Ouyang, H., Tao, X., and Liu, C. (2014a). "One-pot synthesis of TiO_2-WO_3 composite nanocrystallites with improved photocatalytic properties under natural sunlight irradiation." Materials Science in Semiconductor Processing, 25, 106–111.

Liu, S., Yu, J., and Jaroniec, M. (2010). "Tunable photocatalytic selectivity of hollow TiO_2 microspheres composed of anatase polyhedra with exposed {001} facets." Journal of the American Chemical Society, 132(34), 11914–11916.

Liu, X., Zhou, W., Qian, X., Shen, J., and An, X. (2013a). "Polyaniline/cellulose fiber composite prepared using persulfate as oxidant for Cr(VI)-detoxification." Carbohydrate Polymers, 92(1), 659–661.

Liu, Z., Bai, H., and Sun, D. D. (2012). "Hierarchical CuO/ZnO membranes for environmental applications under the irradiation of visible light." International Journal of Photoenergy, 2012.

Long, M., Zhou, C., Xia, S., and Guadiea, A. (2017). "Concomitant Cr(VI) reduction and Cr(III) precipitation with nitrate in a methane/oxygen-based membrane biofilm reactor." Chemical Engineering Journal, 315, 58–66.

Luo, J., Chen, W., Song, H., and Liu, J. (2020). "Fabrication of hierarchical layer-by-layer membrane as the photocatalytic degradation of foulants and effective mitigation of membrane fouling for wastewater treatment." Science of the Total Environment, 699, 134398.

Ma, C. M., Shen, Y. S., and Lin, P. H. (2012). "Photoreduction of Cr(VI) ions in aqueous solutions by UV/ TiO$_2$ photocatalytic processes." International Journal of Photoenergy, 2012.

Macdiarmid, A. G., Chiang, J. C., Richter, A. F., and Epstein, A. J. (1987). Polyaniline: A new concept in conducting polymers. Synthetic Metals.

Magdalane, C. M., Kanimozhi, K., Arularasu, M. V., Ramalingam, G., and Kaviyarasu, K. (2019). "Self-cleaning mechanism of synthesized SnO$_2$/TiO$_2$ nanostructure for photocatalytic activity application for waste water treatment." Surfaces and Interfaces, 17.

Marinho, B. A., Cristóvão, R. O., Djellabi, R., Loureiro, J. M., Boaventura, R. A. R., and Vilar, V. J. P. (2017a). "Applied Catalysis B : Environmental Photocatalytic reduction of Cr(VI) over TiO$_2$ -coated cellulose acetate monolithic structures using solar light." "Applied Catalysis B, Environmental," 203, 18–30.

Masid, S., Tayade, R., and Rao, N. N. (2015). "Ph ton." 119, 190–203.

Mavinakere Ramesh, A., and Shivanna, S. (2018). " Visible Light Assisted Photocatalytic Degradation of Chromium (VI) by Using Nanoporous Fe$_2$O$_3$." Journal of Materials, 2018, 1–13.

Meichtry, J. M., Brusa, M., Mailhot, G., Grela, M. A., and Litter, M. I. (2007). "Heterogeneous photocatalysis of Cr(VI) in the presence of citric acid over TiO$_2$ particles: Relevance of Cr(V)-citrate complexes." Applied Catalysis B: Environmental, 71(1–2), 101–107.

Mendonça, V. R. de, Avansi, W., Arenal, R., and Ribeiro, C. (2017). "A building blocks strategy for preparing photocatalytically active anatase TiO$_2$/rutile SnO$_2$ heterostructures by hydrothermal annealing." Journal of Colloid and Interface Science, 505, 454–459.

Mirmohseni, A., and Saeedi, A. (1998). Application of Conducting Polyaniline Membranes (II) Separation of H$_2$SO$_4$/H$_3$PO$_4$ and HNOS/H$_2$SO$_4$ Using Dialysis, Electrodialysis and Electrodynamic Methods. Iranian Polymer Journal.

Mnif, A., Bejaoui, I., Mouelhi, M., and Hamrouni, B. (2017). "Hexavalent Chromium removal from model water and car shock absorber factory effluent by nanofiltration and reverse osmosis membrane." International Journal of Analytical Chemistry, 2017.

Mohammad Jafri, N. N., Jaafar, J., Dzarfan Othman, M. H., Rahman, M. A., Aziz, F., Yusof, N., Wan Salleh, W. N., and Fauzi Ismail, A. (2020). "Titanium dioxide hollow nanofibers for enhanced photocatalytic activities." Materials Today: Proceedings, 46, 2004–2011.

Mohammed, K., and Sahu, O. (2019). "Recovery of chromium from tannery industry waste water by membrane separation technology: Health and engineering aspects." Scientific African, 4, e00096.

Molinari, R., Mungari, M., Drioli, E., Paola, A. Di, Loddo, V., Palmisano, L., and Schiavello, M. (2000). Study on a photocatalytic membrane reactor for water purification. Catalysis Today.

Molinari, R., Pirillo, F., Falco, M., Loddo, V., and Palmisano, L. (2004). "Photocatalytic degradation of dyes by using a membrane reactor." Chemical Engineering and Processing: Process Intensification, 43(9), 1103–1114.

Molinari, R., Scicchitano, G., Pirillo, F., Loddo, V., and Palmisano, L. (2005). "At present he is Process Engineer at the factory Cellulosa." Int. J. Environment and Pollution, 23(2), 140–152.

Monjezi, S., Soltanieh, M., Sanford, A. C., and Park, J. (2018). "Polyaniline membranes for nanofiltration of solvent from dewaxed lube oil." Separation Science and Technology, 54(5), 795–802.

Monjezi, S., Soltanieh, M., Sanford, A. C., and Park, J. (2019). "Polyaniline membranes for nanofiltration of solvent from dewaxed lube oil." Separation Science and Technology (Philadelphia), 54(5), 795–802.

Moradi, G., Zinadini, S., and Rajabi, L. (2020). "Development of the tetrathioterephthalate filler incorporated PES nanofiltration membrane with efficient heavy metal ions rejection and superior antifouling properties." Journal of Environmental Chemical Engineering, 8(6), 104431.

Mourabet, M., Rhilassi, A. El, Boujaady, H. El, Bennani-Ziatni, M., and Taitai, A. (2017a). "Use of response surface methodology for optimization of fluoride adsorption in an aqueous solution by Brushite." Arabian Journal of Chemistry, 10, S3292–S3302.

Mozia, S., Argurio, P., and Molinari, R. (2018). PMRs utilizing pressure-driven membrane techniques. Current trends and future developments on (Bio-) membranes: Photocatalytic membranes and photocatalytic membrane reactors, Elsevier Inc.

Mozia, S., Toyoda, M., Tsumura, T., Inagaki, M., and Morawski, A. W. (2007). "Comparison of effectiveness of methylene blue decomposition using pristine and carbon-coated TiO_2 in a photocatalytic membrane reactor." Desalination, 212(1–3), 141–151.

Mugunthan, E., Saidutta, M. B., and Jagadeeshbabu, P. E. (2018a). "Visible light assisted photocatalytic degradation of diclofenac using TiO_2-WO_3 mixed oxide catalysts." Environmental Nanotechnology, Monitoring and Management, 10, 322–330.

Mugunthan, E., Saidutta, M. B., and Jagadeeshbabu, P. E. (2019). "Photocatalytic degradation of diclofenac using TiO_2–SnO_2 mixed oxide catalysts." Environmental Technology (United Kingdom), 40(7), 929–941.

Mukherjee, R., Sharma, R., Saini, P., and De, S. (2015). "Nanostructured polyaniline incorporated ultrafiltration membrane for desalination of brackish water." Environmental Science: Water Research and Technology, 1(6), 893–904.

Muthumareeswaran, M. R., Alhoshan, M., and Agarwal, G. P. (2017). "Ultrafiltration membrane for effective removal of chromium ions from potable water." Nature Publishing Group, (September 2016), 1–12.

Nadig, A. R., Naik, N. S., Padaki, M., and Pai, R. K. (2021). "Journal of Water Process Engineering Impact of graphitic carbon nitride nanosheets in mixed- matrix membranes for removal of heavy metals from water." 41(December 2020), 1–11.

Naimi-Joubani, M., Shirzad-Siboni, M., Yang, J. K., Gholami, M., and Farzadkia, M. (2015). "Photocatalytic reduction of hexavalent chromium with illuminated ZnO/TiO_2 composite." Journal of Industrial and Engineering Chemistry, 22, 317–323.

Nair, A. K., and Jagadeesh, J. B. (2017). "TiO_2 nanosheet-graphene oxide based photocatalytic hierarchical membrane for water purification." Surface and Coatings Technology, 320, 259–262.

Nair, A. K., and JagadeeshBabu, P. E. (2017). "Ag-TiO_2 nanosheet embedded photocatalytic membrane for solar water treatment." Journal of Environmental Chemical Engineering, 5(4), 4128–4133.

Nair, A. K., Shalin, P. M., and JagadeeshBabu, P. E. (2016). "Performance enhancement of polysulfone ultrafiltration membrane using TiO_2 nanofibers." Desalination and Water Treatment, 57(23), 10506–10514.

Ngo, A. B., Nguyen, H. L., and Hollmann, D. (2018). "Criticial assessment of the photocatalytic reduction of Cr(VI) over Au/TiO_2." Catalysts, 8(12).

Nguyen, V. H., Tran, Q. B., Nguyen, X. C., Hai, L. T., Ho, T. T. T., Shokouhimehr, M., Vo, D. V. N., Lam, S. S., Nguyen, H. P., Hoang, C. T., Ly, Q. V., Peng, W., Kim, S. Y., Tung, T. Van, and Le, Q. Van. (2020). "Submerged photocatalytic membrane reactor with suspended and immobilized N-doped TiO_2 under visible irradiation for diclofenac removal from wastewater." Process Safety and Environmental Protection, 142, 229–237.

Nie, L., Guo, X., Gao, C., Wu, X., Chen, J., and Peng, L. (2022). "Fabrication and optical hydrogen gas sensing property of hierarchical WO_3 Porous/Nanowires film." Materials Letters, 314(February), 131805.

Norris, I. D., Fadeev, A. G., Pellegrino, J., and Mattes, B. R. (2005). "Development of integrally skinned asymmetric polyaniline hollow fibers for membrane applications." Synthetic Metals, 153(1–3), 57–60.

Novaković, K., Gilja, V., Ţic, M., and Hrnjak-Murgić, Z. (2016). In situ synthesis of the novel $PANI/TiO_2$ photocatalysts for azo dye degradation in wastewater.

Nur-E-Alam, M., Mia, M. A. S., Ahmad, F., and Rahman, M. M. (2020). "An overview of chromium removal techniques from tannery effluent." Applied Water Science, 10(9), 1–22.

Ohta, T., Masegi, H., and Noda, K. (2018). "Photocatalytic decomposition of gaseous methanol over anodized iron oxide nanotube arrays in high vacuum." Materials Research Bulletin, 99, 367–376.

Olad, A., and Nosrati, R. (2012). "Preparation, characterization, and photocatalytic activity of polyaniline/ZnO nanocomposite." Research on Chemical Intermediates, 38(2), 323–336.

Oliveira, H. (2012). "Chromium as an Environmental Pollutant: Insights on Induced Plant Toxicity." Journal of Botany, 2012, 1–8.

Osipenko, V. D., and Pogorelyi, P. I. (1977). "Electrocoagulation neutralization of chromium containing effluent." Metallurgist, 21(9), 628–630.

Pakdel Mojdehi, A., Pourafshari Chenar, M., Namvar-Mahboub, M., and Eftekhari, M. (2019). "Development of PES/polyaniline-modified TiO_2 adsorptive membrane for copper removal." Colloids and Surfaces A: Physicochemical and Engineering Aspects, 583(July).

Pakizeh, M., Moghadam, A. N., Omidkhah, M. R., and Namvar-Mahboub, M. (2013). "Preparation and characterization of dimethyldichlorosilane modified SiO_2/PSf nanocomposite membrane." Korean Journal of Chemical Engineering, 30(3), 751–760.

Patil, S. M., Dhodamani, A. G., Vanalakar, S. A., Deshmukh, S. P., and Delekar, S. D. (2018). "Multi-applicative tetragonal TiO_2/SnO_2 nanocomposites for photocatalysis and gas sensing." Journal of Physics and Chemistry of Solids, 115, 127–136.

Paul, M. L., Samuel, J., Roy, R., Chandrasekaran, N., and Mukherjee, A. (2015). Studies on Cr(VI) removal from aqueous solutions by nanotitania under visible light and dark conditions. Bull. Mater. Sci.

Peng, H., Guo, J., Qiu, H., Wang, C., Zhang, C., Hao, Z., Rao, Y., and Gong, Y. (2021). "Efficient removal of cr (Vi) with biochar and optimized parameters by response surface methodology." Processes, 9(5).

Peng, H., Leng, Y., Cheng, Q., Shang, Q., Shu, J., and Guo, J. (2019). "Efficient removal of hexavalent chromium from wastewater with electro-reduction." Processes, 7(1).

Pereira, V. R., Isloor, A. M., Ahmed, A. Al, and Ismail, A. F. (2015). "Preparation, characterization and the effect of PANI coated TiO_2 nanocomposites on the performance of polysulfone ultrafiltration membranes." New Journal of Chemistry, 39(1), 703–712.

Pereira, V. R., Isloor, A. M., Bhat, U. K., and Ismail, A. F. (2014). "Preparation and antifouling properties of PVDF ultrafiltration membranes with polyaniline (PANI) nanofibers and hydrolysed PSMA (H-PSMA) as additives." Desalination, 351(November), 220–227.

Petsi, P. N., Sarasidis, V. C., Plakas, K. V., and Karabelas, A. J. (2021). "Reduction of nitrates in a photocatalytic membrane reactor in the presence of organic acids." Journal of Environmental Management, 298(3), 113526.

Pinos, V., Dafinov, A., Medina, F., and Sueiras, J. (2016). "Chromium(VI) reduction in aqueous medium by means of catalytic membrane reactors." Journal of Environmental Chemical Engineering, 4(2), 1880–1889.

Piriyanon, J., Takhai, P., Patta, S., and Chankhanittha, T. (2021). "Performance of sunlight responsive WO$_3$/AgBr heterojunction photocatalyst toward degradation of Rhodamine B dye and ofloxacin antibiotic." Optical Materials, 121(September), 111573.

Prajapati, A. K., and Mondal, M. K. (2021). "Green synthesis of Fe 3 O 4 -onion peel biochar nanocomposites for adsorption of Cr(VI), methylene blue and congo red dye from aqueous solutions." Journal of Molecular Liquids, (xxxx), 118161.

Qiu, B., Xu, C., Sun, D., Wang, Q., Gu, H., Zhang, X., Weeks, B. L., Hopper, J., Ho, T. C., Guo, Z., and Wei, S. (2015). "Applied Surface Science Polyaniline coating with various substrates for hexavalent chromium removal." Applied Surface Science, 334, 7–14.

Rathna, T., PonnanEttiyappan, J., and D., R. (2021). "Fabrication of visible-light assisted TiO$_2$-WO$_3$-PANI membrane for effective reduction of chromium (VI) in photocatalytic membrane reactor." Environmental Technology & Innovation, 24, 102023.

Rezazadeh, T., Dalali, N., and Sehati, N. (2018). "Investigation of adsorption performance of graphene oxide/polyaniline reinforced hollow fiber membrane for preconcentration of Ivermectin in some environmental samples." Spectrochimica Acta - Part A: Molecular and Biomolecular Spectroscopy, 204, 409–415.

Rohani, R., Yusoff, I. I., Efdi, F. A. M., Mohd Junaidi, M. U., and Qaiser, A. A. (2017a). "Polyaniline Composite Membranes Synthesis in Presence of Various Acid Dopants for Pressure Filtration." Jurnal Kejuruteraan, 29(2), 121–130.

Rosaih Rohani, Izzati Izni Yosoff, F. A. (2018). "Polyaniline Composite Membranes Synthesis in Presence of Various Acid Dopants for Pressure Filtration." 29(2), 121–130.

Sahu, S., Sahu, U. K., and Patel, R. K. (2019). "Modified Thorium Oxide Polyaniline Core-Shell Nanocomposite and Its Application for the Efficient Removal of Cr(VI)." Journal of Chemical and Engineering Data, 64(3), 1294–1304.

Sairam, M., Nataraj, S. K., Aminabhavi, T. M., Roy, S., and Madhusoodana, C. D. (2006). "Polyaniline membranes for separation and purification of gases, liquids, and electrolyte solutions." Separation and Purification Reviews, 35(4), 249–283.

Sairam, M., Xing, X., Li, K., Bismarck, A., Hans, J., Steinke, G., and Guy, A. (2009). "Nanoporous asymmetric polyaniline films for filtration of organic solvents." 330, 166–174.

Sajan, C. P., Wageh, S., Al-Ghamdi, A. A., Yu, J., and Cao, S. (2016). "TiO$_2$ nanosheets with exposed {001} facets for photocatalytic applications." Nano Research, 9(1), 3–27.

Samani, M. R., Ebrahimbabaie, P., and Molamahmood, H. V. (2016). "Hexavalent chromium removal by using synthesis of polyaniline and polyvinyl alcohol." (September 2017).

Sanchez-Hachair, A., and Hofmann, A. (2018). "Hexavalent chromium quantification in solution: Comparing direct UV–visible spectrometry with 1,5-diphenylcarbazide colorimetry." Comptes Rendus Chimie, 21(9), 890–896.

Sane, P., Chaudhari, S., Nemade, P., and Sontakke, S. (2018). "Photocatalytic reduction of chromium (VI) using combustion synthesized TiO$_2$." Journal of Environmental Chemical Engineering, 6(1), 68–73.

Sarmah, S., and Kumar, A. (2011). "Photocatalytic activity of polyaniline-TiO2 nanocomposites." Indian Journal of Physics, 85(5), 713–726.

Shankar, B. (2009a). "Chromium Pollution in the Groundwaters of an Industrial Area in Bangalore, India." Environmental Engineering Science, 26(2), 305–310.

Shaposhnik, D., Pavelko, R., Llobet, E., Gispert-Guirado, F., and Vilanova, X. (2012). "Hydrogen sensors on the basis of SnO$_2$-TiO$_2$ systems." Sensors and Actuators, B: Chemical, 174, 527–534.

Shi, Y., Huang, J., Zeng, G., Cheng, W., and Hu, J. (2019a). "Photocatalytic membrane in water purification: is it stepping closer to be driven by visible light?" Journal of Membrane Science, Elsevier B.V.

Shubha, L. N., Kalpana, M., and Madhusudana Rao, P. (2016). "Synthesis, characterization by AC conduction and antibacterial properties of polyaniline fibers." Der Pharmacia Lettre, 8(1), 214–219.

Singh, C., and Chaudhary, R. (2013). "Visible light induced photocatalytic reduction of metals (Cr, Cu, Ni, and Zn) and its synergism with different pH, TiO$_2$, and H$_2$O$_2$ doses in simulated wastewater." Journal of Renewable and Sustainable Energy, 5(5), 1–14.

Sirshendu De. (2015). "Module : Membrane based separation processes." Membrane based separation processes, 1–120.

Stejskal, J., Kratochvíl, P., and Radhakrishnan, N. (1993). "Polyaniline dispersions 2. UV-Vis absorption spectra." Synthetic Metals, 61(3), 225–231.

Strathmann, H., and Kock, K. (1977). "The formation mechanism of phase inversion membranes." Desalination, 21(3), 241–255.

Sunil, K., Karunakaran, G., Yadav, S., Padaki, M., Zadorozhnyy, V., and Pai, R. K. (2018). "Al-Ti$_2$O$_6$ a mixed metal oxide based composite membrane: A unique membrane for removal of heavy metals." Chemical Engineering Journal, 348, 678–684.

Syafei, A. D., Lin, C. F., and Wu, C. H. (2008). "Removal of natural organic matter by ultrafiltration with TiO$_2$-coated membrane under UV irradiation." Journal of Colloid and Interface Science, 323(1), 112–119.

Tan, S., Laforgue, A., and Bélanger, D. (2003). "Characterization of a cation-exchange/polyaniline composite membrane." Langmuir, 19(3), 744–751.

Tao, S., Xu, Y. D., Gu, J. Q., Abadikhah, H., Wang, J. W., and Xu, X. (2018). "Preparation of high-efficiency ceramic planar membrane and its application for water desalination." Journal of Advanced Ceramics, 7(2), 117–123.

Teli, S. B., Molina, S., Sotto, A., Garc, E., and Abajo, J. De. (2013). "Shivanand B. Teli, Fouling Resistant Polysulfone − PANI/TiO$_2$ Ultrafiltration.pdf."

Testa, J. J., and Qu, D. De. (2004). "Heterogeneous Photocatalytic Reduction of Chromium (VI) over TiO$_2$ Particles in the Presence of Oxalate : Involvement of Cr(V) Species." 38(5), 1589–1594.

Valari, M., Antoniadis, A., Mantzavinos, D., and Poulios, I. (2015). "Photocatalytic reduction of Cr(VI) over titania suspensions." Catalysis Today, 252, 190–194.

Vellaichamy, B., Periakaruppan, P., and Nagulan, B. (2017a). "Reduction of Cr6+ from Wastewater Using a Novel in Situ-Synthesized PANI/MnO$_2$/TiO$_2$ Nanocomposite: Renewable, Selective, Stable, and Synergistic Catalysis." ACS Sustainable Chemistry and Engineering, 5(10), 9313–9324.

Wang, F., Min, S., Han, Y., and Feng, L. (2010). "Visible-light-induced photocatalytic degradation of methylene blue with polyaniline-sensitized TiO$_2$ composite photocatalysts." Superlattices and Microstructures, 48(2), 170–180.

Wang, K., Xu, L., Li, K., Liu, L., Zhang, Y., and Wang, J. (2019). "Development of polyaniline conductive membrane for electrically enhanced membrane fouling mitigation." Journal of Membrane Science, 570–571(July 2018), 371–379.

Wang, N., Feng, J., Chen, J., Wang, J., and Yan, W. (2017). "Adsorption mechanism of phosphate by polyaniline/TiO_2 composite from wastewater." Chemical Engineering Journal, 316, 33–40.

Wang, W. Y., Irawan, A., and Ku, Y. (2008). "Photocatalytic degradation of Acid Red 4 using a titanium dioxide membrane supported on a porous ceramic tube." Water Research, 42(19), 4725–4732.

Wang, X., Wang, J., Teng, W., Du, Y., Wu, J., Guo, F., and Chen, B. (2021). "Fabrication of highly efficient magnesium silicate and its adsorption behavior towards Cr(VI)." Microporous and Mesoporous Materials, 323(January), 111196.

Wang, Z., Wu, A., Colombi Ciacchi, L., and Wei, G. (2018). "Recent Advances in Nanoporous Membranes for Water Purification." Nanomaterials, 8(2), 65.

Wen, L., and Kocherginsky, N. M. (1999). "Doping-dependent ion selectivity of polyaniline membranes." Synthetic Metals, 106(1), 19–27.

Wen, Y., Yuan, J., Ma, X., Wang, S., and Liu, Y. (2019). "Polymeric nanocomposite membranes for water treatment: a review." Environmental Chemistry Letters, 17(4), 1539–1551.

Wu, Q., Zhao, J., Qin, G., Wang, C., Tong, X., and Xue, S. (2013). "Applied Catalysis B : Environmental Photocatalytic reduction of Cr(VI) with TiO_2 film under visible light ૬." "Applied Catalysis B, Environmental," 142–143, 142–148.

Xu, L., Shahid, S., Holda, A. K., Emanuelsson, E. A. C., and Patterson, D. A. (2018). "Stimuli responsive conductive polyaniline membrane: In-filtration electrical tuneability of flux and MWCO." Journal of Membrane Science, 552, 153–166.

Yang, D., and Mattes, B. R. (2002). "Polyaniline emeraldine base in N-methyl-2-pyrrolidinone containing secondary amine additives: A rheological investigation of solutions." Journal of Polymer Science, Part B: Polymer Physics, 40(23), 2702–2713.

Yang, H. G., Sun, C. H., Qiao, S. Z., Zou, J., Liu, G., Smith, S. C., Cheng, H. M., and Lu, G. Q. (2008). "Anatase TiO_2 single crystals with a large percentage of reactive facets." Nature, 453(7195), 638–641.

Yin, R., Ling, L., Xiang, Y., Yang, Y., Bokare, A. D., and Shang, C. (2018). "Enhanced photocatalytic reduction of chromium (VI) by Cu-doped TiO_2 under UV-A irradiation." Separation and Purification Technology, 190, 53–59.

Yong Ng, L. Y., Mohammad, A. W., Leo, C. P., and Hilal, N. (2013). "Polymeric membranes incorporated with metal/metal oxide nanoparticles: A comprehensive review." Desalination, 308, 15–33.

Yue, L., Xie, Y., Zheng, Y., He, W., Guo, S., Sun, Y., Zhang, T., and Liu, S. (2017). "Sulfonated bacterial cellulose/polyaniline composite membrane for use as gel polymer electrolyte." Composites Science and Technology, 145, 122–131.

Yusoff, I. I., Rohani, R., Khairul Zaman, N., Junaidi, M. U. M., Mohammad, A. W., and Zainal, Z. (2019). "Durable pressure filtration membranes based on polyaniline–polyimide P84 blends." Polymer Engineering and Science, 59, E82–E92.

Zare, E. N., Motahari, A., and Sillanpää, M. (2018). "Nanoadsorbents based on conducting polymer nanocomposites with main focus on polyaniline and its derivatives for removal of heavy metal ions/dyes: A review." Environmental Research, Academic Press Inc.

Zhang, R., Ma, H., and Wang, B. (2010). "Removal of chromium(VI) from aqueous solutions using polyaniline doped with sulfuric acid." Industrial and Engineering Chemistry Research, 49(20), 9998–10004.

Zhao, J., Xing, W., Li, Y., and Lu, K. (2015). "Solvothermal synthesis and visible light absorption of anatase TiO_2." Materials Letters, 145, 332–335.

Zhao, T., Qian, R., Zhou, G., Wang, Y., Lee, W. I., and Pan, J. H. (2021). "Mesoporous WO_3/TiO_2 spheres with tailored surface properties for concurrent solar photocatalysis and membrane filtration." Chemosphere, 263, 128344.

Zheng, W., Angelopoulos, M., Epstein, A. J., and Macdiarmid, A. G. (1997). "Concentration dependence of aggregation of Polyaniline in NMP solution and properties of resulting cast films." 9297(97), 7634–7637.

Zheng, X., Wang, Q., Chen, L., Wang, J., and Cheng, R. (2015). "Photocatalytic membrane reactor (PMR) for virus removal in water: Performance and mechanisms." Chemical Engineering Journal, 277, 124–129.

In this appendix, the calibration curve for Chromium (VI) at a wavelength 350 nm, the calibration curve for DPC-Chromium (VI) complex obtained during Diphenyl carbazide colorimetry method and the calibration curve for BSA is given.

Calibration curve for DPC-Cr(VI) colorimetry

$y=0.010x$
$R^2= 0.997$

Calibration curve for BSA

$y=0.556 x$
$R^2= 0.990$
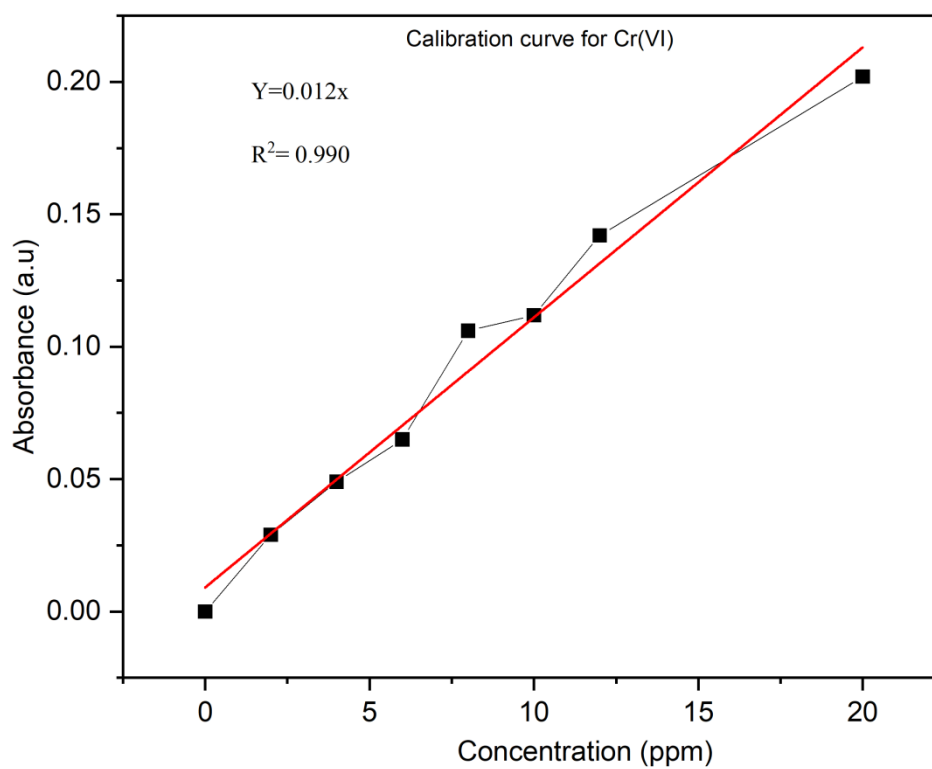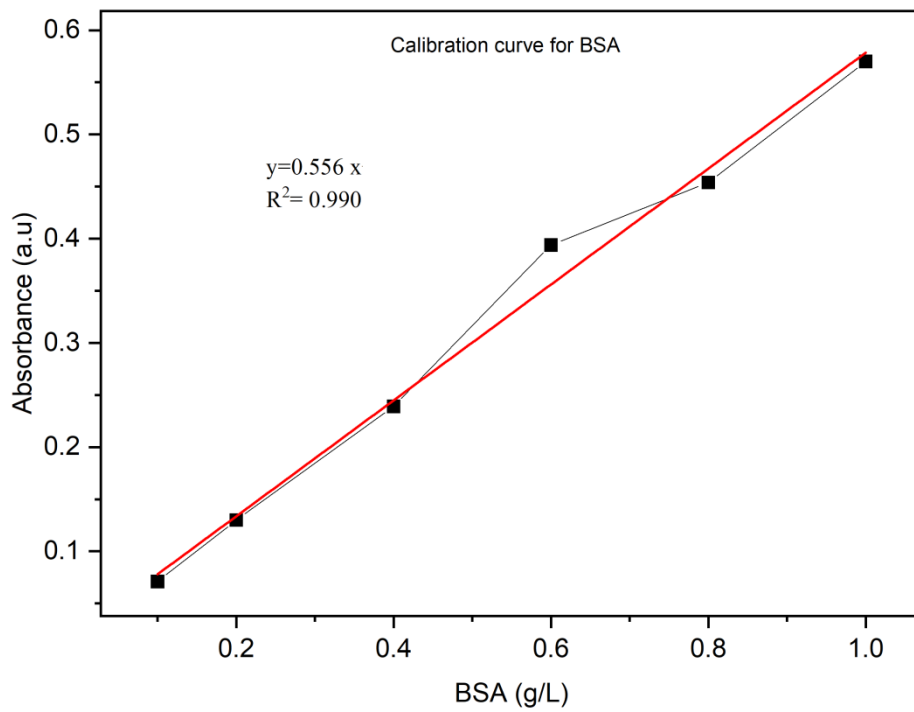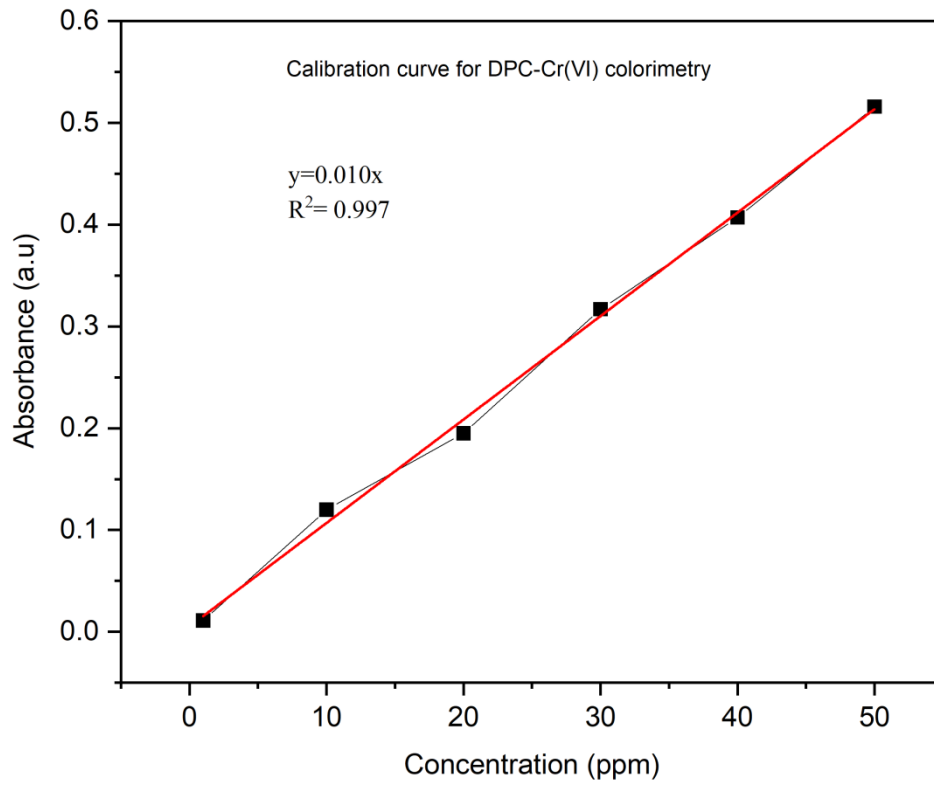
LIST OF PUBLICATIONS FROM THE RESEARCH WORK

International Journal Publications

1. Rathna, T., PonnanEttiyappan, J., and D., Ruben Sudhakar. (2021). "Fabrication of visible-light assisted TiO_2-WO_3-PANI membrane for effective reduction of chromium (VI) in photocatalytic membrane reactor." Published in Environmental Technology and Innovation, Elsevier 24, 102023. https://doi.org/10.1016/j.eti.2021.102023

2. Rathna, T., PonnanEttiyappan, J., and D., Ruben Sudhakar. (2022). "Synthesis, Characterization, and Performance Evaluation of TiO_2-SnO_2 photocatalyst for Removal of Toxic Hexavalent Chromium". Published in the journal of Water, air and soil pollution, Springer. https://doi.org/10.1007/s11270-022-05718-2

3. Rathna, T., PonnanEttiyappan, J., and D., Ruben Sudhakar. "TiO_2-WO_3 Nanocube-Polyaniline Hierarchical Photocatalytic Membrane for Efficient Removal of Chromium in a Photocatalytic Membrane Reactor". Water and Environment Journal, Wiley Online Library (Accepted).

Conference Papers

1. Rathna, T., PonnanEttiyappan, J., Rajmohan., B. "Visible light photocatalytic degradation of hexavalent Chromium using TiO_2-WO_3". Abstract published in 'The 2nd green technologies for sustainable water 2019 conference (GSTW 2019)' held on 1st-5th , December 2019 in Vietnam.

2. Rathna, T., PonnanEttiyappan, J., "Visible light assisted photocatalytic reduction of Chromium (VI) using PANI/TiO_2 nanocomposite from aqueous solutions". Paper presented in 'International conference on advances in manufacturing technologies and application of artificial intelligence' held on 06-07th, August 2021 (On-line mode) in Graphic Era University, Dehradun, Uttarakhand, India. https://doi.org/10.1063/5.0113905.

BIO-DATA

Thara Rathna I.V

Email ID: thararathna91@gmail.com

Contact no: +918281475571

Personal Details:

Fathers Name:	Thamban. A
Date of birth:	02nd January, 1991
Gender:	Female
Nationality:	Indian
Permanent address:	Aikkottuvalapil,
	Puthariyadukkam P.O,
	Nileshwar,
	Kasargod,
	Kerala, India 671314

Educational Qualification:

- **Ph.D in Chemical Engineering** (CGPA 6.7), 2017-2022

  Department of Chemical Engineering

  National Institute of Technology Karnataka

  Surathkal, Mangalore, 575025

- **M.Tech in Polymer Technology** (CGPA 8.1), 2015-2017

  Department of Polymer Science and Rubber Technology

  Cochin University of Science and Technology

  Kalamassery, Cochin, 682022

- **AMIE in Chemical Engineering** (GPA 8.78), 2008-2012

  Visveswaraya Institute of Engineering Technology,

  Mattakara, Kottayam, 686564

Publications

International Journal Publications

1. Rathna, T., PonnanEttiyappan, J., and D., Ruben Sudhakar. (2021). "Fabrication of visible-light assisted TiO_2-WO_3-PANI membrane for effective reduction of chromium (VI)

in photocatalytic membrane reactor." Published in Environmental Technology and Innovation, Elsevier 24, 102023. https://doi.org/10.1016/j.eti.2021.102023

2. Rathna, T., PonnanEttiyappan, J., and D., Ruben Sudhakar. (2022). "Synthesis, Characterization, and Performance Evaluation of TiO_2-SnO_2 photocatalyst for Removal of Toxic Hexavalent Chromium". Published in the journal of Water, air and soil pollution, Springer. https://doi.org/10.1007/s11270-022-05718-2

3. Rathna, T., PonnanEttiyappan, J., and D., Ruben Sudhakar. "TiO_2-WO_3 Nanocube-Polyaniline Hierarchical Photocatalytic Membrane for Efficient Removal of Chromium in a Photocatalytic Membrane Reactor". Water and Environment Journal, Wiley Online Library (Accepted).

Conference Papers

1. Rathna, T., PonnanEttiyappan, J., Rajmohan., B. "Visible light photocatalytic degradation of hexavalent Chromium using TiO_2-WO_3". Abstract published in 'The 2nd green technologies for sustainable water 2019 conference (GSTW 2019)' held on 1st-5th , December 2019 in Vietnam.

2. Rathna, T., PonnanEttiyappan, J., "Visible light assisted photocatalytic reduction of Chromium (VI) using PANI/TiO_2 nanocomposite from aqueous solutions". Paper presented in 'International conference on advances in manufacturing technologies and application of artificial intelligence' held on 06-07th, August 2021 (On-line mode) in Graphic Era University, Dehradun, Uttarakhand, India. https://doi.org/10.1063/5.0113905.

Other work

1. Polyaniline Based Electrochemical Sensor for Monitoring Bacterial Growth

Thara Rathna, Pallavi Koyande, Bhawana Thakur and S. N. Sawant*

Published in the conference proceeding at DAE – BRNS 6th Interdisciplinary Symposium on Material Chemistry (ISMC -2016) held during Dec 6-10th 2016 at BARC, Mumbai.

Declaration:

I hereby declare that the above particulars are true to the best of my knowledge and belief.

Place: Surathkal

Date: 20/06/2023

Thara Rathna I.V